

FUNDAMENTALS AND APPLICATIONS OF ION MOBILITY USING 3D PRINTED DEVICES

by

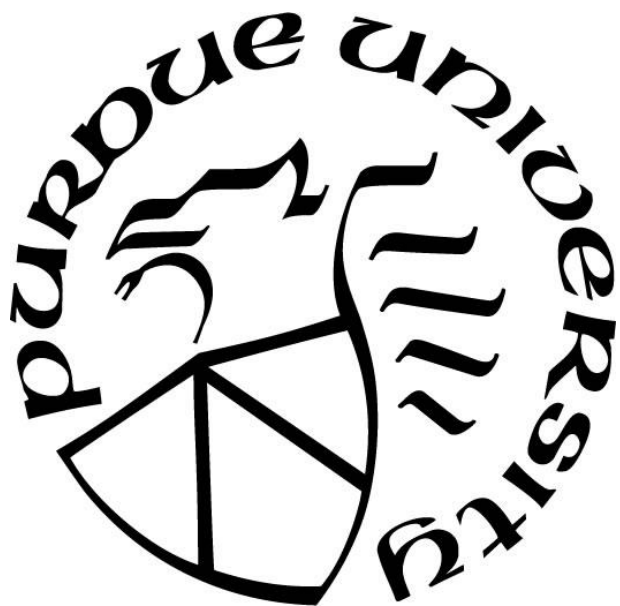
Robert L. Schrader

A Dissertation

Submitted to the Faculty of Purdue University

In Partial Fulfillment of the Requirements for the degree of

Doctor of Philosophy



Department of Chemistry

West Lafayette, Indiana

August 2021

THE PURDUE UNIVERSITY GRADUATE SCHOOL
STATEMENT OF COMMITTEE APPROVAL

Dr. R. Graham Cooks, Chair

Department of Chemistry

Dr. Scott McLuckey

Department of Chemistry

Dr. Christina Li

Department of Chemistry

Dr. Julia Laskin

Department of Chemistry

Approved by:

Dr. Christine Hrycyna

Dedicated to Mom, Dad, and Andy

ACKNOWLEDGMENTS

When I was in second grade, my teacher wanted our parents to give us a practice spelling test. That was *certainly* not my mother's style... Instead, she bought me a tape recorder so that I could record the words and play them back to do the spelling test myself. My parents always made sure that I was set up for success. My brother, Andy, always made sure that I knew that I was the little brother. My family has always supported me in becoming the person that I am today.

My research advisor, Professor R. Graham Cooks, deserves a great deal of the credit for this dissertation. His nearly endless enthusiasm for science and mass spectrometry is contagious. He has been a model for how a great scientist should be. Brandy McMasters was an integral part of learning how to get things done in the lab in my early years.

The former members of Aston Labs Saturdays working in the lab with Dr. Ryan Bain, Dr. Patrick Fedick, and Dr. Stephen Ayrton at the beginning of my graduate career were important in learning how to be a graduate student (even though I don't remember a whole lot of work getting done). Dr. Dalton Snyder was always willing to teach me, even when he thought it was a bad idea, and answer my questions. The results of helpful discussions with Dr. Brett Marsh can be seen throughout this dissertation. The rest of Aston Labs has provided me with Dr. Christina Ferreira, Dr. Valentina Pirro, Dr. Caitlin Falcone, Dr. Cedric D'Hue, Dr. Christopher Pulliam, Dr. Adam Hollerbach, Dr. Karen Yannell, Dr. Clint Alfaro, Dr. Kiran Iyer, Dr. David Logsdon, Dr. Zhouer Xie, Dr. Fan Pu, Dr. Zenwei Wei, Dr. Yangjie Li, Dr. Tsdale Mehari, Xingshuo Chen, Hannah Brown, Lucas Szalwinski, Sangeeta Pandey, Lillian Chen, Saquib Rahman, Lingqi Qiu, Edwin Gonzalez, Nicolás Morato, Yanyang Hu, Kai-Hung Huang, Dylan Holden, and Phoebe Le, and Dr. Jyotimoy Ghosh. In addition to their professional contributions, Sangeeta Pandey, Lucas Szalwinski, and Erin Lang are thanked for their personal contributions to "casserole night."

I was lucky enough to work on two projects with industrial collaborators, Dr. Andreas Kaerner of Eli Lilly, and Dr. Mitch Wells of Teledyne FLIR who both provided valuable comments throughout all of this work. I also had the opportunity to collaborate with Greg Eakins at the Jonathan Amy Facility for Chemical Instrumentation who contributed greatly to the IMS work.

I would like to thank my committee members, Dr. Scott McLuckey, Dr. Christina Li, and Dr. Julia Laskin, for their help and advice during this process.

My high school chemistry teacher, Mr. Countryman, told me, “You’re not very handy in the lab– you might want to think about theoretical chemistry.” I’d like to think that now I’m a bit handier in the lab.

TABLE OF CONTENTS

LIST OF TABLES	9
LIST OF FIGURES	10
LIST OF SCHEMES.....	16
ABSTRACT.....	17
CHAPTER 1. INTRODUCTION	19
1.1 Overview	19
1.2 Additive Manufacturing	19
1.3 Additive Manufacturing in Mass Spectrometry	21
1.4 Development Cycle	21
1.5 Fundamentals of Drift Tube Ion Mobility Spectrometry.....	22
1.6 Applications of Drift Tube Ion Mobility	23
CHAPTER 2. REACTION SCREENING FROM 96-WELL PLATES USING A MODIFIED 3D PRINTER	24
2.1 Introduction	24
2.2 Experimental.....	25
2.2.1 Commercial 3D Printer Modifications	25
2.2.2 Mass Spectrometry	26
2.2.3 Data Analysis	27
2.2.4 Reagents and Supplies.....	27
2.3 Results and Discussion	28
2.3.1 Liquid Handling	28
2.3.2 Carryover.....	30
2.3.3 Screening of the Suzuki Cross Coupling Reaction	30
2.3.4 Amine Alkylation and Automated MS/MS Acquisition	32
2.3.5 Katritzky Transamination.....	34
2.4 Conclusions	36
CHAPTER 3. TURNING AND FOCUSING OF IONS AT ATMOSPHERIC PRESSURE...	37
3.1 Introduction	37
3.2 Experimental.....	38

3.2.1	3D Printing	38
3.2.2	SIMION Simulations.....	38
3.2.3	Electronics	39
	Turning Devices	39
	Ion Funnel Devices.....	41
3.2.4	Affixing the Mesh to the Electrode	41
3.2.5	Chemicals	43
3.2.6	Ionization.....	43
3.3	Results and Discussion	43
3.3.1	Drift Tubes with One Turn	43
3.3.2	Drift Tube with Two Turns	45
3.3.3	Non-uniform Electric Fields for Ion Focusing at Ambient Pressure.....	49
3.3.4	Conclusions	55
CHAPTER 4. FOURIER TRANSFORM ION MOBILITY/MASS SPECTROMETRY FOR RECOGNITION OF RELATED COMPOUNDS		56
4.1	Introduction	56
4.2	Experimental Methods.....	57
4.2.1	Chemicals	57
4.2.2	3D Printed Ion Mobility Spectrometer	58
4.2.3	Electronics	59
4.2.4	Mass Spectrometry	60
4.2.5	Fourier Transform Ion Mobility Operation	60
4.3	Results and Discussion	61
4.3.1	Characterization of Plastic IMS in Fourier Transform Mode	61
4.3.2	FT-IMS-CID of TAA Cations.....	63
4.3.3	Separation and Fragmentation of Drugs of Abuse	66
4.3.4	Separation of Explosives	71
4.3.5	Optimization of Ion Gates	73
4.4	Conclusions	76

CHAPTER 5. COUPLING OF ATMOSPHERIC DRIFT TUBE ION MOBILITY WITH TWO-DIMENSIONAL TANDEM MASS SPECTROMETRY	78
5.1 Introduction	78
5.2 Experimental.....	78
5.2.1 Chemicals	78
5.2.2 Drift Tube Ion Mobility.....	79
5.2.3 Mass Spectrometry and 2D MS/MS.....	80
5.3 Results and Discussion	81
5.3.1 MS/MS Selective Ion Mobility Spectra for Lipids	84
5.3.2 Separation of Isobars Prior to 2D MS/MS by Ion Mobility Spectrometry	86
5.4 Conclusions	87
REFERENCES	88
VITA.....	101
LIST OF PUBLICATIONS	102

LIST OF TABLES

Table 2.1. Accuracy in volume delivery of syringe driven by 3D printer extruder motor	28
Table 3.1 Comparison of drift time and resolving power for straight drift tube versus chicane with 18 separated electrodes. (C_m refers to the tetraalkylammonium cation with m-carbon alkanes). 48	48
Table 3.2 Linearly increasing resistances generated a non-uniform (linear) electric field in to generate a focusing electric field.	51
Table 3.3 Quadratically increasing resistances generated a non-uniform (quadratic) electric field in order to generate a stronger focusing field.	51
Table 3.4 Ion current measurements for 12 and 16 electrode geometry collected for each voltage configuration using nESI of 100 μ M each solution of $C_2 - C_8$ TAAs.	52
Table 3.5 Following a region of uniform electric field and electrode diameter, quadratically increasing resistance were used to generate a non-uniform electric field.....	54
Table 4.1 Operating parameters for the bipolar ion mobility spectrometer.	59

LIST OF FIGURES

Figure 1.1 FDM 3D printer consisting of motors to move the extruder in three dimensions (x , y , z) and a fourth motor to feed plastic into the hot extruder. The motors move the extruder in two dimensions to trace out a single layer and then the z axis moves up a small amount to begin the next layer.....	20
Figure 1.2 Development of drift tubes began with designing the device in a CAD software. Electrode geometries are imported into SIMION for simulating ion trajectories. Drift tubes were 3D printed and then tested experimentally. Depending on the results, the drift tube may be redesigned and the cycle began again.	21
Figure 2.1. Schematic showing the (a) front view of the custom syringe assembly and (b) back view of the custom syringe assembly. Note the custom printed bed holds either two 96-well microtiter plates, or one microtiter plate and other items.	25
Figure 2.2 Photos of (a) the device in its home position in front of the mass spectrometer, (b) the custom syringe assembly moved to the spray position, and (c) a closeup of the syringe in the spray position showing the 90° bent capillary.....	26
Figure 2.3 Microtiter plate for catalyst loading experiments was pipetted using this pattern in which each reagent was pipetted directly into the appropriate well. Reagents were stored in 4 mL vials and each syringe addition could fill 8 wells. Syringe was only washed when the reagent was changed. The full well plate was completed in approximately 40 minutes.	29
Figure 2.4. Alternating wells were filled with 1 μ M rhodamine B (m/z 443) and a methanol blank. The heatmap is a plot of m/z 443 intensity with the colors plotted on a log scale. Significant carryover was observed when no wash was completed between analyses, and one wash may be sufficient between scans to eliminate carryover.	30
Figure 2.5 Heatmap of normalized intensity of the product ion (observed as $[M - H]^-$ at m/z 169) for various halides, (a) 2 equivalents base and 1% catalyst, and (b) various catalyst loadings with 2 equivalents of trimethylamine. Each reaction mixture was run in duplicate with each adjacent well containing the same reaction mixture.	31
Figure 2.6. Reaction of benzylamine (4) and benzyl bromide (A) was observed to be fastest in acetonitrile solvent. (a) The single alkylation product (4 + A) was observed as well as (b) the double alkylation product (4 + 2A).....	33
Figure 2.7 MS/MS data was acquired automatically for each well to confirm the identity of the desired product. (a) MS/MS fragmentation of the single alkylation product and (b) MS/MS fragmentation of the double alkylation product is shown for the reaction of benzylamine and benzyl bromide.....	33

Figure 2.8. (a) Heatmap of product to starting material ratios for each para-substituted aniline for the Katritzky transamination reaction run in acetonitrile. (b) Hammett plot versus σ_p^+ constants and (c) σ_p Hammett plot versus σ_p constants. The electrophilic substituent constant σ_p^+ shows a log-linear relationship, while the classic Hammett constants σ_p show a semi-log-linear relationship. 35

Figure 3.1 Flow chart of designs for (a) single turn drift tubes and (b) two turn drift tubes. The total number of electrodes is given for each design. The straight drift tube with the same path length as single turn drift tubes had 45 total electrodes. The straight drift tube with the same path length as the two turn drift tubes had 59 electrodes. The two separated 90° electrode chicane and hairpin systems showed no ion transmission in simulations and were not fabricated. 40

Figure 3.2 An image (a and d) of two meshes taken and (b and e) cropped to only contain the mesh and then (c and f) converted to black and white pixels using Adobe Photoshop. The number of white versus total number of pixels was counted using MATLAB to give a percent transmission. The difficulty in aligning the two meshes is seen from the variability in optical transmission for two different meshes. 41

Figure 3.3 (a) Orthographic projection of mesh application device. (b) A strip of mesh material was clamped by the two pieces of foam (blue) and polyimide tape is applied to the top and bottom edges of the mesh material. (c) One clamp was removed, the mesh was cut to the shape of the electrode, and that side was taped to the electrode with polyimide tape. (d) The second clamp was removed, and the final side is fixed to the electrode with polyimide tape. The overhanging tape is then trimmed with a razor blade. 42

Figure 3.4 Renderings of (a) straight drift tube with same path length as single turn drift tubes, turns with (b) two consecutive 45° electrodes, (c) two separated 45° electrodes, and (d) nine separated 10° electrodes. Histogram of drift times from SIMION trajectory simulations for (e) straight drift tube, turns with (f) two consecutive 45° electrodes, (g) two separated 45° electrodes, and (h) nine separated 10° electrodes. Experimental results with C₂, C₄, C₆, and C₈ tetraalkylammonium salts for (i) straight drift tube, turns with (j) two consecutive 45° electrodes, (k) separated 45° electrodes, and (l) nine separated 10° electrodes. 44

Figure 3.5 Electric field strength (V/mm) calculated from SIMION of a single turn using (a) two consecutive 45° turning electrodes, (b) two separated 45° turning electrodes, and (c) nine separated 10° turning electrodes. 45

Figure 3.6 Renderings of (a) straight drift tube with same path length as hairpin drift tubes, hairpin with (b) two turns with two consecutive 45° electrodes, (c) four turns with separated 45° electrodes, and (d) 18 separated 10° electrodes. Histogram of SIMION trajectory simulations for (e) straight drift tube, hairpin with (f) two turns with two consecutive 45° electrodes (g) four turns with separated 45° electrodes, and (h) 18 separated 10° electrodes. Experimental results with C₂, C₄, C₆, and C₈ tetraalkylammonium salts of (i) straight drift tube, hairpin with (j) two turns with two consecutive 45° electrodes, (k) four turns with separated 45° electrodes, and (l) 18 separated 10° electrodes. 46

Figure 3.7 Renderings of chicane drift tube with (a) two turns with two consecutive 45° electrodes, (b) four turns with separated 45° electrodes, (c) two turns with 18 consecutive 10° electrodes, and (d) 18 separated 10° electrodes. Histogram of drift times from SIMION trajectory simulations for chicane with (e) two turns with two consecutive 45° electrodes, (f) four turns with separated 45° electrodes, (g) two turns with 18 consecutive 10° electrodes, and (h) 18 separated 10° electrodes. Experimental results with C₂, C₄, C₆, and C₈ tetraalkylammonium salts for chicane with (i) two turns with two consecutive 45° electrodes, (j) four turns with separated 45° electrodes, (k) two turns with 18 consecutive 10° electrodes, and (l) 18 separated 10° electrodes. 47

Figure 3.8 Electric field strength (V/mm) calculated from SIMION of the chicane with (a) two turns with two consecutive 45° electrodes, (b) four turns with separated 45° electrodes, (c) two turns with nine consecutive 10° electrodes, and (d) 18 separated 10° electrodes. 48

Figure 3.9 (a) Color map showing electric field calculated for equal resistances from SIMION with equipotential lines overlaid. Straight equipotential lines mean that ions are not focused to the center to be transmitted. (b) Ion trajectories from SIMION for ion funnel geometry with equal resistances (linear voltage drop) between each electrode. (c) Color map showing electric field for linear resistance increase between electrodes calculated from SIMION with equipotential lines overlaid. Curved equipotential lines mean the ions are focused to the center of the drift tube and are transmitted. (d) Ion trajectories from SIMION for ion funnel geometry with linear resistance increase between electrodes (non-linear voltage drop) between each electrode. (e) Color map showing electric field for square resistance increase between electrode calculated from SIMION with equipotential lines overlaid. (f) Ion trajectories from SIMION for ion funnel geometry with square resistance increase between electrode (non-linear voltage drop) between each electrode. 50

Figure 3.10 (a) Electric field and equipotential lines and (b) ion trajectory simulation for ion funnel geometry with square resistance increase (non-linear voltage drop) between each electrode. (c) Electric field and equipotential lines and (d) ion trajectory simulation for ion funnel geometry with square resistance increase (non-linear voltage drop) between each electrode with added mesh denoted by the red dotted line. (e) Electric field and equipotential lines and (f) ion trajectory simulation for ion funnel geometry with an initial region of linear voltage drop and square resistance increase (non-linear voltage drop) between each electrode. (g) Electric field and equipotential lines and (h) ion trajectory simulation for ion funnel geometry with an initial region of linear voltage drop and square resistance increase (non-linear voltage drop) between each electrode and added mesh denoted by red dotted line. 53

Figure 3.11 (a) Electric field lines for the previously described ion funnel geometry with square resistance increase between electrodes compared with (b) electric field lines for proposed geometry with thicker electrodes and reduced inter-electrode spacing. The defocusing fields appear improved and will potentially offer improved ion transmission. 55

Figure 4.1 (a) Schematic of the 3D printed ion mobility device with ion gating performed by applying square waveforms to two sets of steel meshes at each end of the 31 drift lens spectrometer. The cylindrical extrusion can be seen on the first (focusing) electrode. Steel meshes are placed directly on the 3D printed electrodes. (b) Sweep voltages used to simultaneously open and close both gates with linearly increasing frequency. (c) Fourier transform of the ion chronogram gives the ion frequency distribution, which is converted into arrival time, i.e. the ion mobility spectrum, by division by the sweep rate. (d) Ion mobility spectrometer was placed directly in front of the mass spectrometer capillary inlet. Fragmentation (denoted by a red asterisk) can be made in either the source region or in the ion trap. 58

Figure 4.2 Ion mobility spectra for TAA cation mixture ($C_2 - C_8$) recorded using gate frequency sweeps: 5 – 2005 Hz (red), 5 – 3005 Hz (blue), and 5 – 7005 Hz (green). (b) Ion chronograms for the C_6 TAA for each frequency sweep show an increase in arrival frequency with sweep rate. (c) Ion chronograms for the C_2 , C_5 , C_8 TAA cation for the 5 – 3005 Hz frequency sweep show an increase in arrival frequency for ions with lower mobility. (d) Calculated resolving power for each TAA cation for each frequency sweep showing a decrease in resolving power at faster sweep rates. 62

Figure 4.3 (a) Use of a 100 m/z window allowed isolation of the C_6 and C_7 TAA cation in the ion trap. (b) Excitation occurred at a secular frequency corresponding to the average mass. Fragment ions (generated in the ion trap) of each TAA cation had the same drift time as the precursor ion, as can be seen in the ion mobility spectrum. (c) Ion mobility spectrum of only the C_6 precursor and product ions showing that all peaks have the same drift time. (d) Ion mobility spectrum of only the C_7 precursor and product ions showing again that both peaks have the same drift time. 64

Figure 4.4 (a) Reconstructed mass spectrum using CID from the Fourier transform ion mobility spectrum of each ion. (b) Isolation and fragmentation of the C_6 TAA cation in the ion trap without ion mobility. (c) Isolation and fragmentation of the C_7 TAA cation in the ion trap without ion mobility. The CID mass spectrum shows product ions belonging to both precursors which can be identified using ion mobility information. 65

Figure 4.5 (a) Ion mobility spectra using in-source fragmentation of amphetamine (m/z 136) and its fragments m/z 119 and m/z 91 and MDEA (m/z 208) and its fragments m/z 163, m/z 135, m/z 133, m/z 105, and m/z 72. (b) Ion chronograms for precursor ions amphetamine and MDEA showing differences in arrival frequency corresponding to their differences in drift time. (c) Ion mobility spectra from the same data for only amphetamine and its fragment showing that all peaks have the same arrival time. (d) Ion chronograms for amphetamine and its fragment ions showing again that the ions of m/z 119 and m/z 91 maintain the frequency of the amphetamine precursor. (e) Ion mobility spectra (from the same data) for only MDEA and its fragment showing that all peaks have the same arrival time. (f) Ion chronograms for MDEA and its fragments again showing that the fragment ions maintain the frequency of the MDEA precursor. 67

Figure 4.6 (a) Reconstructed in-source mass spectrum with in-source fragmentation from the Fourier transform for amphetamine, MDEA, and their detected fragments. (b) Full scan mass spectrum of amphetamine with source fragmentation without ion mobility showing amphetamine and its product ions. (c) Full scan mass spectrum of MDEA with source fragmentation without ion mobility showing MDEA and its product ions. Product ions coming from either amphetamine or MDEA can be identified with ion mobility information. 68

Figure 4.7 (a) MS² of amphetamine (b) MS³ of amphetamine and *m/z* 119 (c) MS² of MDEA (d) MS³ of MDEA and *m/z* 163 69

Figure 4.8 (a) Ion mobility spectra using in-source CID for 4-fluoroisobutyrylfentanyl (*m/z* 369), acetyl fentanyl (*m/z* 323), their fragment *m/z* 188, acetyl norfentanyl (*m/z* 219), and its fragment *m/z* 84. (b) Ion mobility spectra (from the same data) of only 4-fluoroisobutyrylfentanyl, acetyl fentanyl, and their fragment *m/z* 188. This fragment ion shows two peaks corresponding to the drift time of both of its precursors. (c) Ion mobility spectra (from the same data) of acetyl norfentanyl and its fragment *m/z* 84 showing that both peaks have the same arrival time. (d) Ion chronograms for 4-fluoroisobutyrylfentanyl, acetyl fentanyl, and their fragment *m/z* 188 showing that the product ion frequency is a combination of both precursor ion frequencies. (e) Ion chronograms for acetyl norfentanyl and its product ion *m/z* 84 showing that the product ion maintains the frequency of the acetyl norfentanyl precursor. 70

Figure 4.9 (a) Ion mobility spectra of trinitroglycerin chloride adduct (*m/z* 262,264), trinitroglycerin NO₃ adduct (*m/z* 289), HMX chloride adduct (*m/z* 331,333), HMX NO₃ adduct (*m/z* 358) and HMX dimer chloride adduct (*m/z* 627,629). (b) Ion chronograms for all ions. Low signal intensity for this measurement shows that poor signal intensity gives rise to artifacts in the Fourier transform, i.e. the ion mobility spectrum. 72

Figure 4.10 Simulation of Tyndall-Powell gate with inter-mesh distance of 900 μm vs 300 μm for various injection times. Ion initial positions were diagonal behind the first mesh. For the 300 μm inter-mesh distance even at the shortest injection time ions were able to pass through the gate whereas all ions are blocked for a 100 μs injection time with a 900 μs inter-mesh distance. 73

Figure 4.11 Fabrication of a 3D printed holder capable of sub-1 mm inter-mesh distance required the removal of the divider between those two electrodes and thicker electrodes to fill the space. 74

Figure 4.12 (a) Ion intensity and resolving power for a 900 μm inter-mesh distance for a voltage difference of 100 V and 200 V. (b) Ion intensity and resolving power for a 900 μm inter-mesh distance for a voltage difference of 100 V and 200 V. In both cases, both voltage and distance decrease the minimum gate opening time for which ion signal is observed. 75

Figure 4.13 (a) Ion chronogram for TAA cations for a gate two blocking voltage of 500 V (blue) versus 325 V (red) for stainless steel mesh sheets. (b) Ion chronogram for TAA cations for gate two blocking voltage of 500 V (blue) versus 325 V (red) for MN17 nickel mesh. 76

Figure 5.1. Ion mobility coupled with full scan MS gives mobility and mass information. By fragmenting ions in the source, related precursors and products were identified by their drift time. Ion mobility with 2D MS/MS gives mobility and the entire MS/MS data domain. 81

Figure 5.2 Individual 2D MS/MS spectra collected at various drift times where the (a) C ₃ , (b) C ₅ , and (c) C ₇ TAA are the base peaks.	82
Figure 5.3 Ion mobility spectrum plotted from 2D MS/MS extracted ion intensities. The mobility spectrum is nearly identical to data collected with full scan MS but with additional MS/MS information collected in the same experiment.	83
Figure 5.4. (a) Total 2D MS/MS spectrum of a lipid mixture showing characteristic fragments of <i>m/z</i> 184 for the two PCs and a characteristic neutral loss of 141 Da for the two PEs. Data projection and extraction give the mass spectra for each of the scan lines.....	84
Figure 5.5 (a) Extracted product ion scan lines gives the ion mobility spectrum for each lipid. (b) Extracted neutral loss scan line gives an ion mobility spectrum of only the PEs in the mixture (dotted line) and extracted precursor ion scan line gives the ion mobility spectrum of the PCs in the mixture (solid line).....	85
Figure 5.6. (a) Total 2D MS/MS spectrum of mixture of puromycin and terfenadine. Each compound shows a characteristic fragment, but since they are isobaric they cannot be distinguished from one compound with two fragments in 2D MS/MS. (b) Extracted normalized ion intensities for each MRM give the ion mobility spectrum for each compound.	86

LIST OF SCHEMES

Scheme 2.1. Suzuki cross-coupling of 4-hydroxyphenylboronic acid (1) with various alkyl benzenes (2a-d) to form 4-phenylphenol (3).	31
Scheme 2.2 Alkylation of various amines (4-7) by a halide (A-C) to form a single alkylation product. Reaction can potentially form a double alkylation product.	32
Scheme 2.3 Reaction of 2,4,6-triphenylpyrilyum tetrafluoroborate (8) with various para-substituted anilines (9a-e) to form a pyridinium product (10a-e).....	34

ABSTRACT

Advancements in 3D printing technology have provided (1) easy access to low-cost, open-source robotics, and (2) a fast fabrication technique for analytical devices among others. Using the robotics of a 3D printer, a mass spectrometry-based reaction screening device was built as a low-cost, modest throughput alternative to expensive, very fast systems. Using the 3D printer for fabrication, ion mobility devices were fabricated. Fundamental studies of the motion of ions in these devices were performed in addition to applications of ion mobility-mass spectrometry using a 3D printed drift tube ion mobility spectrometer.

With only simple modification, 3D printer kits provide nearly all the necessary parts for a functional reaction screening device. Replacing the hotend assembly with custom parts to hold a syringe, precise volumes of reaction mixtures can be dispensed, and high voltage applied to the needle for direct analysis of solutions by mass spectrometry. Direct analysis of reaction mixtures in a 96-well microtiter plates was completed in approximately 105 minutes (~65 seconds per reaction mixture, including washing of syringe). Following analysis, product distributions derived from the electrospray mass spectra were represented as heatmaps and optimum reaction conditions were determined. Using low-cost, open-source hardware, a modest throughput for reaction screening could be achieved using electrospray ionization mass spectrometry.

The manipulation of ions at reduced pressures is very well understood, whereas the efficient manipulation of ions at atmospheric pressure is far less understood. Using 3D printing, multiple iterations of atmospheric pressure drift tube ion mobility spectrometers were fabricated with one and two turns in the drift path. Optimum electrode geometries for ion transmission and resolution were determined by both simulation and experiment. Racetrack effects, where ions on the inside of turns have a shorter path than ions on the outside, were determined to be highly detrimental to resolving power. Drift tubes with two turns in opposite directions (a chicane) corrected for racetrack effects and had only marginally poorer resolving power than a straight drift tube. Additionally, ion intensities were nearly identical between optimized straight and turned ion paths, showing that these manipulations can be done with high efficiency. The focusing of ions at reduced pressure using RF ion funnels at reduced pressure can have nearly 100 percent transmission. At atmospheric pressure, RF fields are not nearly as efficient at focusing ions. By using non-uniform

DC fields at atmospheric pressure, ions can be focused, but not nearly to the extent as at reduced pressure.

The coupling of atmospheric pressure drift tube ion mobility with ion trap mass spectrometry is inefficient due to the mismatch in duty cycle between the two instruments. For this reason, increasing the amount of data collected from a single experiment is of high importance. Fourier transform ion mobility increases the duty cycle from less than 1% to 25%. When ions are fragmented in the mass spectrometer, they maintain the frequency characteristic of the precursor. Therefore, ions can be fragmented without isolation in the ion trap (reducing duty cycle further) and related precursors and product ions identified through their drift time. Two-dimensional tandem mass spectrometry is a method to collect all tandem mass spectrometry information in a single scan. When coupled with ion mobility, this data can be used to generate functional group-specific ion mobility spectra where ion intensity is measured along a precursor or neutral loss scan line. This was demonstrated for a lipid sample in which head-group specific ion mobility spectra were obtained using head-group specific precursor and neutral loss scan lines.

CHAPTER 1. INTRODUCTION

1.1 Overview

Successfully building an ion manipulation device requires both the fundamental knowledge of the motion of ions in electrostatic fields and the ability to manufacture electrodes of the desired shape. For example, even though hyperbolic rods give the optimal electric field, round rods have often been used to approximate hyperbolic surfaces due to difficulty in machining complex shapes.¹ After successfully machining one set of Orbitrap rods, it took Alexander Makarov and his team many years to repeat the feat.² The major focus of this dissertation is the use of additive manufacturing techniques to fabricate ion manipulation and focusing devices and then to use them as analytical devices. In addition, a 3D printer was used as a prefabricated robot to be converted to a high throughput reaction sampling device.

1.2 Additive Manufacturing

Additive manufacturing, also referred to as 3D printing, is the technique of producing 3D objects by building them up layer-by-layer. This is in contrast to traditional milling in which material is removed (often layer-by-layer) to produce the desired product. The most common type of 3D printer used by hobbyists and scientists alike is known as fused deposition modeling (FDM).

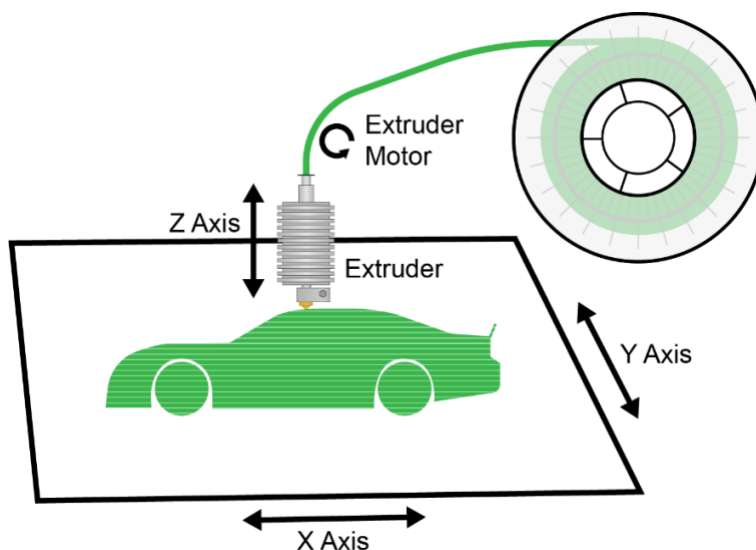


Figure 1.1 FDM 3D printer consisting of motors to move the extruder in three dimensions (x , y , z) and a fourth motor to feed plastic into the hot extruder. The motors move the extruder in two dimensions to trace out a single layer and then the z axis moves up a small amount to begin the next layer.

3D printers of this type consist of a platform with 3-axis motion control. Solid plastic is fed into a heated nozzle; molten plastic is extruded, cools, and hardens in the appropriate pattern on the build plate.^{3,4} As the first layer cools and hardens, the z -axis is raised a small amount (< 0.2 mm) and the subsequent layer is added. This process continues until the entire model is complete (Figure 1.1).

Two of the most common 3D printing materials are polylactic acid (PLA) and acrylonitrile butadiene styrene (ABS).⁵ ABS is more difficult to work but is useful due to its higher temperature tolerance. Managing temperature is very important when printing ABS to reduce the potential for model warping. The addition of conductive materials such as carbon black powder (Proto-pasta) make these plastics conductive.

Stereolithography (SLA) is another 3D printing technique, which instead of a thermoplastic, uses a photo-curable resin that is hardened by a laser or projector of the appropriate wavelength working layer-by-layer.⁶ 3D printers of this type are able to achieve higher resolutions than most FDM printers, which is necessary in some analytical chemistry applications.

1.3 Additive Manufacturing in Mass Spectrometry

Outside the mass spectrometer, FDM 3D printing can quickly fabricate useful devices. Paper spray⁷⁻⁹ is a useful ambient ionization¹⁰ technique for the analysis of samples in complex mixtures. 3D printed cartridges¹¹⁻¹³ can be quickly fabricated to provide features for optimal signal intensity and increased spray time. One can even spray directly from a 3D printed cone.¹⁴ Holders necessary for attaching ambient ionization sources to a mass spectrometer can be easily 3D printed, such as for desorption electrospray ionization (DESI)¹⁵ or low temperature plasma (LTP).¹⁶

Inside the mass spectrometer, SLA 3D printing is preferred. Cured resin parts are coated with conductive surfaces to produce mass analyzers. Examples include quadrupole mass filters¹⁷, hyperbolic linear ion traps¹⁸, and circular arrays of rectilinear ion traps.¹⁹ Though the direct 3D printing of metal is possible,²⁰ the resolution is not currently possible to meet the high demands of some mass spectrometry devices.²¹

1.4 Development Cycle

Analytical instrument development using 3D printing when compared to traditional machining lends itself to a rapid development cycle in which design changes can be quickly tested because of the speed of manufacturing.

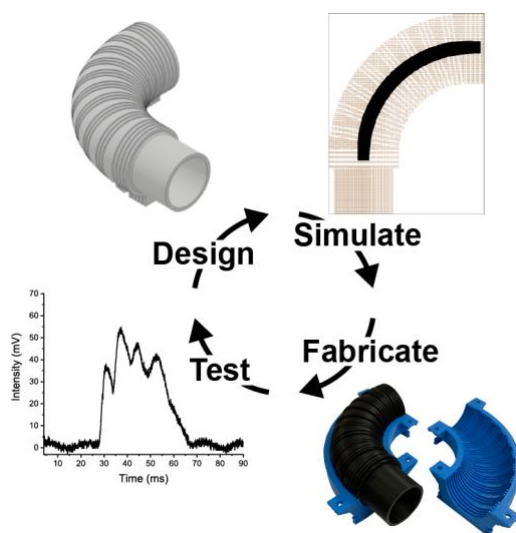


Figure 1.2 Development of drift tubes began with designing the device in a CAD software. Electrode geometries are imported into SIMION for simulating ion trajectories. Drift tubes were 3D printed and then tested experimentally. Depending on the results, the drift tube may be redesigned and the cycle began again.

After deciding on a potential design, the first step of building an ion manipulation device is design using a CAD software, such as Autodesk Inventor. This geometry is imported into an ion trajectory simulation software, such as SIMION. After simulation, if the desired performance is achieved, the device can be fabricated with FDM 3D printing. If the desired performance is not achieved in the simulation, then the cycle begins again with a new design without fabrication. After fabrication of the device and the associated voltage divider, the testing can begin. The fabrication time varies depending on the size of the device, but the case can be printed in approximately 6 hours (printed in two halves) and each electrode (depending on diameter) can be printed in approximately 8 – 12 minutes. Therefore, the entire device can be completed in approximately 7 – 8 hours. After testing the device, the design can be revised, and the entire cycle can begin again.

1.5 Fundamentals of Drift Tube Ion Mobility Spectrometry

An ion traveling through a drift tube at atmospheric pressure collides with a very large number of gas molecules while being accelerated by the electric field. The velocity of ions in an electric field is directly proportional to the magnitude of the electric field (provided E is below the low field limit).^{22, 23} The equation for the average velocity is

$$v_d = KE$$

where v_d is the velocity, E is the electric field, and K is a constant (mobility). This equation can be rewritten using the drift length and voltage as

$$\frac{L}{t_d} = K \frac{V}{L}$$

$$K = \frac{L^2}{V t_d}$$

where L is the drift length, V is the drift voltage, and t_d is the drift time. In order to compare mobility measurements taken under different conditions, mobility spectra are often reported using the reduced mobility K_0 which has the equation:

$$K_0 = \frac{P}{760} \frac{273}{T} K$$

where P is the pressure in torr and T is the temperature in Kelvin. K_0 is reported with the units cm^2/Vs .

Drift tube ion mobility is dependent on the balance of the electric field pushing the ions forward and their collisions with gas molecules pushing them backward. The equation for the collision cross section is given by²⁴

$$K = \frac{3}{16} \left(\frac{2\pi}{\mu k_B T} \right)^{1/2} \frac{ze}{N \Omega}$$

where μ is the reduced mass of the ion-gas pair, k_B is Boltzmann's constant, T is temperature, z is the number of charges, e is the elementary charge, N is the number density and Ω is the collision cross section. By combining the two equations for K , the collision cross section can be determined directly from the drift time:

$$\Omega = t_d \frac{3}{16} \left(\frac{2\pi}{\mu k_B T} \right)^{1/2} \frac{ze V}{N L^2}$$

Large databases of collision cross section measurements have been published for large and small molecules.²⁵⁻²⁷

1.6 Applications of Drift Tube Ion Mobility

Drift tube ion mobility spectrometers have applications as both a standalone spectrometer and coupled to mass spectrometers. Standalone drift tube ion mobility is most often used for the detection of small molecules such as chemical warfare agents,²⁸⁻³¹ drugs of abuse,^{32, 33} and explosives^{34, 35}. Since ion mobility can be operated at atmospheric pressure, the size of the devices can be smaller than a miniature mass spectrometer.^{36, 37}

Analytical techniques that separate molecules (or their ions) have been coupled to mass spectrometers for decades. Drift tube ion mobility spectrometers were first coupled to a magnetic sector mass spectrometer,³⁸ though modern instruments most often use a time-of-flight mass spectrometer.^{39, 40} A major application of drift tube ion mobility mass spectrometry is the separation of biomolecules.^{25, 41} Due to their ability to fold, gas phase protein structures can exist multiple conformational states of the same m/z but different collision cross section.⁴² IMS-MS offers increased peak capacity for the identification of peptides versus MS alone, though not yet to the performance of LC-MS.⁴³ Drift tube ion mobility also has utility in the identification and separation of small molecules.^{44, 45}

CHAPTER 2. REACTION SCREENING FROM 96-WELL PLATES USING A MODIFIED 3D PRINTER

Portions of this work have been published in the journal *Analyst* as the article: “Schrader, R. L.; Ayrton, S. T.; Kaerner, A.; Cooks, R. G. High Throughput, Low Cost Reaction Screening using a Modified 3D Printer. *Analyst*, **2019**, *144*, 4978-4984.”

2.1 Introduction

The combination of modern robotics and analytical instrumentation has allowed for the rapid preparation and analysis of reaction mixtures. These experiments require less effort per reaction mixture than traditional analytical methods.⁴⁶ High-throughput experimentation (HTE) utilizing mass spectrometry has been used in many areas such as biochemistry⁴⁷, drug discovery^{48, 49}, and catalysis^{50, 51}. HTE has been applied to organic synthesis for the optimization of known reactions⁵²⁻⁵⁷ as well as the discovery of new ones.⁵⁸

Chromatography-based high-throughput screening (HTS) systems in the microtiter format can have throughputs of 5 – 22 s per sample.⁵⁹ The Agilent RapidFire™ system is a high throughput screening system coupled to SPE-MS with a sample throughput of ~8 s per sample.⁶⁰ Other systems forgo chromatography, such as those using desorption electrospray ionization⁵³ or acoustic droplet ejection⁶¹ and offer higher throughputs. Most such systems use mass spectrometry for analysis, although optical methods are also used.⁶² Here, we use an electrospray ionization (ESI) based method by applying a high voltage directly to the metal needle of a glass syringe for direct MS analysis of reaction mixtures. While the value of HTE is clear, the tools required to perform these experiments are expensive, making it difficult for most investigators to utilize it.

Analytical chemistry has long embraced new technologies with examples from across the subject.⁶³⁻⁶⁷ Three-dimensional printing (3D printing) technology has developed greatly over the past few years and has made a great impact in chemistry.^{4, 68} The commercial 3D printer offers an easy-to-use platform for modification to perform tasks requiring simple robotics, for example a MALDI matrix application using a modified 3D printer.⁶⁹ Here we have utilized a Delta 3D printer, which utilizes three stepper motors at the base arranged in an equilateral triangle to move a hot extruder in the *x*, *y*, and *z* dimensions. A typical Cartesian 3D printer uses stepper motors to directly control each axis. This hot extruder was replaced with a glass syringe whose plunger was

controlled by an additional stepper motor (the “extruder” motor). Printers of this type are low cost and the additional parts necessary for modifications made can be purchased for an additional low cost. After calibration and optimization, this system was used to prepare 96-well microtiter plates with reaction being followed by analysis of products by mass spectrometry.

2.2 Experimental

2.2.1 Commercial 3D Printer Modifications

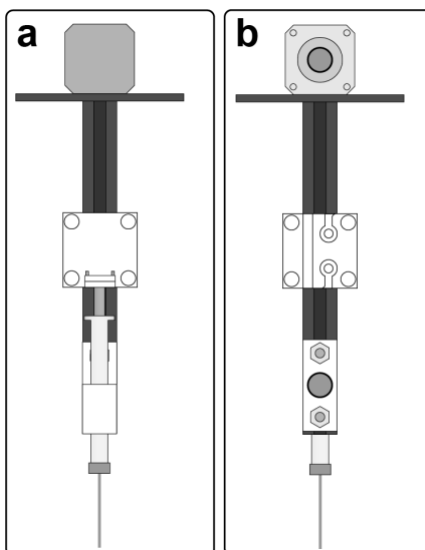


Figure 2.1. Schematic showing the (a) front view of the custom syringe assembly and (b) back view of the custom syringe assembly. Note the custom printed bed holds either two 96-well microtiter plates, or one microtiter plate and other items.

The hotend assembly was removed from an assembled AnyCubic Kossel 3D printer (Guandong, China) and replaced with a 250 μ L Hamilton 750 series syringe with removable needle (Reno, NV). The needle length is 51 mm with an inner diameter of 0.15 mm and outer diameter of 0.72 mm. A short height NEMA 17 motor from OMC Corporation (Nanjing City, China) was held in place with a custom 3D printed bracket. The syringe was attached to a 125 mm beam from MakerBeam (Utrecht, Netherlands) with a custom 3D printed bracket and the syringe plunger controlled by the stepper motor through a timing belt. These modifications are described in Figure 2.1. The stock 3D printer firmware was modified with a dummy temperature to allow for movement of the extruder motor. All 3D printed pieces were designed in-house with Autodesk

Inventor (San Rafael, CA), converted to STL, and 3D-printed using a Mendelmax 3 (Makers Tool Works, Oklahoma City, OK) with polylactic acid/polyhydroxyalkanoate (PLA/PHA) filament (ColorFabb, Belfeld, Netherlands).

The custom bed was 3D printed with pre-defined holes to place two 96-well plates. Additional holes allow for 20 mL vials and 4 mL vials containing wash solvent or reagent vials for well plate preparation. The x , y , z coordinates of each well was determined and controlled with G-code instructions.

2.2.2 Mass Spectrometry

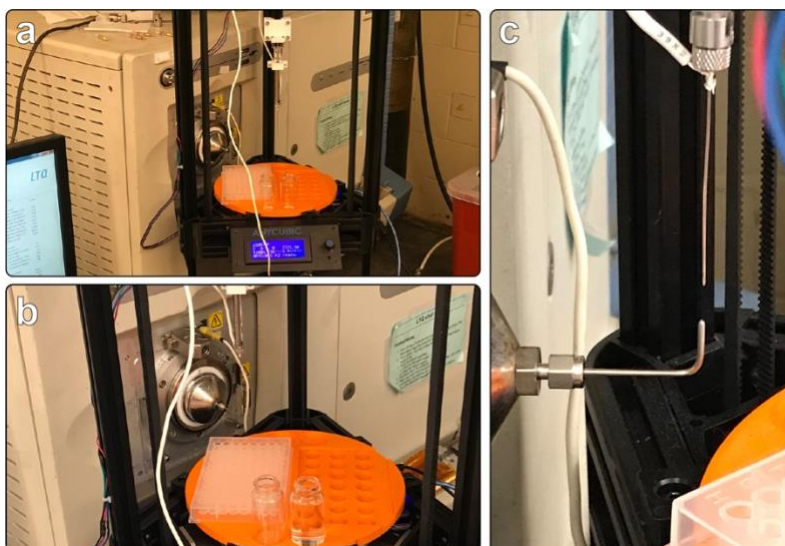


Figure 2.2 Photos of (a) the device in its home position in front of the mass spectrometer, (b) the custom syringe assembly moved to the spray position, and (c) a closeup of the syringe in the spray position showing the 90° bent capillary.

All mass spectrometry measurements were made with a Thermo-Fisher LTQ XL-Orbitrap or LTQ MS (San Jose, CA). An Arduino Uno (Adafruit, New York, NY) was used to supply a contact closure signal to the mass spectrometer by contact with a mechanical endstop (Bigtree Technology, Shenzhen City, China) upon reaching the spray position. The endstop was supported by metal beams (Makerbeam) and 3D printed brackets. Electrospray was generated directly from the syringe needle by applying high voltage (5 kV) to the needle. The standard inlet was replaced with an extended capillary bent 90° such that it was coaxial with the syringe needle in the spray position. Photos of the device operation are given in Figure 2.2. Parameters for the MS were: spray

voltage 4.5 kV, capillary voltage 15 V, tube lens 65 V, and capillary temperature 150 °C and a mass range of m/z 50 – 700.

2.2.3 Data Analysis

Individual wells were saved as individual ‘.RAW’ files by the instrument and were converted to the open-source ‘.mzXML’ format using MSConvert⁷⁰. Individual ‘.mzXML’ files were imported into MATLAB (The MathWorks, Inc., Natick, MA) with the Bioinformatics toolbox. Using a user-supplied table of starting material and product m/z values, mass spectra in which one of these supplied m/z values was not the base peak were automatically removed. This serves to remove both scans in which either noise was a significant portion of the spectrum and those in which no data was collected such that only data representative of the sample well was included. Data from each well was normalized and then displayed as a heat map of intensities across the entire 96-well plate.

2.2.4 Reagents and Supplies

All chemicals were purchased from Sigma-Aldrich (St. Louis, MO). HPLC grade methanol was purchased from Fisher Scientific (Hampton, NH). Microtiter plates were purchased from Greiner Bio-One (Kremsmünster, Austria).

For the Suzuki reaction, solutions were prepared using 40 mM concentrations of the halobenzene and 4-hydroxyphenylboronic acid, using 80 mM for the various bases, and 0.04 – 4 mM for the various catalysts. Aliquots of the appropriate reagents were robotically pipetted into each well and the microtiter plate was sealed with a silicone cover. The reaction mixtures were diluted 100 times in methanol for analysis manually.

For the N-alkylation, both the amine and halide were prepared using 10 mM in methanol, ethanol, acetonitrile, and dioxane. The reagents were pipetted manually into each well of the microtiter plate. The reaction mixtures were diluted 1000 times in methanol for analysis.

For the Katritzky transamination, both the 2,4,6-triphenylpyrilium tetrafluoroborate and five substituted anilines were prepared at 20 mM in acetonitrile. The prepared solutions were pipetted into a microtiter plate manually in quadruplicate. The reaction mixtures were diluted 1000 times in acetonitrile for analysis.

2.3 Results and Discussion

2.3.1 Liquid Handling

Table 2.1. Accuracy in volume delivery of syringe driven by 3D printer extruder motor

Desired Volume	Actual Volume Delivered	Percent Error
50 μL	$51.3 \pm 0.3 \mu\text{L}$	2.70 %
100 μL	$99.3 \pm 0.4 \mu\text{L}$	-0.75 %
150 μL	$149.7 \pm 0.5 \mu\text{L}$	-0.18 %
200 μL	$200.7 \pm 0.7 \mu\text{L}$	0.37 %

The extruder motor was used to control the plunger of a glass syringe. The ability of the device to deliver accurate volumes is directly related to the motion of the stepper motor. The device was calibrated by measuring the volume of water delivered for a specific command distance, for example a 20 unit G-code command resulted in a delivered volume of 90.33 μL . Using the resulting linear calibration, the volume delivery was tested at four different volumes in triplicate (Table 2.1).

An Eppendorf® manual autopipette delivering 100 μL using a 20 – 200 μL tip has a systematic error of $\pm 1.0 \mu\text{L}$, slightly greater than the observed error using the automated device. This demonstrates that a modified 3D printer can be used to prepare 96-well plates from prepared stock solutions with reliable accuracy.

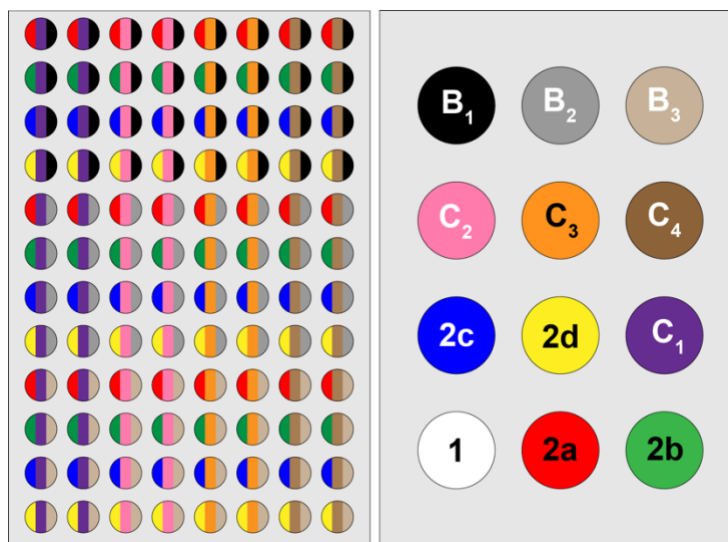


Figure 2.3 Microtiter plate for catalyst loading experiments was pipetted using this pattern in which each reagent was pipetted directly into the appropriate well. Reagents were stored in 4 mL vials and each syringe addition could fill 8 wells. Syringe was only washed when the reagent was changed. The full well plate was completed in approximately 40 minutes.

A program to fill microtiter plates with the appropriate solutions from stock solution was written using G-code. The well plate design for the Suzuki base screening experiment is shown in Figure 2.3. These plate configurations were completed in approximately forty minutes and require no operator intervention. Reagents were stored in 4 mL vials in the pre-cut holes. The syringe drew 200 μL of reagent and deposited 25 μL of reagent per well. The syringe was then washed with methanol solvent before a new reagent was dispensed.

2.3.2 Carryover

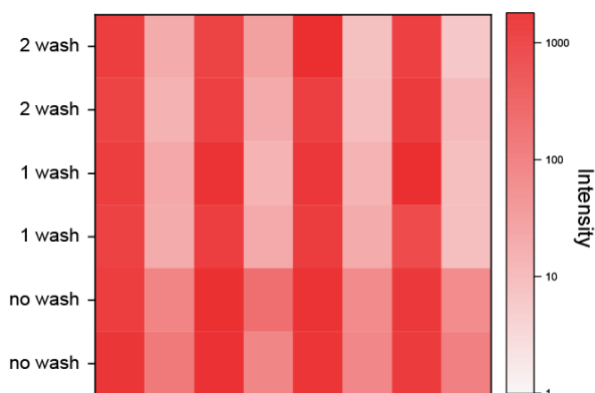


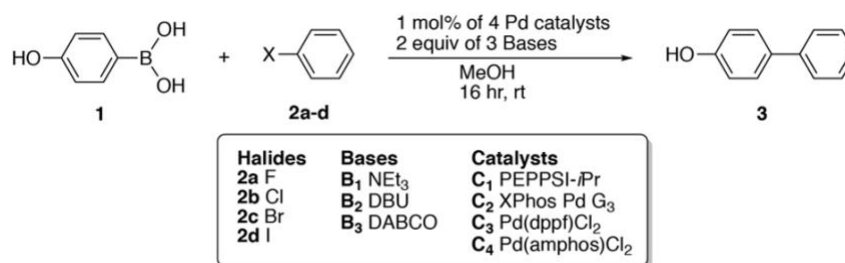
Figure 2.4. Alternating wells were filled with 1 μ M rhodamine B (m/z 443) and a methanol blank. The heatmap is a plot of m/z 443 intensity with the colors plotted on a log scale. Significant carryover was observed when no wash was completed between analyses, and one wash may be sufficient between scans to eliminate carryover.

A concern when using the same syringe for repeated sample injection is carryover between samples. In order to investigate this effect, a well plate was filled with alternating wells of 1 μ M rhodamine B in methanol and pure methanol. For the first 16 wells, the syringe was washed twice with methanol between injection. For the second 16 wells, the syringe was washed only once with methanol. For the final 16 wells, the syringe was not washed between each injection. The resulting heatmap is shown in Figure 2.4. No change in ion intensity at m/z 443 observed in the blank wells between one wash and two. When no wash step was performed between wells, the ion intensity observed at m/z 443 in the blank wells was increased by six-fold. Since the signal intensity is over an order of magnitude larger than the carried over intensity, this suggest that carryover is small, even when no wash step is done.

2.3.3 Screening of the Suzuki Cross Coupling Reaction

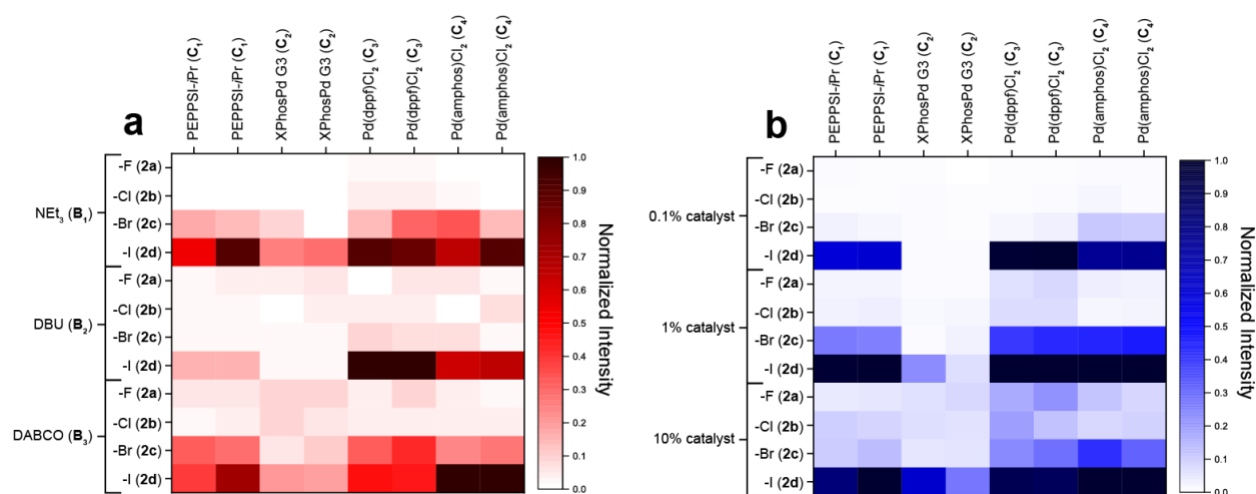
The use of metal catalyzed reactions to form C-C bonds has revolutionized synthetic organic chemistry. For example, the Suzuki cross-coupling forms a carbon-carbon single bond using an organoboron and a halide reagent.^{71, 72} This reaction is especially important in the synthesis of drug targets.⁷³ This reaction has a strong dependence on experimental conditions, so establishing of a reactivity landscape for the reaction is very important,^{57, 74} especially given its

significance in medicinal chemistry.⁷³ Many combinations exist with various leaving groups, bases, solvents, and catalyst.



Scheme 2.1. Suzuki cross-coupling of 4-hydroxyphenylboronic acid (**1**) with various alkyl benzenes (**2a-d**) to form 4-phenylphenol (**3**).

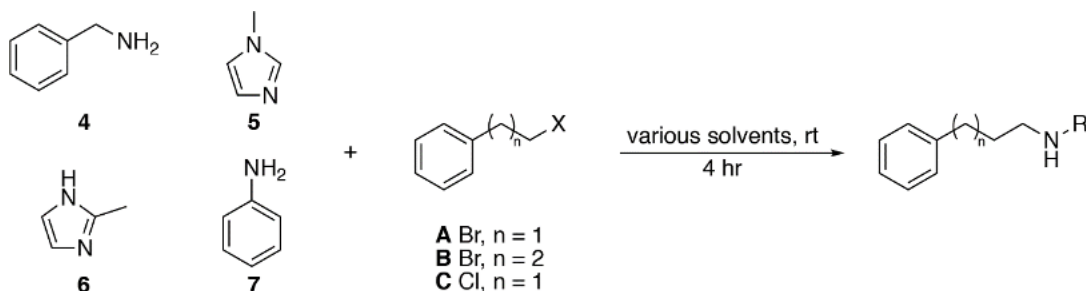
In order to investigate the use of the modified 3D printer as a reaction screening tool, the Suzuki cross-coupling of 4-hydroxyphenylboronic acid (**1**) with various alkyl benzenes (**2a-d**) was studied using four pre-formed, air and moisture tolerant palladium catalysts (PEPPSI-*i*Pr, XPhosPd G₃, Pd(dppf)Cl₂, and Pd(amphos)Cl₂) with triethylamine, DBU, and DABCO base (Scheme 2.1). The reactions mixtures, after preparation, were allowed to sit at room temperature for 16 hours. These reactions are generally heated to decrease the reaction time, but a long, room temperature reaction was chosen for ease of the experiment.



The reactivity landscape of this reaction was tested via a base screen and catalyst loading screen (Figure 2.5). These reactions were performed in the open air because all catalysts used are relatively air and moisture stable. In all cases, the iodobenzene showed the greatest reactivity while the Pd(dppf)Cl₂ and Pd(amphos)Cl₂ catalysts gave the greatest yields. Figure 2.5b shows a screen of catalyst loading using triethylamine base. As expected, increasing catalyst loading percentage increases reactivity. Increased catalyst loading percentages increased yield, but it is important to find optimal catalyst loading as this increases cost.

Previous DESI high-throughput screening work using a similar Suzuki coupling^{52, 53} exclusively utilized the XPhosPd G3 catalyst. Other studies have shown the XPhosPd G3 catalyst to work very well, even for difficult substrates.⁵⁷ This work was done at room temperature and the differences in observed reactivity between those studies and this one is most likely due to differences in temperature.

2.3.4 Amine Alkylation and Automated MS/MS Acquisition



Scheme 2.2 Alkylation of various amines (**4-7**) by a halide (**A-C**) to form a single alkylation product. Reaction can potentially form a double alkylation product.

Amine alkylation reactions were also studied using this system. The carbon-nitrogen bond is a key step for the formation of a large number of compounds.⁷⁵ The direct nucleophilic alkylation can be problematic because it forms both single and double alkylation products.⁵³ The reaction of benzylamine (**4**) and benzyl bromide (**A**) (Scheme 2.2) shows a large conversion to the double alkylation product.

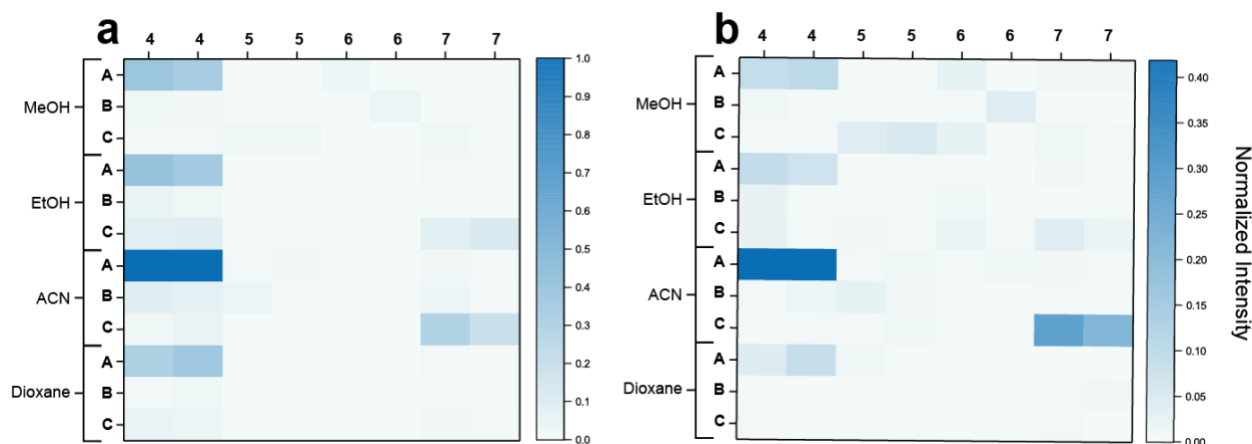


Figure 2.6. Reaction of benzylamine (**4**) and benzyl bromide (**A**) was observed to be fastest in acetonitrile solvent. (a) The single alkylation product (**4** + **A**) was observed as well as (b) the double alkylation product (**4** + **2A**).

Heatmap for the single alkylation product is shown in Figure 2.6a and for the double alkylation product in Figure 2.6b. Some reaction is seen in other solvents, but this reaction proceeds the best in the polar, aprotic solvent acetonitrile. Benzyl bromide showed far greater reactivity than benzyl chloride, given that bromide is a stronger leaving group than chloride. Similarly, no reactivity was observed for bromoethylbenzene (**B**) due to the lack of stability of its carbocation when compared to the benzyl halides. Since the reactions were diluted in methanol prior to analysis, solvent effects on ionization efficiency of the products should be minimal.

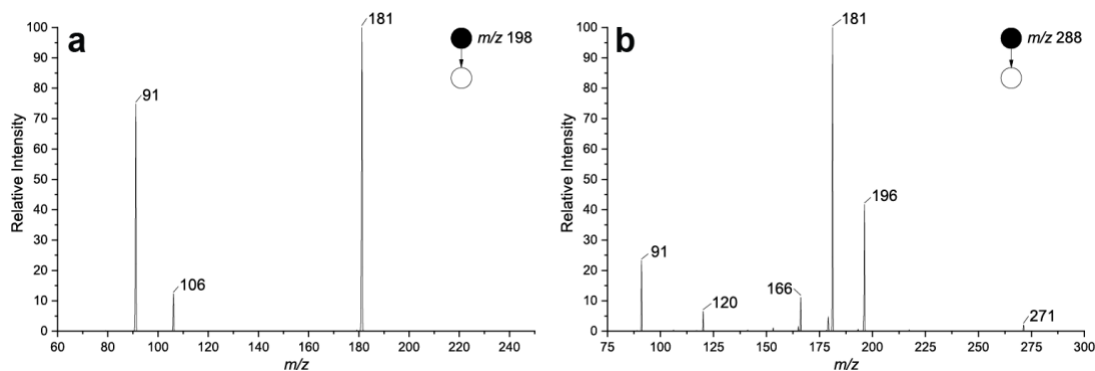
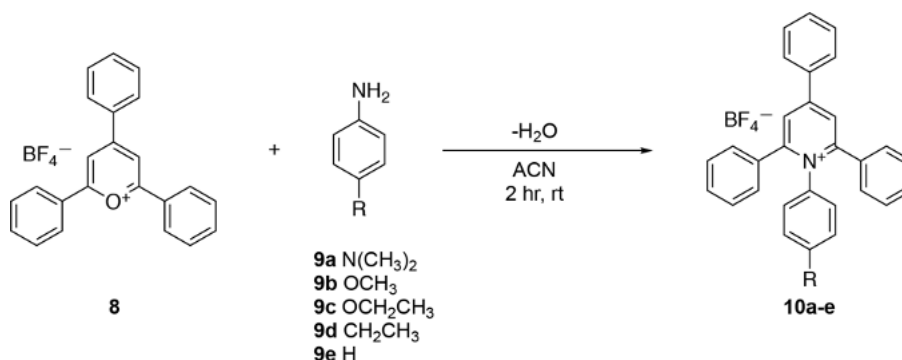


Figure 2.7 MS/MS data was acquired automatically for each well to confirm the identity of the desired product. (a) MS/MS fragmentation of the single alkylation product and (b) MS/MS fragmentation of the double alkylation product is shown for the reaction of benzylamine and benzyl bromide.

Data acquisition in these experiments was controlled through Thermo-Fisher XCalibur software, which allowed for the automated acquisition of MS/MS. This can either be done by pre-selecting expected product ion masses or can be done in a data-dependent fashion. In the case of the amine alkylation, MS/MS data was collected for each of the expected alkylation products, as exemplified in Figure 2.7. The spectra obtained for these compounds confirm the identity of the products as they agree with reported literature spectra.⁵³

2.3.5 Katritzky Transamination



Scheme 2.3 Reaction of 2,4,6-triphenylpyrylium tetrafluoroborate (**8**) with various para-substituted anilines (**9a-e**) to form a pyridinium product (**10a-e**).

The Katritzky transamination reaction involves reaction of a pyrylium heterocycle (**8**) with a para-substituted aniline (**9a-e**) to form the pyridinium salt (Scheme 2.3). The reactions were performed in acetonitrile and run in quadruplicate. The resulting MS ion intensities were used to calculate a ratio of product to starting material without correction for ionization efficiencies.

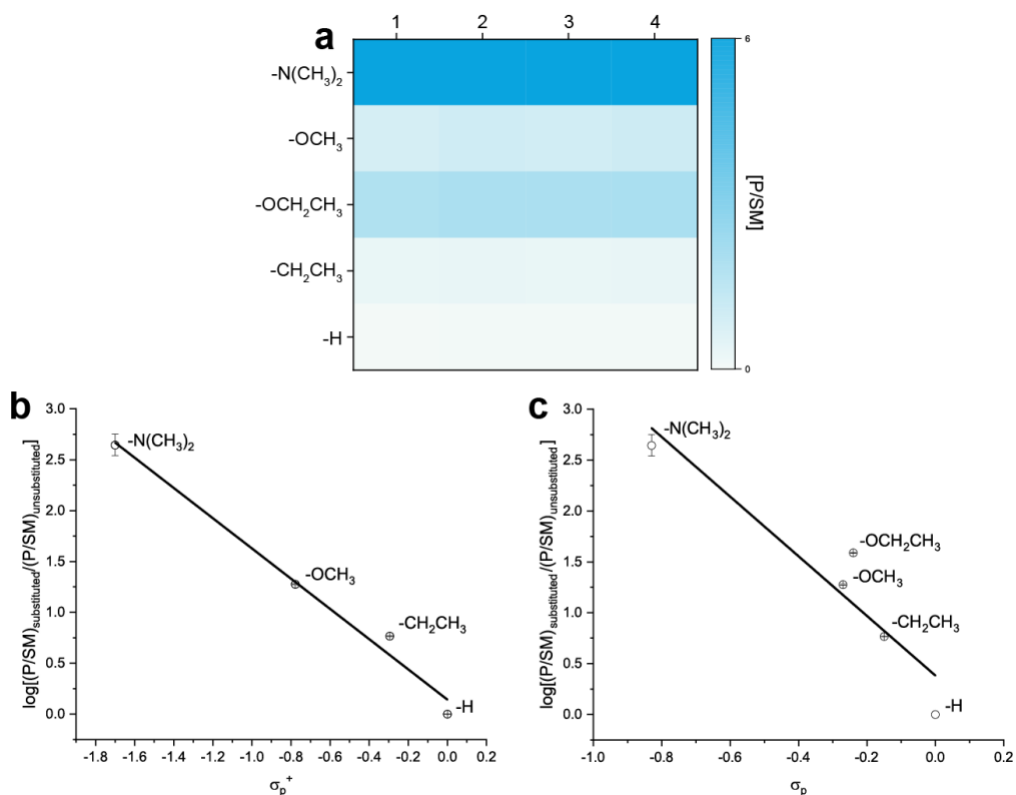


Figure 2.8. (a) Heatmap of product to starting material ratios for each para-substituted aniline for the Katritzky transamination reaction run in acetonitrile. (b) Hammett plot versus σ_p^+ constants and (c) σ_p Hammett plot versus σ_p constants. The electrophilic substituent constant σ_p^+ shows a log-linear relationship, while the classic Hammett constants σ_p show a semi-log-linear relationship.

A heatmap of the resulting ratios is shown in Figure 2.8a. This data can also be displayed as a Hammett plot, showing the log reaction yield of the substituted cases versus the unsubstituted plotted versus the substituent constant σ_p^{76-78} (Figure 2.8c). The slope of the resulting plot shows the effect of the electronic nature of the substituents on the reaction kinetics. When conjugation exists between the substituents and the cationic reaction center, such as with anilines, classic Hammett σ_p values result in poor correlation.⁷⁷ The correlation can be greatly improved using electrophilic substituent constants σ_p^+ (Figure 2.8b).⁷⁹ This correlation is much more strongly linear when compared to standard Hammett substituent constants. The ethoxy substituent does not appear in Figure 2.8a because the Hammett constant for this substituent was not available. This is evidence that the reaction site is in direct resonance with the *para* substituent, which offers greater stabilization.⁸⁰

2.4 Conclusions

Most reaction screening systems are large-scale and expensive which limits availability to the individual investigator. By modifying a 3D printer to replace the extruder with a glass syringe, low-cost hardware and open-source software can be used for preparation of 96-well microtiter plates and subsequent screening of reaction mixtures. This allows for the easy and cheap investigation of reactions in which the reactivity landscape greatly depends on the reaction conditions and seemingly endless combinations of solvent, catalyst, and base are available. Automated MS/MS capabilities aid in identification of product as well as potential byproducts. Automated preparation of well plates can be done in approximately 40 minutes and the MS analysis time is approximately 105 minutes on a system that is home-built and low-cost.

CHAPTER 3. TURNING AND FOCUSING OF IONS AT ATMOSPHERIC PRESSURE

Portions of this work have been published in the journal *International Journal of Mass Spectrometry* as the article: “Schrader, R. L.; Marsh, B. M.; Cooks, R. G., Temporal Distribution of Ions in Ambient Pressure Drift Tubes with Turns, *Int. J. Mass Spectrom.* **2020**, 456, 11639”

3.1 Introduction

The resolution of a drift tube ion mobility instrument is directly proportional to the square root of the drift length. Consequently, many instruments feature drift lengths of on the order of meters.⁴¹ On the other hand, several ion mobility instruments including ion cyclotron mobility spectrometry,⁸¹ structures for lossless ion manipulation (SLIM),⁸² and cyclic IMS⁴⁰ feature curved trajectories to allow for theoretically unlimited ion path lengths. Some^{40, 82} make use of traveling waves for ion mobility separation. By turning the ion beam, long path lengths can be achieved without a commensurately long drift path. Each of these techniques has been implemented at reduced pressure with use of an RF electric field (or RF element between drift tubes) for axial ion confinement. “S-bend” shaped drift tubes have been used to couple coaxial laser beams to ion mobility separators.⁸³ The turning of ions is also important in quadrupole devices, for example to separate the ion path from the path of neutrals prior to detection,⁸⁴⁻⁸⁶ quadrupole deflectors can be used to turn ions from multiple sources.⁸⁷ Though the efficient turning of ion beams at reduced pressures using RF is well understood, it necessitates the use of vacuum pumps, adding to power and weight burdens.

3D printed electrodes operated with high voltage DC potentials have been used to turn ion beams at atmospheric pressure.^{88, 89} These earlier studies examined the spatial distribution of the ion beams, but the temporal distribution was not investigated. A marked racetrack effect is expected because ions on the inside of a turn have a shorter path to travel than ions on the outside. Ions may experience electric field inhomogeneities depending on their starting position. The effect on resolution of racetrack effects in the ion cyclotron mobility spectrometry, SLIM, and cyclic IMS were shown to be minimal.^{40, 81, 90, 91} Radial confinement of the ion beam likely limits the differences in ion path and electric field inhomogeneity that the ions experience.

As ions enter the initial vacuum region of the mass spectrometer, they undergo a supersonic expansion.⁹² RF-based ion focusing devices are used to focus the ions for efficient transfer to subsequent pressure regions.^{93, 94} These devices have greatly improved instrument sensitivity when compared to previous ion optics. These devices operate in low to medium vacuum conditions, ranging from mTorr to 10 Torr. The focusing of the ion beam at atmospheric pressure, prior to inlet capillary, could be used to help improve instrument performance. The focusing performance of RF-based ion funnels at atmospheric pressure is greatly reduced compared to operation in the millitorr regime.⁹⁵ Focusing of ions at atmospheric pressure with DC voltages can be accomplished with electrodes of conical shapes^{89, 96} as well as drift tube devices with non-uniform electric fields.^{97, 98} Non-uniformities in the electric field of a DC ion funnel are able to focus ions with sufficient electric field strength at reduced pressure.⁹⁹

3.2 Experimental

3.2.1 3D Printing

All housings and electrodes were designed in Autodesk Inventor (San Rafael, CA) and converted to '.stl' files. To prepare for 3D printing, stereolithography files were sliced with Simplify3D (Cincinnati, OH) to break the model into printable layers and generate commands for the 3D printer as '.gcode' files. Housings were printed from ColorFabb (Belfeld, Netherlands) polylactic acid/polyhydroxyalkanoate filament. Electrodes were printed from Proto-pasta (Vancouver, WA) conductive polylactic acid filament. All housings and electrodes were printed with a Mendelmax 3 (Maker's Tool Works, Oklahoma City, OK) 3D printer. Straight drift electrodes had dimensions 38 x 28 x 1.5 mm (o.d., i.d., thickness). Turning electrodes were generated as solids of revolution of 10°, 45° and 90° using the same dimensions as the straight drift electrodes. For ion funnel electrodes, the inner diameter was varied from 28 mm to 7 mm for the final electrode. The intermediate electrodes had linearly decreasing inner diameters.

3.2.2 SIMION Simulations

Ion trajectory simulations for each drift tube were performed using SIMION 8.1 (Scientific Instrument Services, Ringoes, NJ). CAD files (*.stl) of each electrode structure were imported into SIMION using the SL toolkit. To perform atmospheric pressure simulations, the statistical

diffusion simulation (SDS) model was used to model collisions with background gas.¹⁰⁰ Reduced mobility values from the literature¹⁰¹ were used explicitly in the SDS algorithm. For turning and ion funnel mesh simulations, ions were initially distributed randomly within a circle distribution orthogonal to the drift axis bounded by a diameter of 6 mm (turning) or 2 mm (funnel). For the turning simulations, the ions were located between the first and second drift electrode. For ion funnel mesh simulations, the ions were located at the tip of the nESI emitter. For ion funnel electric field simulations, ions were distributed within a circle distribution bounded by a diameter of 27 mm centered in the focusing electrode. Ion arrival at a grounded plate electrode after the final drift electrode modeled the Faraday cup detector.

3.2.3 Electronics

Turning Devices

A custom voltage divider circuit of 1 M Ω resistors (Stackpole Electronics, Inc., Raleigh, NC, $\pm 1\%$) was built on a solderable breadboard (Mouser Electronics, Mansfield, TX) and connections were made by inserting header pins into holes in the electrodes. For the turning, hairpin, and chicane electrodes, the breadboard was cut into multiple pieces, one for each electrode section, with a high voltage wire electrically connecting the sections. The first electrode (the focusing electrode) had a 25 mm cylindrical extension to confine the electrospray plume. This has been described in detail previously.¹⁰² In each drift tube, the focusing electrode was 3000 V, the injection electrode was 2500/2375V, and the drift voltage was 2400 V.

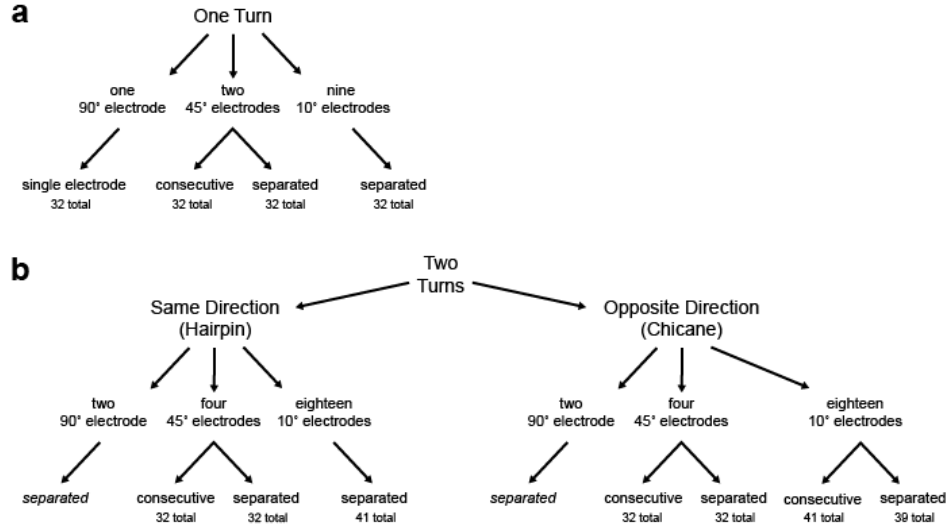


Figure 3.1 Flow chart of designs for (a) single turn drift tubes and (b) two turn drift tubes. The total number of electrodes is given for each design. The straight drift tube with the same path length as single turn drift tubes had 45 total electrodes. The straight drift tube with the same path length as the two turn drift tubes had 59 electrodes. The two separated 90° electrode chicane and hairpin systems showed no ion transmission in simulations and were not fabricated.

The total number of electrodes for each geometry is given in Figure 3.1. There is a voltage drop on each drift electrode, regardless of electrode type. An entrance ion gate was created with two steel mesh screens (40 mesh, 66% transmission, E-Fab, Santa Clara, CA) on the 1st and 2nd drift electrode. A third mesh was used at the exit of the drift tube to shield the Faraday cup detector. High voltage DC potentials ($\pm 0.2\%$) were applied from a custom power supply. Switching was performed using a Behlke GHTS 60A (Billerica, MA) high voltage switch with input waveforms from a precision square waveform generator operating at a frequency in the range of 2 – 10 Hz (Model DG535, Stanford Research Systems, Stanford, CA), the chosen value depending on ion arrival times of interest. An injection time of 1 ms was used for all experiments. Detection was performed using a custom PCB Faraday cup with an SMB (Sub-Miniature B) connection to a Keithley 428 current amplifier (Solon, OH). Data for straight drift tubes was collected with an amplification of 10^8 V/A and data for turning drift tubes was collected with an amplification of 10^9 V/A. Data was collected using a Tektronix TDS 2024C 4-channel digital oscilloscope (Beaverton, OR).

Ion Funnel Devices

Voltage dividers were constructed from the same solderable breadboard as the turning devices. Resistors of values 100 k Ω , 200 k Ω , 300 k Ω , 390 k Ω , 510 k Ω , 620 k Ω , 750 k Ω , 820 k Ω , 910 k Ω , 1 M Ω , 2 M Ω , and 3 M Ω were used in various configurations to generate the desired electric field. No switched potentials or ion meshes were used with the ion funnel device. The first electrode was set to 3000 V regardless of the number of electrodes.

3.2.4 Affixing the Mesh to the Electrode

In order to construct an ion gate, mesh material is affixed to the plastic electrode using polyimide tape. For numerous experiments in this dissertation, this was a stainless-steel mesh screen (40-mesh) with 66% optical transmission manufactured by E-fab. The optical transmission is compromised by the alignment of the two meshes. Ion transmission is greatly improved when the alignment of the two meshes is optimized.

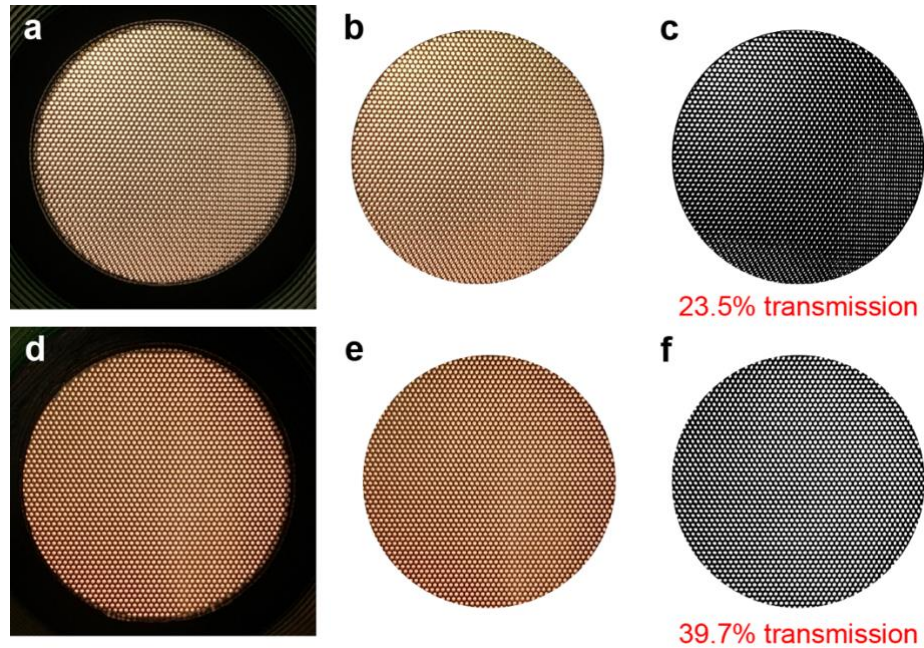


Figure 3.2 An image (a and d) of two meshes taken and (b and e) cropped to only contain the mesh and then (c and f) converted to black and white pixels using Adobe Photoshop. The number of white versus total number of pixels was counted using MATLAB to give a percent transmission. The difficulty in aligning the two meshes is seen from the variability in optical transmission for two different meshes.

In order to quantitatively assess the alignment of the meshes, backlit images were taken of the ion gate. These images were cropped using Adobe Photoshop (San Jose, CA) and then converted to be two color: black and white. The color threshold was adjusted until the black and white image appropriately matched the color image. The optical transmission was then calculated using MATLAB by dividing the number of white pixels by the total number of pixels. Two examples are shown in Figure 3.2. For a poorly aligned mesh, the optical transmission is reduced from the optimal value of 66% to 23.5%. Better alignment was achieved, but this only gave an optical transmission of 39.7%. Poor mesh alignment becomes an even greater issue for experiments described later with two ion gates.

In order to improve sensitivity, a new mesh material was selected. A 90% transmission electroformed nickel mesh screens (MN17, Precision Eforming, Cortland, NY) was selected for its high optical transmission. This material is so thin ($4 - 5 \mu\text{m}$) and pliable that the method for affixing them to the electrodes became non-trivial.

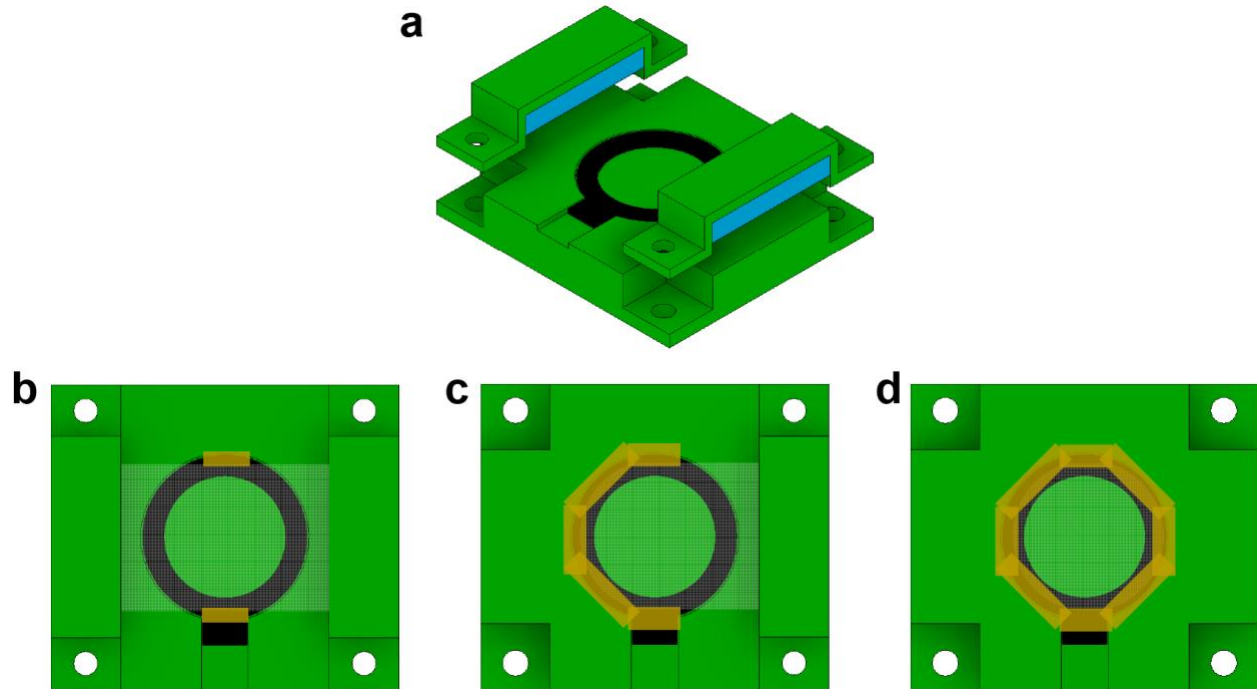


Figure 3.3 (a) Orthographic projection of mesh application device. (b) A strip of mesh material was clamped by the two pieces of foam (blue) and polyimide tape is applied to the top and bottom edges of the mesh material. (c) One clamp was removed, the mesh was cut to the shape of the electrode, and that side was taped to the electrode with polyimide tape. (d) The second clamp was removed, and the final side is fixed to the electrode with polyimide tape. The overhanging tape is then trimmed with a razor blade.

The mesh material must be taut so that the two adjoining meshes do not touch each other. In order to do this, a holder was 3D printed and a method developed (described in Figure 3.3) to affix the meshes to the electrode. Essentially, the device is used to hold the mesh taut over the electrode so that it can be taped down while the mesh remains flat. The new mesh was able to achieve a nearly two times improvement in signal intensity for the TAA cations.

3.2.5 Chemicals

Tetraethylammonium bromide, tetrabutylammonium bromide, tetrahexylammonium bromide, and tetraethylammonium bromide were purchased from Sigma Aldrich (St. Louis, MO). Each tetraalkylammonium (TAA) salt was prepared at 100 μ M concentration in acetonitrile (Fisher Scientific, Hampton, NH).

3.2.6 Ionization

Borosilicate glass capillaries (i.d. 0.86 cm, o.d. 1.5 cm, 10 cm length) were purchased from Sutter Instruments (Navajo, CA). The capillaries were pulled to an approximate tip diameter of 5 μ m using a P-97 Flaming/Brown tip puller (Sutter Instruments). Pulled capillaries were fitted to a Warner Instruments (Hamden, CT) E series electrode with a 0.127 mm diameter silver wire (Alfa Aesar, Ward Hill, MA). Capillaries were placed approximately 1 – 2 mm from the entrance mesh. High voltage (5.5 kV) was applied to the electrode holder.

3.3 Results and Discussion

3.3.1 Drift Tubes with One Turn

Four different 90° drift tubes were fabricated, each with a different configuration of electrodes. “Consecutive” geometries refer to turning electrodes placed successively without interruption, and “separated” geometries refers to geometries where turning electrodes are separated by one or more straight drift electrodes. The four 90° drift tubes were: two consecutive 45° electrodes, two separated 45° electrodes, nine separated 10° electrodes, and one 90° electrode. A straight drift tube of the same path length (measured along the center line) was fabricated for comparison. Computer-generated renderings of each drift tube are given in Figure 3.4(a-d). Histograms of ion drift times calculated from SIMION trajectory simulations for each drift tube

are shown in Figure 3.4(e-h). Experimental data for each drift tube is shown in Figure 3.4(i-l). Good agreement was seen between the simulated arrival time distributions and the experimental ion mobility spectra. Reduced mobilities (K_0) were used explicitly in the SDS algorithm because estimated values can be incorrect by as much as 40 percent.¹⁰³ The single 90° electrode performed poorly in both simulations and experiment and is not shown.

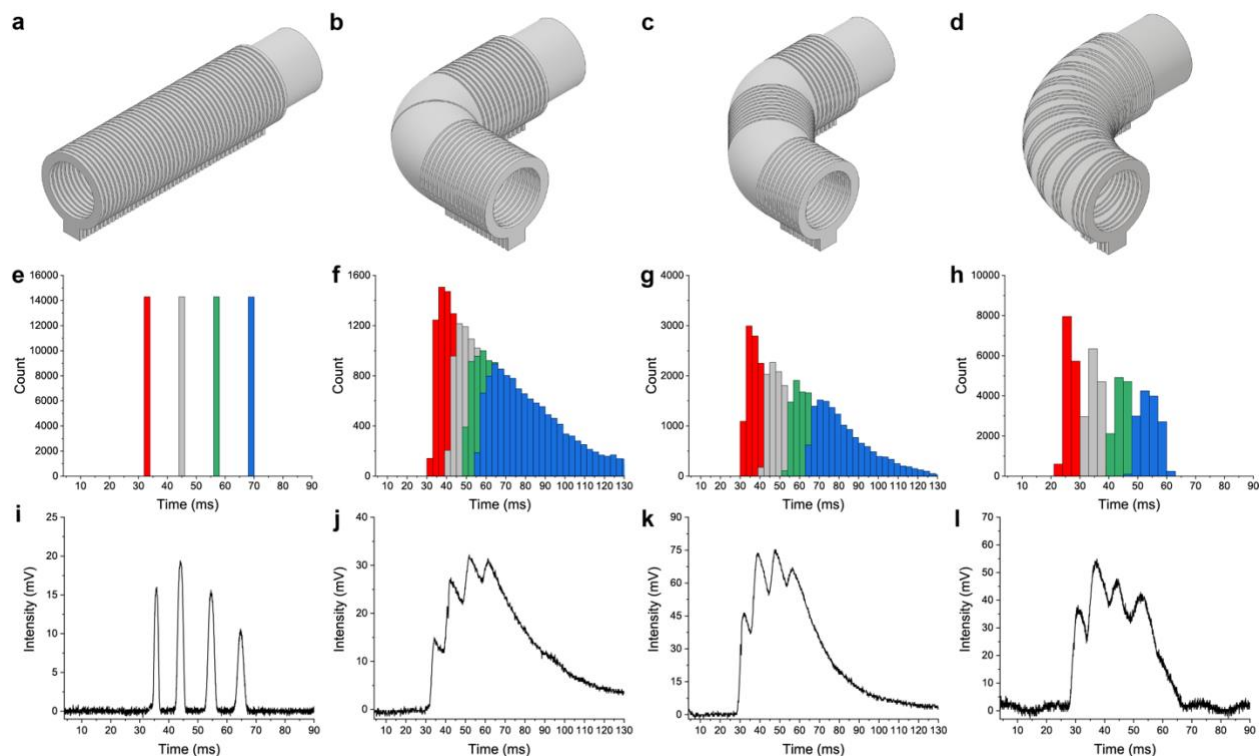


Figure 3.4 Renderings of (a) straight drift tube with same path length as single turn drift tubes, turns with (b) two consecutive 45° electrodes, (c) two separated 45° electrodes, and (d) nine separated 10° electrodes. Histogram of drift times from SIMION trajectory simulations for (e) straight drift tube, turns with (f) two consecutive 45° electrodes, (g) two separated 45° electrodes, and (h) nine separated 10° electrodes. Experimental results with C₂, C₄, C₆, and C₈ tetraalkylammonium salts for (i) straight drift tube, turns with (j) two consecutive 45° electrodes, (k) separated 45° electrodes, and (l) nine separated 10° electrodes.

The loss in resolving power as a result of the turn can be attributed to two factors: (1) differences in path length of ions on the inside of the turn versus ion on the outside of the turn and (2) differences in electric field strength on the inside vs the outside of the turn. The magnitude of loss in resolving power is much greater in the drift tubes with 45° electrodes than for the drift tube

with 10° electrodes. The electric field gradient in the plane normal to ion motion is greater in the turn for 45° electrode structures than for the 10° electrode structures (Figure 3.5).

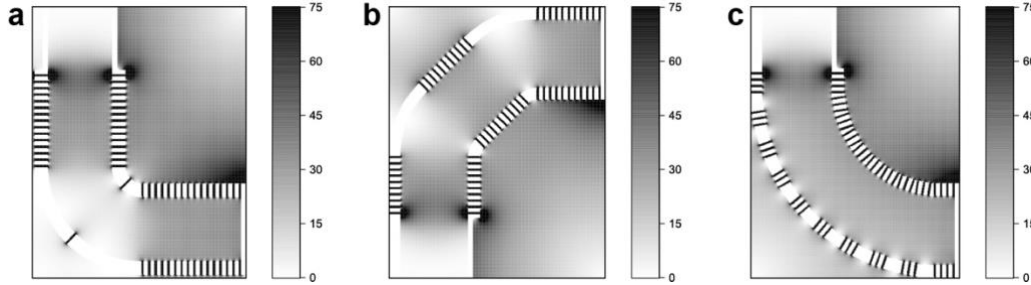


Figure 3.5 Electric field strength (V/mm) calculated from SIMION of a single turn using (a) two consecutive 45° turning electrodes, (b) two separated 45° turning electrodes, and (c) nine separated 10° turning electrodes.

This leads to a large dispersion in the ion arrival time due to variation in drift field strength based on the ion's position. The drift field is far more homogenous for the 10° electrodes; hence the smaller resolution reduction for these for these electrodes even after considering the greater number of electrodes.

3.3.2 Drift Tube with Two Turns

Two potential geometries exist for drift tubes with two turns: two turns in the same direction (a hairpin) and two turns in the opposite direction (a chicane). For the hairpin, three different drift tube geometries were fabricated: two turns with two consecutive 45° electrodes, four turns with separated 45° electrodes, and 18 separated 10° electrodes. A straight drift tube with the same path length (measured along the center line) as the hairpin drift tubes was fabricated for comparison. SIMION simulations showed that ions do not pass through a hairpin with two 90° turns, so this device was not fabricated.

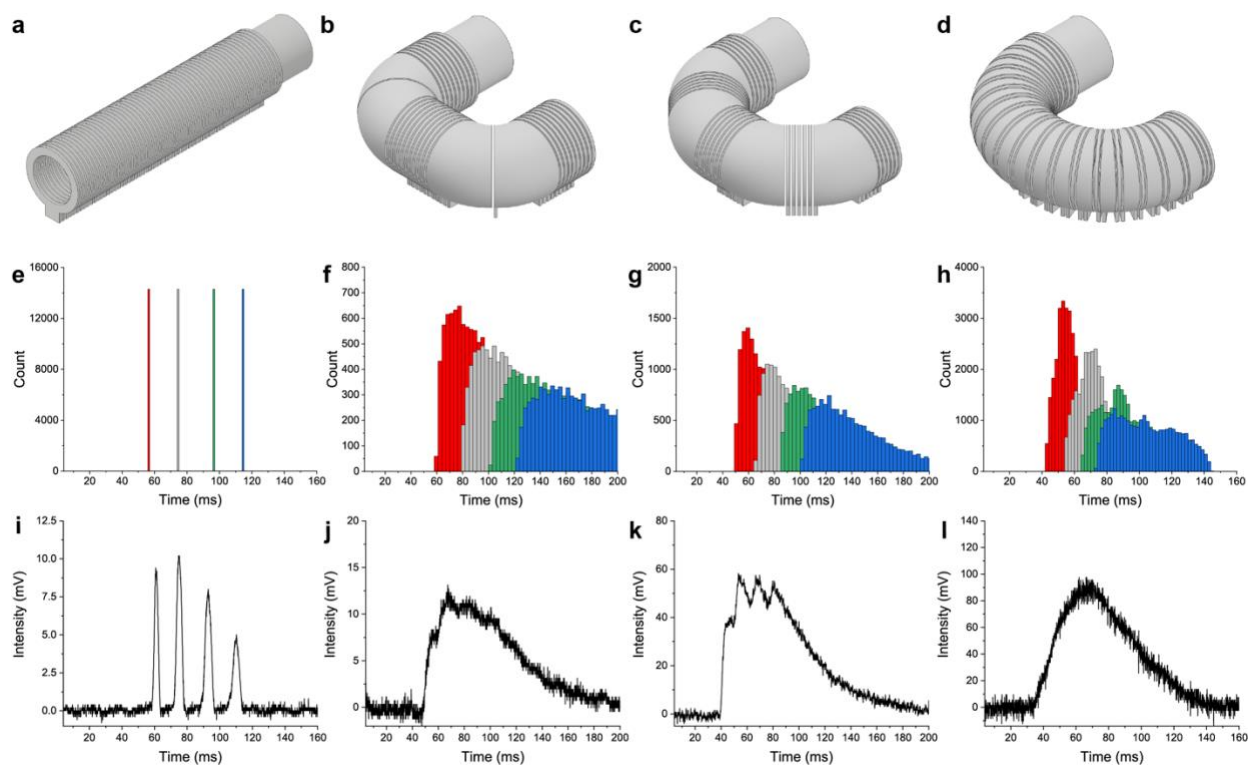


Figure 3.6 Renderings of (a) straight drift tube with same path length as hairpin drift tubes, hairpin with (b) two turns with two consecutive 45° electrodes, (c) four turns with separated 45° electrodes, and (d) 18 separated 10° electrodes. Histogram of SIMION trajectory simulations for (e) straight drift tube, hairpin with (f) two turns with two consecutive 45° electrodes (g) four turns with separated 45° electrodes, and (h) 18 separated 10° electrodes. Experimental results with C₂, C₄, C₆, and C₈ tetraalkylammonium salts of (i) straight drift tube, hairpin with (j) two turns with two consecutive 45° electrodes, (k) four turns with separated 45° electrodes, and (l) 18 separated 10° electrodes.

Computer-generated renderings of each drift tube are shown in Figure 3.6(a-d). Histograms of ion drift times calculated from SIMION trajectory simulations for each drift tube are shown in Figure 3.6(e-h) and experimental data is shown in Figure 3.6(i-l). As with single turning drift tubes, SIMION simulations show good agreement with the experimental data. Resolution is further degraded in the two turn geometries when compared to the drift tubes with one turn as differences in path length and electric field strength are exaggerated.

For chicane drift tubes, four different drift tube geometries were fabricated: two turns with two consecutive 45° electrodes, four turns with separated 45° electrodes, 18 separated 10° electrodes, and two turns with 18 consecutive 10° electrodes. As with the hairpin, SIMION

simulations showed that ions do not pass through a chicane with two 90° electrodes, so this device was not fabricated.

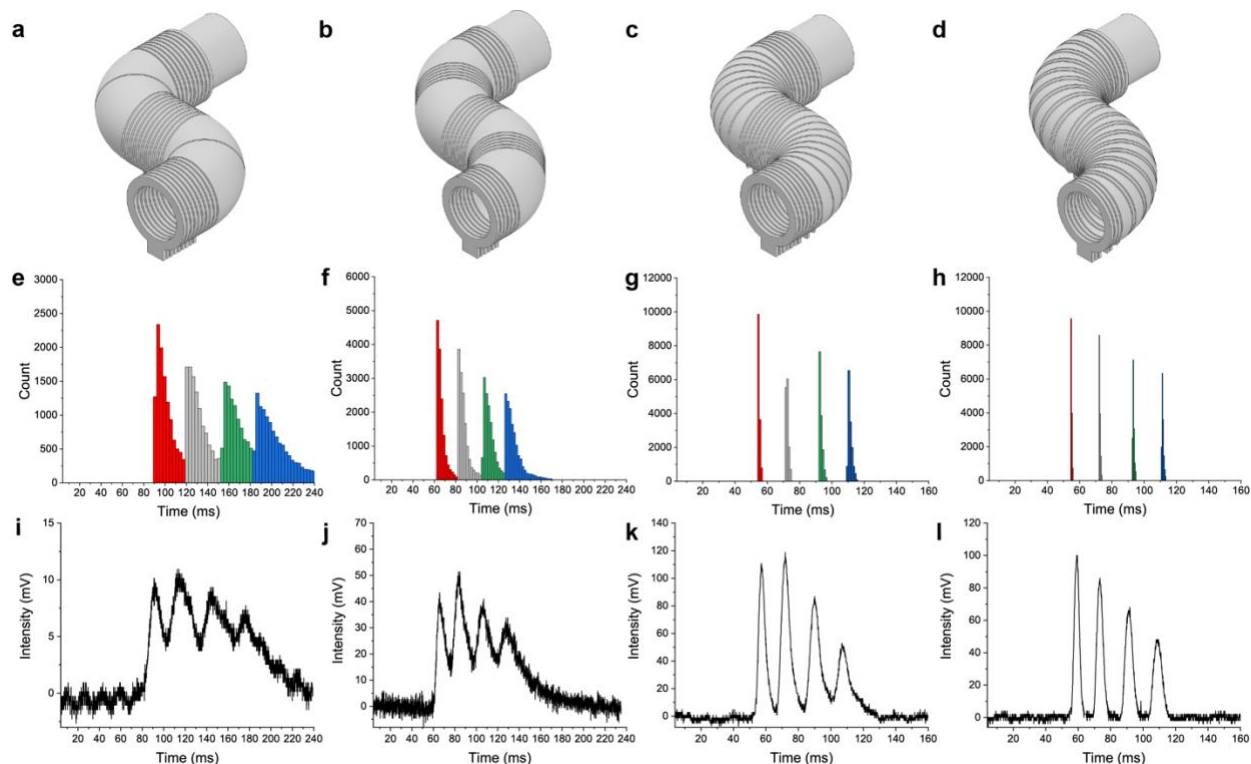


Figure 3.7 Renderings of chicane drift tube with (a) two turns with two consecutive 45° electrodes, (b) four turns with separated 45° electrodes, (c) two turns with 18 consecutive 10° electrodes, and (d) 18 separated 10° electrodes. Histogram of drift times from SIMION trajectory simulations for chicane with (e) two turns with two consecutive 45° electrodes, (f) four turns with separated 45° electrodes, (g) two turns with 18 consecutive 10° electrodes, and (h) 18 separated 10° electrodes. Experimental results with C_2 , C_4 , C_6 , and C_8 tetraalkylammonium salts for chicane with (i) two turns with two consecutive 45° electrodes, (j) four turns with separated 45° electrodes, (k) two turns with 18 consecutive 10° electrodes, and (l) 18 separated 10° electrodes.

Computer-generated renderings of each drift tube are shown in Figure 3.7(a-d). Histograms of ion drift times calculated from SIMION trajectory simulations for each drift tube are shown in Figure 3.7(e-h) and experimental data is shown in Figure 3.7(i-l). and chicane drift tubes have the same path length, so both can be compared with the same length straight drift tube.

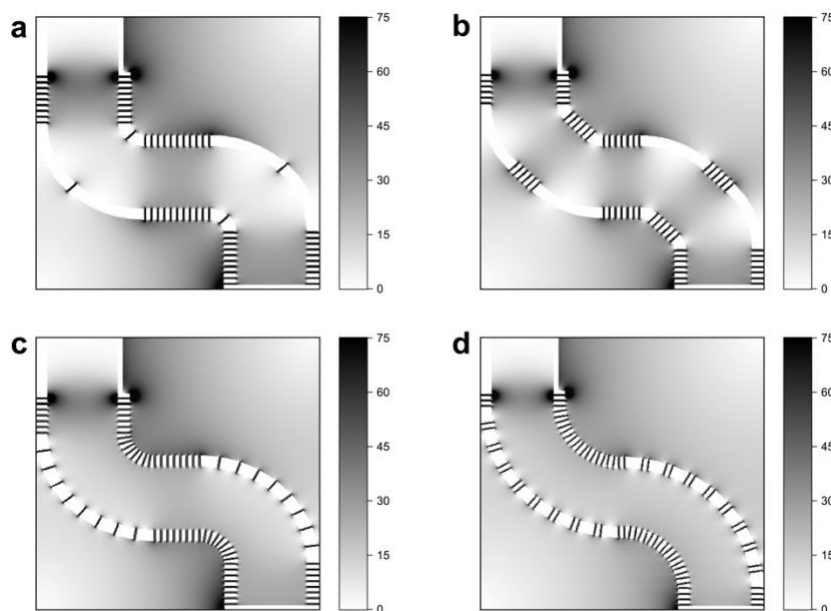


Figure 3.8 Electric field strength (V/mm) calculated from SIMION of the chicane with (a) two turns with two consecutive 45° electrodes, (b) four turns with separated 45° electrodes, (c) two turns with nine consecutive 10° electrodes, and (d) 18 separated 10° electrodes.

Unlike the turn and hairpin drift tubes, because there are two turns in the chicane drift tube an ion originating off-center on either side of the drift tube will travel the same path length. The resulting correction led to lower temporal dispersions for the chicane drift tubes. For both drift tubes containing 45° electrodes, resolving powers were still very low which is attributed to the differences in electric field strength caused by the 45° electrodes, Figure 3.8(a-b).

Table 3.1 Comparison of drift time and resolving power for straight drift tube versus chicane with 18 separated electrodes. (C_m refers to the tetraalkylammonium cation with m-carbon alkanes).

	Straight		Chicane	
	Drift Time (ms)	Resolving Power	Drift Time (ms)	Resolving Power
C₂	60.7	24.3	59.1	16.5
C₄	75.2	20.9	73.4	17.1
C₆	92.9	22.1	91.2	17.3
C₈	110.4	26.2	108.5	16.0

Unlike the previously discussed geometries, the performance degradation in chicane drift tubes with 10° electrodes was greatly reduced compared the straight drift tubes. The average resolving power was reduced by 1.4 times (Table 3.1) for the chicane with 18 separated 10°

electrodes. Performance was reduced when the turning electrodes were arranged consecutively. This is attributed to the electric field strength differences between the two geometries, Figure 3.7(c-d). A general observation is that the difference in electric field strength in the turns was greater when all of the turning electrodes were placed consecutively versus placing a drift electrode between each turning electrode. The result was that the resolving power was lower when all the turning electrodes were placed consecutively versus placing a drift electrode between each turning electrode.

3.3.3 Non-uniform Electric Fields for Ion Focusing at Ambient Pressure

Drift tube ion mobility spectrometers are normally operated such that voltage difference between each adjacent electrode is constant. This results in a constant electric field strength throughout the entire drift length. The trajectory of ions at atmospheric pressure follow a path normal to the equipotential lines.¹⁰⁴ Electric fields for a 12 electrode ion funnel geometry were calculated using SIMION. The inner diameter of the electrodes ranged linearly from 28 mm at the entrance to 7 mm at the exit and the first electrode had a 25 mm cylindrical extension to confine the electrospray plume.

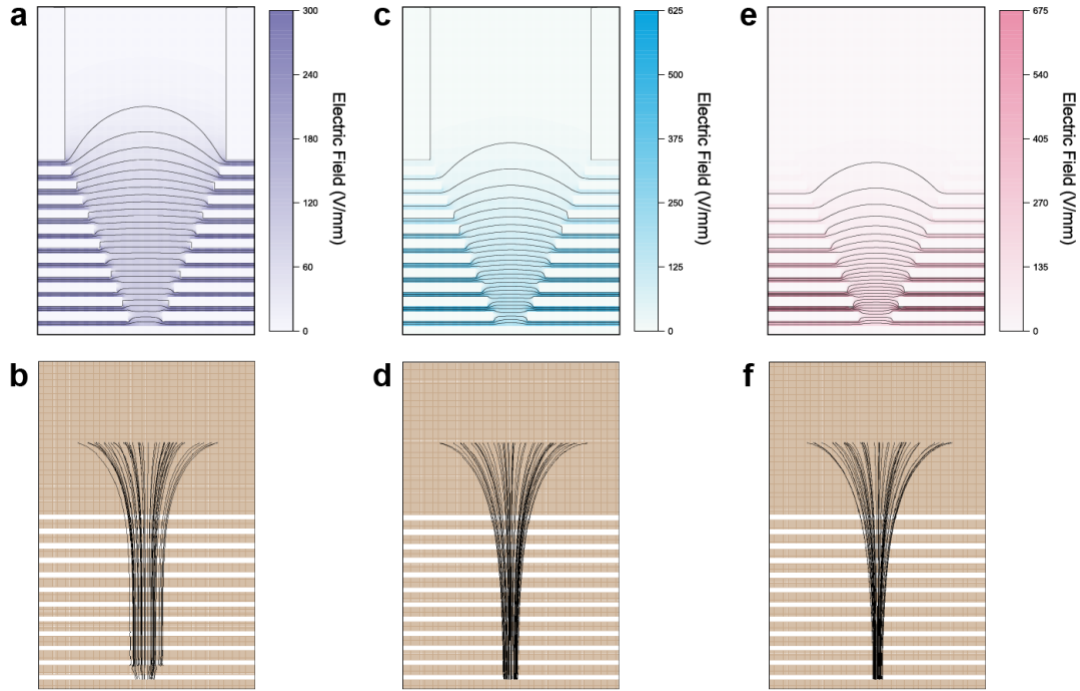


Figure 3.9 (a) Color map showing electric field calculated for equal resistances from SIMION with equipotential lines overlaid. Straight equipotential lines mean that ions are not focused to the center to be transmitted. (b) Ion trajectories from SIMION for ion funnel geometry with equal resistances (linear voltage drop) between each electrode. (c) Color map showing electric field for linear resistance increase between electrodes calculated from SIMION with equipotential lines overlaid. Curved equipotential lines mean the ions are focused to the center of the drift tube and are transmitted. (d) Ion trajectories from SIMION for ion funnel geometry with linear resistance increase between electrodes (non-linear voltage drop) between each electrode. (e) Color map showing electric field for square resistance increase between electrode calculated from SIMION with equipotential lines overlaid. (f) Ion trajectories from SIMION for ion funnel geometry with square resistance increase between electrode (non-linear voltage drop) between each electrode.

For a uniform electric field, the equipotential lines essentially straight across the electrode diameter (Figure 3.9a) The ions move perpendicularly to these equipotential lines, are not focused to the center, and impact the electrodes as these decrease in diameter. In order to focus ions to the center, the equipotential lines must be convex. These equipotential lines are result from an electric field that is non-uniform, i.e. voltage drop between electrodes was increased down the length of the drift region. To do this, the value of the resistors between each electrode increased between each electrode. For Figure 3.9a and b, the resistance increased linearly from 100 k Ω to 1100 k Ω by approximately 100 Ω .

Table 3.2 Linearly increasing resistances generated a non-uniform (linear) electric field in to generate a focusing electric field.

Electrode	Resistance (k Ω)	Voltage (V)
1		3000
2	100	2958
3	200	2873
4	300	2746
5	390	2581
6	510	2365
7	620	2103
8	750	1786
9	820	1439
10	910	1054
11	1000	630
12	1100	165
Ground	390	0

The exact values and voltages are given in Table 3.2. The resistance between the final electrode and ground was only 390 k Ω so that the final voltage would be similar to the uniform electric field. Unlike the uniform electric field, the equipotential lines in the linearly increasing electric field are such that the ions are focused to the center as seen from the ion trajectories in Figure 3.9d.

Table 3.3 Quadratically increasing resistances generated a non-uniform (quadratic) electric field in order to generate a stronger focusing field.

Electrode	Resistance (k Ω)	Voltage (V)
1		3000
2	100	2892
3	200	2947
4	390	2879
5	620	2770
6	910	2610
7	1200	2399
8	1620	2114
9	2000	1762
10	2510	1321
11	3000	793
12	3600	160
Ground	910	0

To further improve focusing, a second non-uniform field was tested. In this case, the electric field increased quadratically between electrodes. The exact values and voltages are given in Table 3.3. The ion trajectories (Figure 3.9f) show a smaller final ion beam than linearly increasing resistances (Figure 3.9d).

Table 3.4 Ion current measurements for 12 and 16 electrode geometry collected for each voltage configuration using nESI of 100 μ M each solution of C₂ – C₈ TAAs.

		Current (nA)	Current Density (pA/mm ²)
12 electrodes	28 mm electrodes	95.51 \pm 11.76	38.78 \pm 4.77
	Funnel (constant)	3.05 \pm 0.08	27.01 \pm 0.74
	Funnel (linear)	3.34 \pm 0.06	29.52 \pm 0.50
	Funnel (quadratic)	4.57 \pm 0.39	40.42 \pm 3.47
	Funnel (square w/ mesh)	5.77 \pm 0.42	51.04 \pm 3.76
16 electrodes	28 mm electrodes	53.27 \pm 7.30	21.62 \pm 2.96
	Funnel (square)	1.94 \pm 0.31	12.60 \pm 1.99
	Funnel (square w/ mesh)	0.70 \pm 0.04	4.56 \pm 0.26

The simulations predict that there should be trend in focusing such that observed ion current should be “constant” < “linear” < “quadratic”. In order to experimentally test these devices, a solution of 100 μ M each of C₂ – C₈ TAA cations was nanoelectrosprayed into the device. The resulting ion current was detected using a Faraday cup and current amplifier. Observed ion currents are given in Table 3.4. Just as the simulations predicted, the current increases for the “linear” and “square” electric fields. Compared to the uniform electric field, the “quadratic” electric field improves ion current by almost 1.5 times.

In order to benchmark the focusing performance, the ion current from a 12 electrode drift cell of 28 mm electrode was measured and is given in Table 3.4. The total ion current is nearly 20 times higher with no focusing than the ion funnel devices. Although the total ion current is much higher, the current density is nearly the same between the 28 mm electrodes and the “quadratic” electric field.

The simulations presented in Figure 3.9 do not take into account the contribution of the nESI emitter to the electric field. The nESI emitter was included in a simulation of the “quadratic” electric field and this defocuses the ions at the beginning of the drift tube which likely contributes

to the poor transmission through the funnel devices. Ions that are defocused at the beginning of the drift tube travel to the defocusing field near the electrode edges and are lost. Efficient focusing at the beginning will ensure that ions stay toward the center and improve transmission. In order to limit the contribution of the electric field generated by the nESI emitter, a nickel mesh was added to second electrode. The purpose of this mesh is to limit the contribution of the nESI emitter to the drift region. Experimentally, this leads to a 1.25 times improvement in the ion current (Table 3.4). Any observed improvement must also overcome the loss in transmission due any ions that may impact the mesh. Importantly, the current density with the mesh included is larger than the current density for the 28 mm electrodes.

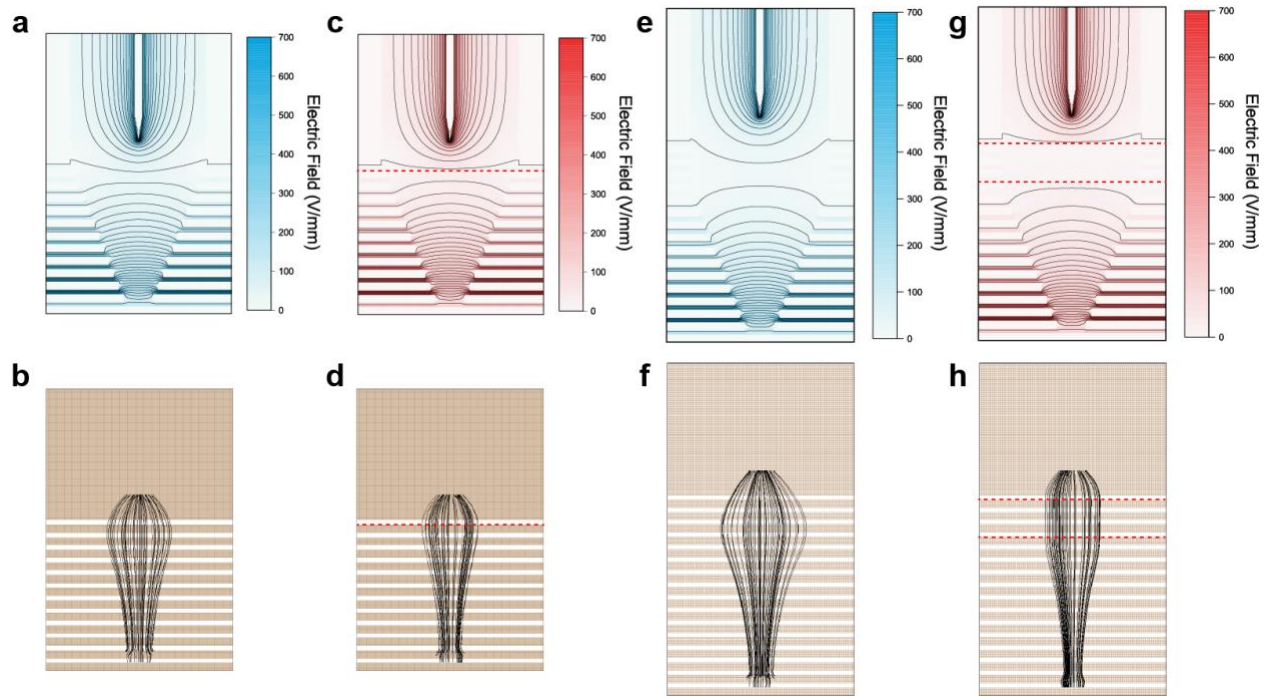


Figure 3.10 (a) Electric field and equipotential lines and (b) ion trajectory simulation for ion funnel geometry with square resistance increase (non-linear voltage drop) between each electrode. (c) Electric field and equipotential lines and (d) ion trajectory simulation for ion funnel geometry with square resistance increase (non-linear voltage drop) between each electrode with added mesh denoted by the red dotted line. (e) Electric field and equipotential lines and (f) ion trajectory simulation for ion funnel geometry with an initial region of linear voltage drop and square resistance increase (non-linear voltage drop) between each electrode. (g) Electric field and equipotential lines and (h) ion trajectory simulation for ion funnel geometry with an initial region of linear voltage drop and square resistance increase (non-linear voltage drop) between each electrode and added mesh denoted by red dotted line.

The electrode diameter for the previously described geometry begins decreasing at the beginning of the drift tube. As described previously, the electric field contribution from the nESI emitter causes defocusing fields. To attempt to improve transmission, four 28 mm electrodes were added prior to the funnel electrodes. The goal of these electrodes was to use electrodes of larger diameter where there are defocusing fields to allow these ions space to defocus and then be refocused by the funnel.

Table 3.5 Following a region of uniform electric field and electrode diameter, quadratically increasing resistance were used to generate a non-uniform electric field.

Electrode	Resistance (k Ω)	Voltage (V)
1		3000
2	100	2983
3	100	2966
4	100	2948
5	100	2931
6	100	2914
7	200	2880
8	390	2813
9	620	2706
10	910	2550
11	1200	2344
12	1620	2065
13	2000	1722
14	2510	1290
15	3000	775
16	3600	157
Ground	910	0

The electric field was constant for the four electrodes that had a 28 mm diameter. Following this region, the resistance was increased quadratically similar to the 12 electrode geometry. Meshes were added at the beginning and end of the constant region (Figure 3.10). The experimentally determined ion currents are given in Table 3.4. Unlike the 12 electrode geometry, the inclusion of meshes is detrimental to the ion current. Additionally, the transmission is not improved by the addition of large diameter electrodes at the beginning of the drift tube.

The inter-electrode spacing (0.95 mm) was chosen based on the solderable breadboard pitch and 3D printer limitations. A potential avenue for improvement of ion transmission is to reduce this spacing.

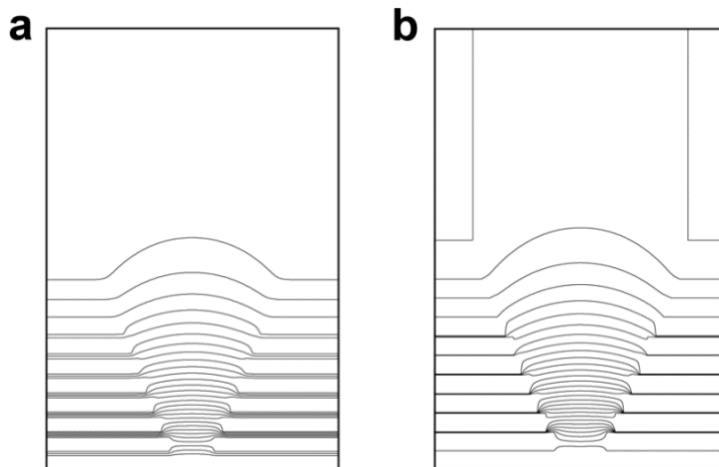


Figure 3.11 (a) Electric field lines for the previously described ion funnel geometry with square resistance increase between electrodes compared with (b) electric field lines for proposed geometry with thicker electrodes and reduced inter-electrode spacing. The defocusing fields appear improved and will potentially offer improved ion transmission.

By reducing the inter-electrode spacing to 0.15 mm (the thickness of a one-layer thick 3D print), the defocusing fields near the edges of the electrodes appear improved compared the previous geometry. Improved ion transmission would open avenues for the use of this device to improve ion transmission to a mass spectrometer.

3.3.4 Conclusions

The manipulation of ions at atmospheric pressure is far more poorly understood than ions at reduced pressure with RF fields. Fundamental studies of the turning and focusing of ions at elevated pressure have highlighted the parameters that must be optimized to manipulate ions efficiently. For example, racetrack effects and electrode geometry are vitally important to high resolution, high efficiency turning of ions at atmospheric pressure. Further, non-uniform electric fields can be used to focus ions with an ion funnel-like geometry, but defocusing fields near the electrode edges greatly hinder ion transmission. Further optimizations to the electric field and geometry are necessary to improve transmission.

CHAPTER 4. FOURIER TRANSFORM ION MOBILITY/MASS SPECTROMETRY FOR RECOGNITION OF RELATED COMPOUNDS

Portions of this work have been published in the journal *Analytical Chemistry* as the article: “Schrader, R. L.; Marsh, B. M.; Cooks, R. G., Fourier Transform Ion Mobility Linear Ion Trap Mass Spectrometer Frequency Encoding for Recognition of Related Compounds in a Single Acquisition, *Anal. Chem.* **2020**, 92, 5107-5115.”

4.1 Introduction

Drift tubes with a single entrance gate coupled to a fast mass analyzer, such as a time-of-flight instrument, must have a mass spectrometry sampling rate sufficient to extract mobility information in the millisecond regime from a single ion injection event. Quadrupole mass filters have been used as mass analyzers and detectors for drift tube ion mobility devices.¹⁰⁵ The quadrupole mass filter can either be used to analyze all ions in a transmission mode or can be used in a mass-selective mode to detect ions of a single m/z . Triple quadrupoles offer the addition of tandem mass spectrometry capabilities.¹⁰⁶⁻¹⁰⁸ Slow mass analyzers, such as quadrupole ion traps and Orbitraps, are unable to sample all the mobility information from a single injection of ions. The mass scan in a quadrupole ion trap occurs over 30 – 85 ms, which is much slower than the flight time in time-of-flight instruments.¹⁰⁹ One approach to overcome this is to sample a mobility selected packet of ions by scanning the delay between the opening of the first ion gate and a second ion gate at the exit of the drift cell. The ion mobility spectrum can be reconstructed from the MS intensity at each sampling point.^{110, 111} In this mode of operation, more than 99% of the ions generated at the ion source are not sampled at the mass spectrometer. The equations relating resolving power and signal-to-noise ratio in drift tube ion mobility have been published previously.¹¹²

Fourier transforms are utilized in mass spectrometry techniques such as Fourier Transform Ion Cyclotron Resonance¹¹³, Orbitraps^{114, 115}, in select quadrupole ion trap^{116, 117} and time-of-flight experiments.¹¹⁸ Fourier transform ion mobility (FT-IMS) is a recently reintroduced technique that has been used to increase the duty cycle when coupling drift tube ion mobility with ion traps^{119, 120} and Orbitraps.^{121, 122} The FT-IMS method increases the duty cycle to 25% which results in improved data acquisition times and increased instrumental sensitivity. Alternatively, an increase

in duty cycle can also be accomplished with the Hadamard transformation.¹²³⁻¹²⁵ The Hadamard transform has also been applied to time-of-flight mass spectrometry.^{126, 127}

Fourier transforms are utilized in mass spectrometry techniques such as Fourier Transform Ion Cyclotron Resonance¹¹³, Orbitraps^{114, 115}, in select quadrupole ion trap^{116, 117} and time-of-flight instruments.¹¹⁸ Fourier transform ion mobility (FT-IMS) is a recently reintroduced technique that has been used to increase the duty cycle when coupling drift tube ion mobility with ion traps^{119, 120} and Orbitraps.^{121, 122} The FT-IMS method increases the duty cycle to 25% which results in improved data acquisition times and increased instrumental sensitivity. Alternatively, an increase in duty cycle can also be accomplished with the Hadamard transformation.¹²³⁻¹²⁵ The Hadamard transform has also been applied to time-of-flight mass spectrometry.^{126, 127}

Ion mobility spectrometers have been fabricated using several non-traditional means including resistive glass¹²⁸, printed circuit boards¹²⁹⁻¹³¹, and metal-coated polymers.¹³² A 3D printed ion mobility spectrometer has recently been described as both a standalone device,¹⁰² as well as coupled to a mass spectrometer.¹¹⁰ Resolving powers ($t_d/\Delta t_d$ at FWHM) achieved for the standalone device were about 50 and when coupled to the mass spectrometer they were approximately 45. This ion mobility device was fabricated using polylactic acid/polyhydroxyalkanoate for the housing and conductive polyethylene terephthalate glycol modified polymer with multiwalled carbon nanotubes for the electrodes. This device was used here to perform FT-IMS experiments and to establish a methodology to obtain MS/MS information from all ions using a single FT-IMS experiment.

4.2 Experimental Methods

4.2.1 Chemicals

Tetraalkylammonium (TAA) bromide salts (C₂-C₈) were purchased from Sigma Aldrich (St. Louis, MO). TAAs were prepared in 100 μ M solutions in acetonitrile (Fisher Scientific, Hampton, NH). Amphetamine, 3,4-methylenedioxymethamphetamine (MDEA), acetyl norfentanyl oxalate, acetyl fentanyl, 4-fluoroisobutyrylfentanyl, trinitroglycerin (TNG), and HMX were purchased from Cerilliant (Round Rock, TX). Amphetamine solutions were diluted to 10 ppm from standards in methanol (Fisher Scientific) and 0.1% formic acid (Sigma-Aldrich). Fentanyl solutions were diluted to 25 ppm in methanol/0.1% formic acid. Explosives solutions were diluted to 10 ppm in

acetonitrile (Fisher Scientific). TAA bromide salts were observed as the positively charged cations and the drugs of abuse were observed as the protonated molecules. Explosives were observed as negatively charged adducts with chloride and nitrate.

4.2.2 3D Printed Ion Mobility Spectrometer

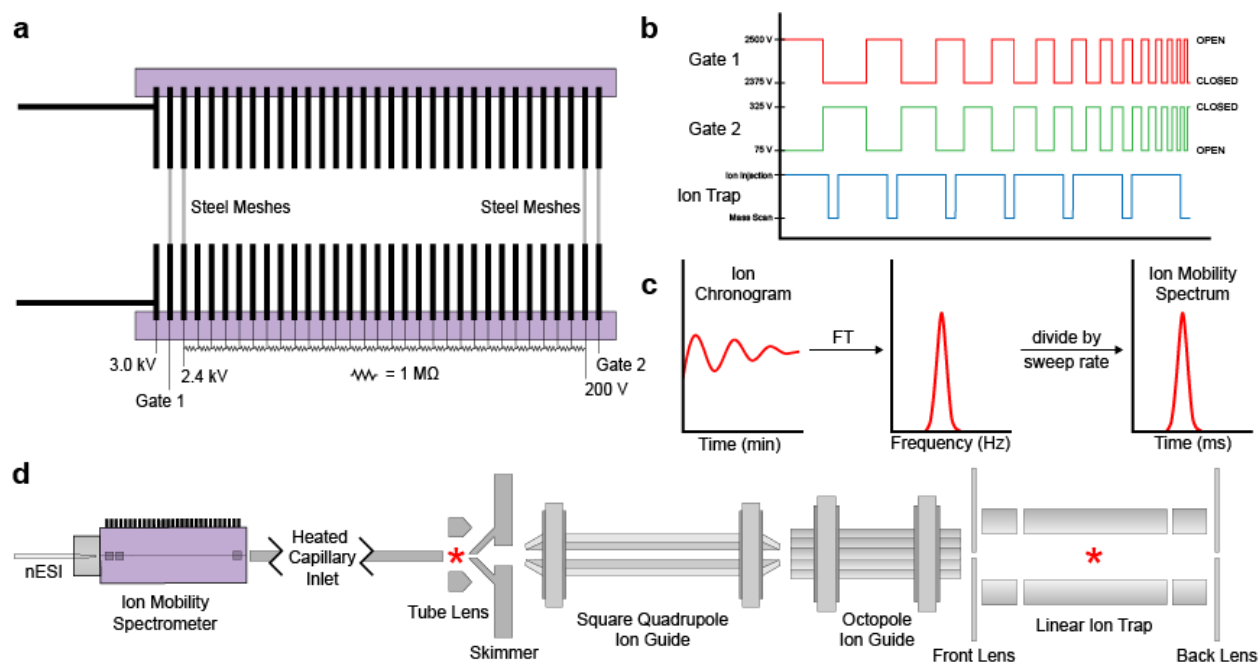


Figure 4.1 (a) Schematic of the 3D printed ion mobility device with ion gating performed by applying square waveforms to two sets of steel meshes at each end of the 31 drift lens spectrometer. The cylindrical extrusion can be seen on the first (focusing) electrode. Steel meshes are placed directly on the 3D printed electrodes. (b) Sweep voltages used to simultaneously open and close both gates with linearly increasing frequency. (c) Fourier transform of the ion chronogram gives the ion frequency distribution, which is converted into arrival time, i.e. the ion mobility spectrum, by division by the sweep rate. (d) Ion mobility spectrometer was placed directly in front of the mass spectrometer capillary inlet. Fragmentation (denoted by a red asterisk) can be made in either the source region or in the ion trap.

The 3D printed ion mobility spectrometer has been described in detail previously^{102, 110}. Briefly, polyethylene terephthalate glycol (PETG) modified polymer filament containing multi-walled carbon nanotubes (3DXTech, MI) was used to construct one focusing electrode and 31 drift electrodes. The drift electrode apertures were 7 mm in diameter. The first (focusing) electrode incorporated a 30 mm cylindrical extrusion prior to the lens structure used to confine the electrospray plume. The non-conductive housing was printed in two identical pieces from non-

conductive polylactic acid/polyhydroxyalkanoate (PLA/PHA) filament (ColorFabb, Belfeld, Netherlands). The housing of overall dimensions (approximately 46 x 66 x 83 mm) was fabricated such that the slots for the individual electrodes had a pitch of 2.54 mm. This distance was chosen as it is the standard distance between pins of a breadboard and as such allowed for standard header pins to be used to supply voltages to the device. A schematic of the device is provided in Figure 4.1a. Note that the first two and the final two drift electrodes were used as ion gates. Unlike some other ion mobility systems,^{112, 119} there is no ion desolvation region prior to the entrance ion gate as the plastic construction could not be heated.

4.2.3 Electronics

High voltage DC potentials were applied to the drift region through a custom voltage divider circuit built with a solderable breadboard (Mouser Electronics, Mansfield, TX) and using 29 resistors, each 1 M Ω . Electrical contact was made by inserting header pins from the breadboard into holes in the electrodes. Entrance and exit ion gates were created with four steel mesh screens (40 mesh, 66% transmission, E-Fab, Santa Clara, CA) placed on the 1st, 2nd, 30th and 31st drift electrode. The switched potential on the 1st drift electrode and 31st drift electrode was applied using a Behlke GHTS 60A (Billerica, MA) high voltage switch and a Directed Energy Inc. (DEI) PVX-4140 pulse generator (Fort Collins, CO). High voltage for the focusing electrode, both potentials for the Behlke switch, and the upper drift potential were supplied from a custom high voltage power supply. High voltage for the lower drift potential and DEI switch were supplied by a Spectrum Solutions (Russellton, PA) TD-500 power supply.

Table 4.1 Operating parameters for the bipolar ion mobility spectrometer.

Item	Parameter
Nanospray Voltage	$\pm 4500 - 5500$ V
Focusing Electrode	± 3000 V
Gate 1 Electrode (High/Low)	$\pm 2500/2375$ V
Drift High	± 2400 V
Drift Low	± 200 V
Gate 2 Electrode (High/Low)	$\pm 325/75$ V
Ion Gate Frequency Sweep	5 – 2005 Hz, 5 – 3005 Hz, 5 – 7005 Hz

The square wave input signal for both high voltage switches was supplied by a Keysight 33600A waveform generator (Santa Rosa, CA). High voltage parameters for each electrode are given in Table 4.1.

4.2.4 Mass Spectrometry

Borosilicate glass capillaries (i.d. 0.86 cm, o.d. 1.5 cm, 10 cm length) were purchased from Sutter Instruments (Navajo, CA) and pulled to an approximate 5 μm tip diameter with a P-97 Flaming/Brown tip puller (Sutter Instruments). The pulled capillaries were fitted in a Warner Instruments (Hamden, CT) E series electrode holder fitted with 0.127 mm diameter silver wire (Alfa Aesar, Ward Hill, MA, USA) and high voltage (4.5 – 5.5 kV) was applied to the holder. A Thermo Finnigan LTQ (San Jose, CA) was used for all experiments. The nanoelectrospray capillaries were placed approximately 1 – 2 mm from the first steel mesh. An Arduino Uno microcontroller (Arduino, Turin, Italy) with mechanical switch was used to trigger the waveform generator and the LTQ sample acquisition simultaneously using the Arduino digital output pins and LTQ contact closure. The 3D printed ion mobility device was placed approximately 1 mm in front of the mass spectrometer capillary inlet (Figure 1d). A 200 ms ion injection time (without automatic gain control) was used for all experiments, which corresponds to a scan time of approximately 240 – 280 ms, dependent on mass range. Capillary temperature, capillary voltage, and tube lens voltage were 200 °C, ± 15 V, and ± 65 V, respectively. For CID experiments, a 100 ms injection time with isolation window of m/z 100 and with the isolation mass being set at a value of mass-to-charge ratio that corresponded to the average of two adjacent TAA cations, while a normalized collision energy of 40 was used. When source fragmentation was of interest for MS/MS experiments on drugs of abuse, a voltage of 30 – 50 V was applied. Ion chronograms for each ion of interest were generated using XCalibur (Thermo Fisher) and Fourier transforms were calculated using MATLAB (MATLAB (The MathWorks, Inc., Natick, MA)).

4.2.5 Fourier Transform Ion Mobility Operation

In the FT-IMS mode of operation, both ion gates were opened and closed simultaneously using a square wave with an initial frequency of 5 Hz and final frequency of 2005 to 7005 Hz with the adjustment in frequency occurring linearly over a period of 4 minutes (Figure 4.1b). The

highest gating frequency that can be used is a function of the sampling rate of the mass analyzer as higher gating frequencies result in higher encoded frequencies. Waveforms were calculated in MATLAB and exported as '.csv' files to the waveform generator. Frequency encoding of FT-IMS has been described previously.^{121, 133} Briefly, ions are transmitted when their drift time (t_d) corresponds to the gating frequency ($\nu = 1/t_d$). Therefore, by sweeping the gate frequency over a range of frequencies, the signal (S) will be

$$S(\nu)_{max} = 0.5I_0 \text{ for } \nu = 0, 1/t_d, 2/t_d, 3/t_d, \dots$$

$$S(\nu)_{min} = 0 \text{ for } \nu = 0, 1/2t_d, 3/2t_d, 5/2t_d, \dots$$

at frequency ν where I_0 is the ion intensity without ion gating. For each ion, the resulting ion chronogram can be Fourier transformed to give the ion arrival frequency. The total signal versus time, the total ion chronogram, is the raw data obtained over the course of the experiment. The ion mobility spectrum can then be determined by dividing signal by the sweep rate in Hz/s. The steps connecting the ion chronogram to the ion mobility spectrum are shown in Figure 4.1c.

4.3 Results and Discussion

4.3.1 Characterization of Plastic IMS in Fourier Transform Mode

Previous experiments using the plastic, dual-gated ion mobility device have shown good resolution but low efficiency using the second ion gate as a mobility selection window.¹¹⁰ In order to compare this mode of operation with Fourier transform ion mobility, a seven tetraalkylammonium salt mixture ($C_2 - C_8$) was ionized by nanospray with the emitter placed inside the focusing electrode and the drift cell placed directly in front of the mass spectrometry capillary inlet. Three different waveforms were used in turn, each four minutes in length: 5 – 2005 Hz, 5 – 3005 Hz, and 5 – 7005 Hz.

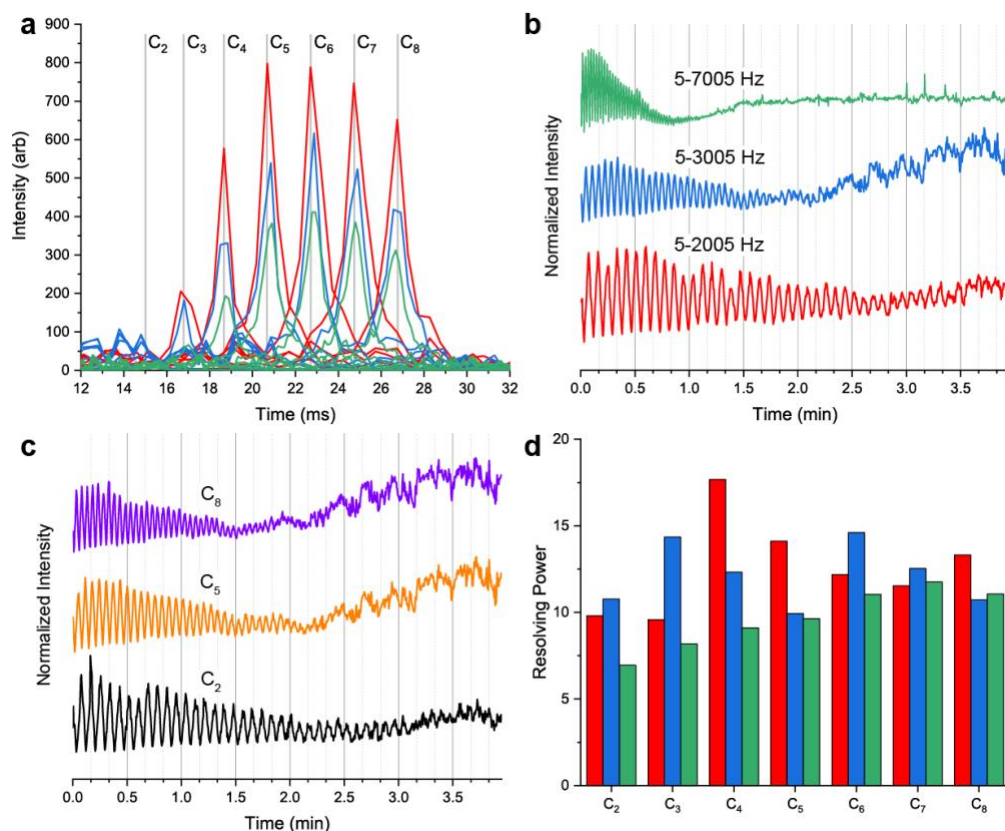


Figure 4.2 Ion mobility spectra for TAA cation mixture (C₂ – C₈) recorded using gate frequency sweeps: 5 – 2005 Hz (red), 5 – 3005 Hz (blue), and 5 – 7005 Hz (green). (b) Ion chronograms for the C₆ TAA for each frequency sweep show an increase in arrival frequency with sweep rate. (c) Ion chronograms for the C₂, C₅, C₈ TAA cation for the 5 – 3005 Hz frequency sweep show an increase in arrival frequency for ions with lower mobility. (d) Calculated resolving power for each TAA cation for each frequency sweep showing a decrease in resolving power at faster sweep rates.

Ion mobility spectra for the TAA mixture is shown in Figure 4.2a. The signal intensity of the C₂ TAA is small when compared with the other TAAs, and it is overshadowed when plotted on the same scale. In all cases, for higher sweep rates, higher arrival frequencies were observed, as shown for the C₆ TAA cation (Figure 4.2b). The arrival frequency for ions of higher mobility (lower drift time) is lower than that of an ion with lower mobility (Figure 4.2c). Resolving power was calculated by fitting each peak (e.g. in Figure 4.2a) to a Gaussian function and the resolving power is $R_p = t_d/\text{FWHM}$ where the FWHM is 2.353σ , where σ is obtained from the Gaussian fitting. This treatment is only valid for Gaussian peaks, which may not be true for the TAA cations given the small number of data points making up the peak. While the peaks in the observed spectrum are non-ideal, it is a valuable metric for comparisons. A simulation study based on a PCB ion mobility device has been done to optimize Gaussian peak response.⁴³ For higher gate sweep

frequencies, i.e. a higher sweep rate, both the absolute signal intensity as well as the resolving power was decreased.

The maximum resolving power achieved when the plastic IMS device was operated using the second gate as a mobility window selector was approximately 45,¹¹⁰ whereas the maximum resolving power observed using the Fourier transform mode was 17. A greater resolving power was reported using the FT-IMS mode of operation on a commercial Excellims ambient IMS system.¹¹⁹ The plastic IMS makes use of two Tyndall-Powell style gates constructed from two stainless steel meshes, as opposed to the Bradbury-Neilson gate of the commercial system. The ion packets produced by the Tyndall-Powell gate are not as narrow or as well-shaped like those of a Bradbury-Neilson gate.^{134, 135} This deviation from ideality in ion gating is likely to cause the reduction in resolving power in FT mode with the 3D printed spectrometer. Variation in dead time is another factor that may impact resolving power.¹³⁶ Although the resolving power is reduced, the signal intensity is increased by over an order of magnitude when compared to the mobility selection mode of operation.¹¹⁰

4.3.2 FT-IMS-CID of TAA Cations

Ion mobility data can be used to determine the family of precursors and product ions to which an ion belongs. Because the product ions maintain the precursor ion's frequency pattern,¹²⁰ they are expected to have the same arrival time distribution as the precursor. This allows for simultaneous collection of fragmentation and drift time information. Because all ions are being fragmented simultaneously, *a priori* knowledge of the precursor ion m/z is lost. However, for small molecules and singly charged ions, the precursor ion is likely to be the observed species with the largest m/z , though this may not be true for larger or more highly charged molecules.

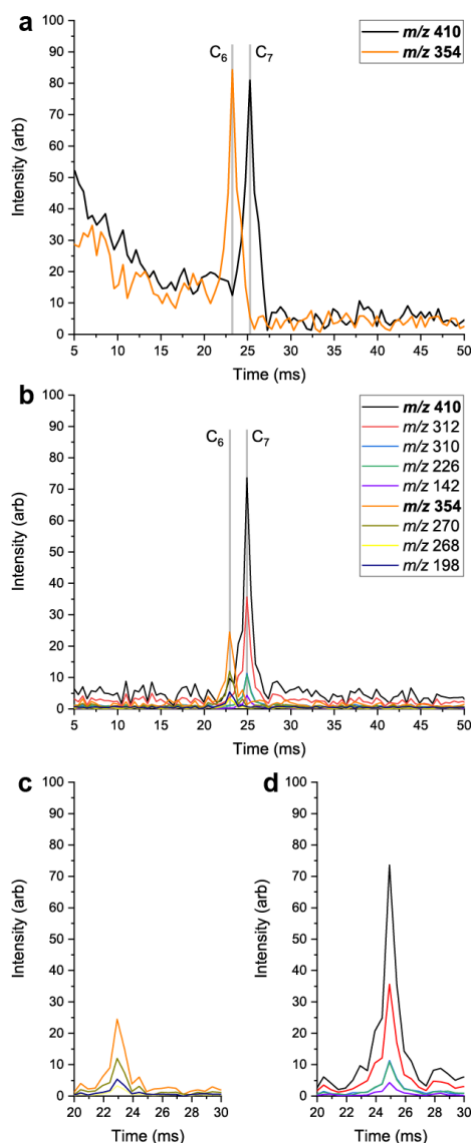


Figure 4.3 (a) Use of a 100 m/z window allowed isolation of the C₆ and C₇ TAA cation in the ion trap. (b) Excitation occurred at a secular frequency corresponding to the average mass. Fragment ions (generated in the ion trap) of each TAA cation had the same drift time as the precursor ion, as can be seen in the ion mobility spectrum. (c) Ion mobility spectrum of only the C₆ precursor and product ions showing that all peaks have the same drift time. (d) Ion mobility spectrum of only the C₇ precursor and product ions showing again that both peaks have the same drift time.

For non-specific CID fragmentation in the ion trap, a m/z 100 mass selection window was used, which is sufficient to isolate two adjacent TAA cations. The isolation of two TAA cations without fragmentation is shown in Figure 4.3a. In order to fragment the TAA cations, the excitation mass chosen was the average mass of the two TAA precursor cations. The resulting CID spectrum contains both precursor ions and product ions originating from each precursor. Plotting the ion

mobility spectrum with both precursors and their product ions show two distinct arrival times as product ions have the arrival time of their precursor (Figure 4.3b). Plotting each precursor and their fragments individually, as ion chronograms, highlights the fact that the precursors and product ions have the same drift time (Figure 4.3c and Figure 4.3d).

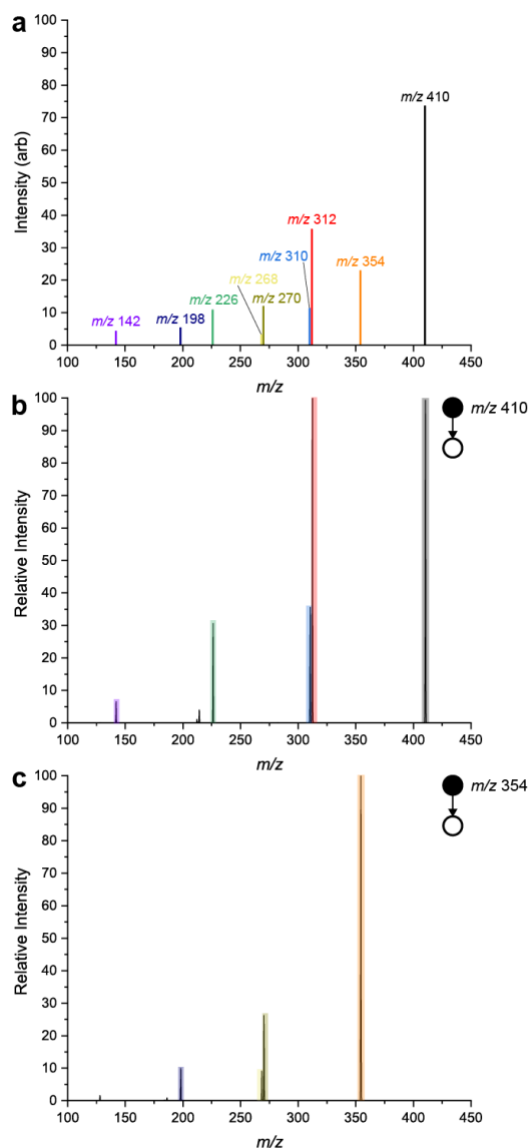


Figure 4.4 (a) Reconstructed mass spectrum using CID from the Fourier transform ion mobility spectrum of each ion. (b) Isolation and fragmentation of the C_6 TAA cation in the ion trap without ion mobility. (c) Isolation and fragmentation of the C_7 TAA cation in the ion trap without ion mobility. The CID mass spectrum shows product ions belonging to both precursors which can be identified using ion mobility information.

The CID mass spectrum (Figure 4.4a) of the C₆ and C₇ TAA isolation was reconstructed from the intensity values of the peaks in the FT-IMS spectrum. When compared with the product ion spectra recorded by the ion trap of the C₇ TAA cation (Figure 4.4b) and C₆ TAA cation (Figure 4.4c), it is clear that fragments from each precursor can be identified in the reconstructed mass spectrum. Although the mass spectrum collected contains products from all precursor ions, ion mobility information allows identification of which product ions are from the C₇ TAA cation and which product ions are from the C₆ TAA cation.

It is clear that drift time information can be used to determine families of precursors and product ions as seen for the data in Figure 4.3b. Furthermore, in this case, the precursor can be assumed to be the ion of the highest m/z at a particular arrival time. With using the LTQ ion trap, this method is limited by the selection window and uneven fragmentation due to excitation at a single resonance frequency. One can envisage the experiment being done without ion isolation and with use of a broadband excitation to cause fragmentation. This can be accomplished using a stored waveform inverse Fourier Transform (SWIFT) for excitation.¹³⁷ This contrasts with the typical ion trap CID experiment in which a single precursor is isolated, activated using a single resonance frequency, and subjecting the resulting product to mass analysis.¹³⁸

4.3.3 Separation and Fragmentation of Drugs of Abuse

The 3D printed plastic IMS combined with a mass spectrometer has been used previously to detect drugs of abuse.¹¹⁰ Drug compounds were shown to be resolved, though not to baseline. As is the case of the TAAs, signal intensity was improved by over an order of magnitude when comparing the original¹¹⁰ with the FT-IMS mode of operation. Based on the data gathered for the TAA cations, a gate waveform of 5 – 2005 Hz was chosen for further experiments. While lowering the sweep rate should further increase SNR and resolving power this necessarily increases the acquisition time. Therefore, the sweep rate used here was chosen to give the best SNR and resolving power.

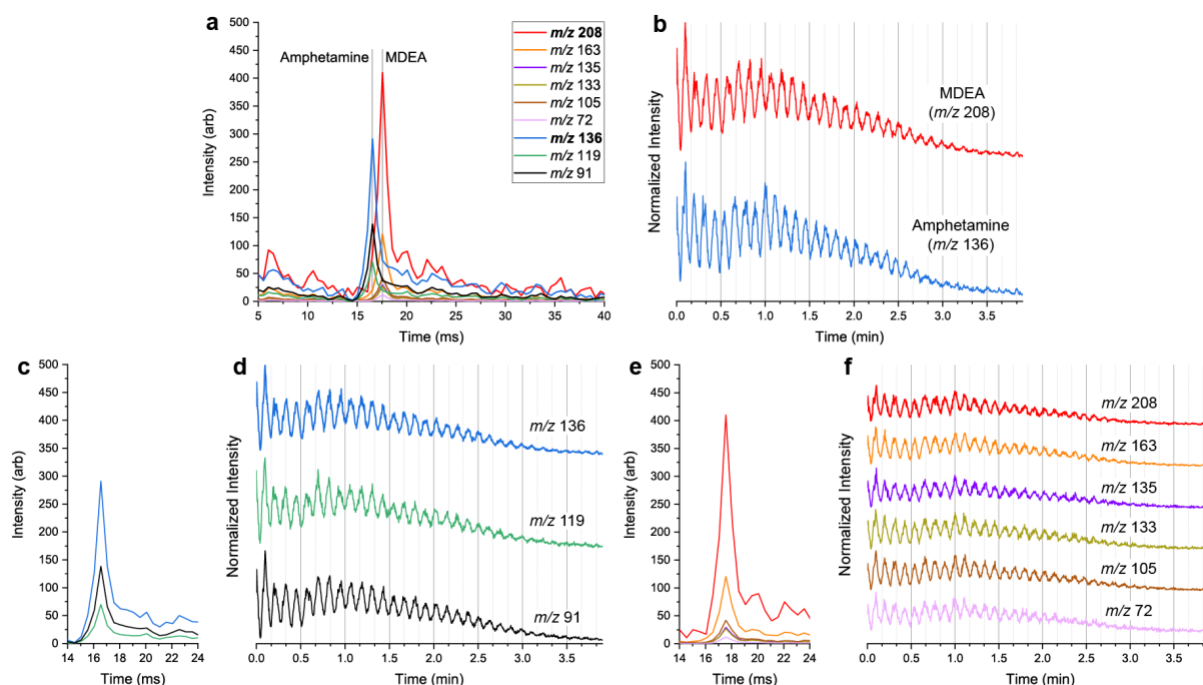


Figure 4.5 (a) Ion mobility spectra using in-source fragmentation of amphetamine (m/z 136) and its fragments m/z 119 and m/z 91 and MDEA (m/z 208) and its fragments m/z 163, m/z 135, m/z 133, m/z 105, and m/z 72. (b) Ion chronograms for precursor ions amphetamine and MDEA showing differences in arrival frequency corresponding to their differences in drift time. (c) Ion mobility spectra from the same data for only amphetamine and its fragment showing that all peaks have the same arrival time. (d) Ion chronograms for amphetamine and its fragment ions showing again that the ions of m/z 119 and m/z 91 maintain the frequency of the amphetamine precursor. (e) Ion mobility spectra (from the same data) for only MDEA and its fragment showing that all peaks have the same arrival time. (f) Ion chronograms for MDEA and its fragments again showing that the fragment ions maintain the frequency of the MDEA precursor.

CID can be performed in the source region prior to mass analysis. This results in a full scan mass spectrum containing product ions from all precursors. This method of non-targeted fragmentation was applied for the amphetamines and fentanyls. The ion mobility spectrum for amphetamine, MDEA, and for product ions of both precursors is given in Figure 4.5a. The difference in frequency of the two species can be seen in arrival time frequency which is encoded in each ion chronogram (Figure 4.5b). Amphetamine has two product ions, m/z 119 and m/z 91, which have the same arrival frequency as the amphetamine precursor (Figure 4.5c). When plotted alone (from the same data set), the ion mobility spectrum of amphetamine and its product ions shows that all three peaks have the same drift time (Figure 4.5d). Similarly, the fragments of MDEA, m/z 163, m/z 135, m/z 133, m/z 105, and m/z 72 were observed at the same drift time as

the MDEA precursor (Figure 4.5e). This is also reflected from the ion chromatograms of MDEA and its products having the same frequency (Figure 4.5f).

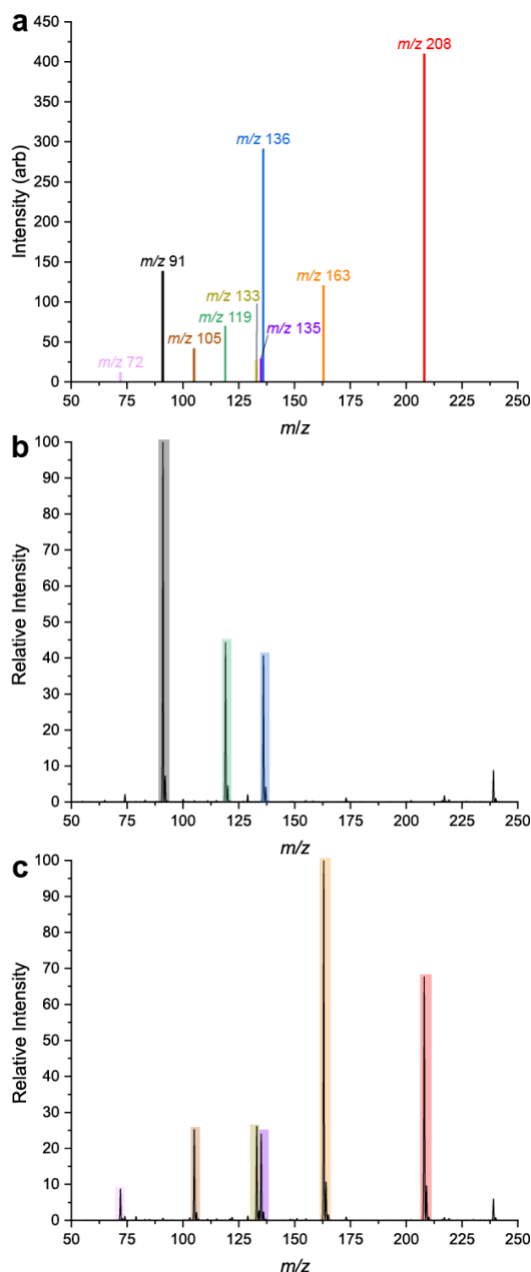


Figure 4.6 (a) Reconstructed in-source mass spectrum with in-source fragmentation from the Fourier transform for amphetamine, MDEA, and their detected fragments. (b) Full scan mass spectrum of amphetamine with source fragmentation without ion mobility showing amphetamine and its product ions. (c) Full scan mass spectrum of MDEA with source fragmentation without ion mobility showing MDEA and its product ions. Product ions coming from either amphetamine or MDEA can be identified with ion mobility information.

Using intensities from the ion mobility spectrum of all detected precursors and their fragments, an in-source CID mass spectrum can be reconstructed (Figure 4.6a) using the knowledge of precursors and product ions from the FT-IMS information. Mass spectra acquired using pure solutions of amphetamine and MDEA with in-source fragmentation are given in Figure 4.6b and 4.6c. When comparing the reconstructed spectrum with the standards, the precursor of the fragments can be easily identified. In-source fragmentation has the advantage of producing both MS² and MS³ products.

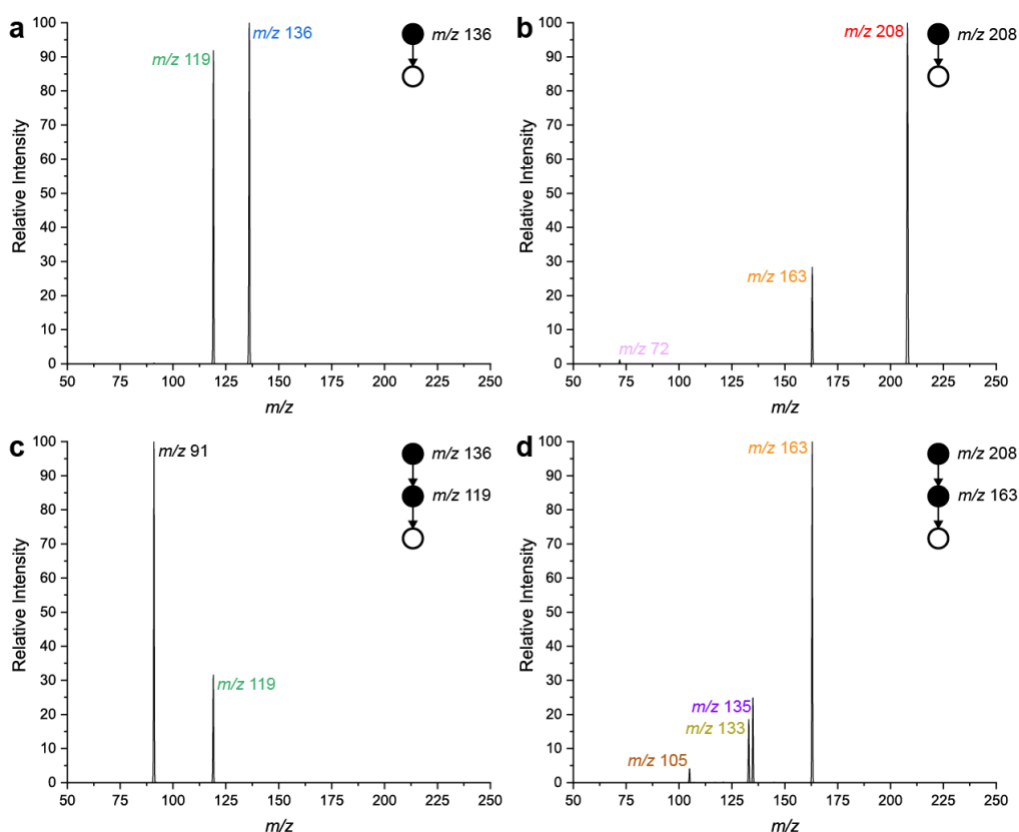


Figure 4.7 (a) MS² of amphetamine (b) MS³ of amphetamine and m/z 119 (c) MS² of MDEA (d) MS³ of MDEA and m/z 163

The ion trap fragmentation of amphetamine and MDEA are shown in Figure 4.7. Resonance excitation of the MDEA precursor yields mostly m/z 163 with a small amount of m/z 72. Subsequent fragmentation of m/z 163 yields m/z 135, 133, and 105. All of these ions are observed with in-source fragmentation because fragments produced in the source region may still

fragment before entering the ion trap. If excitation were to be done in the ion trap, this could also be achieved with a broadband excitation waveform.

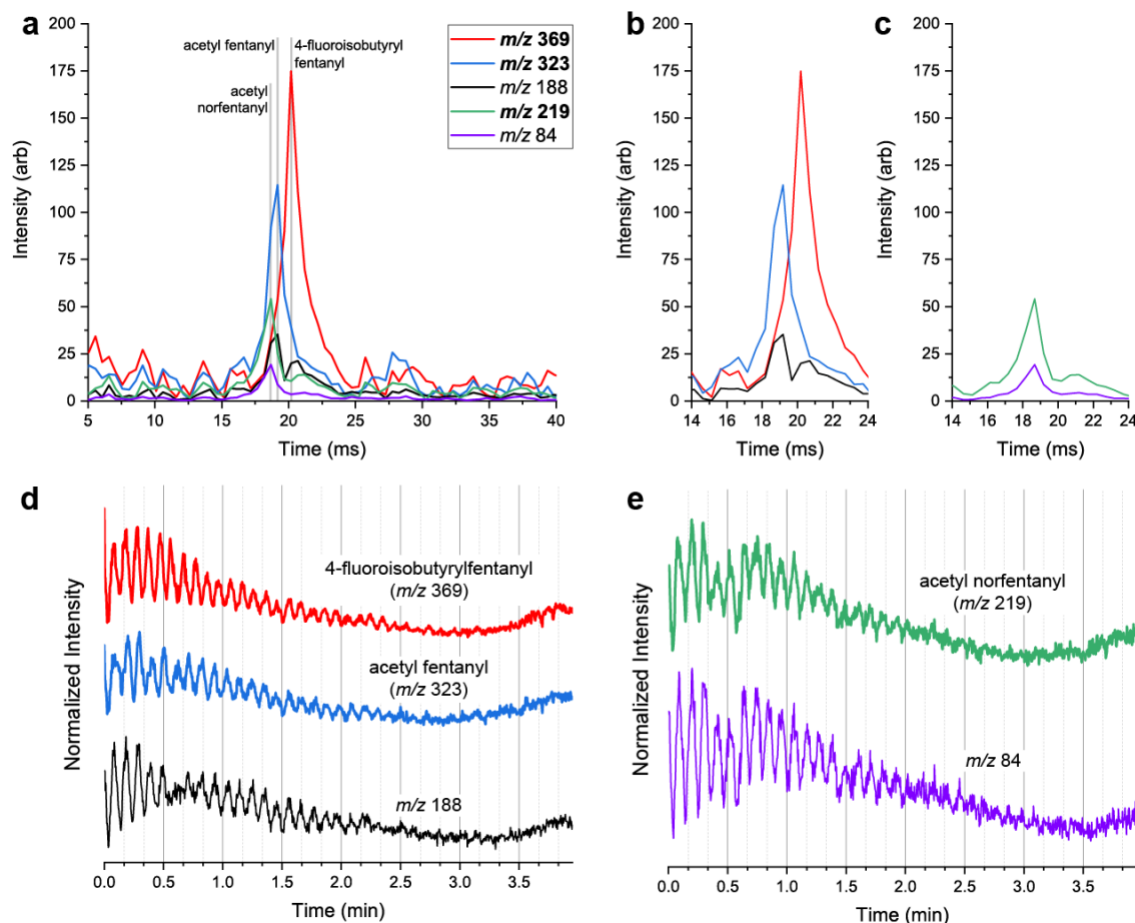


Figure 4.8 (a) Ion mobility spectra using in-source CID for 4-fluoroisobutyrylfentanyl (m/z 369), acetyl fentanyl (m/z 323), their fragment m/z 188, acetyl norfentanyl (m/z 219), and its fragment m/z 84. (b) Ion mobility spectra (from the same data) of only 4-fluoroisobutyrylfentanyl, acetyl fentanyl, and their fragment m/z 188. This fragment ion shows two peaks corresponding to the drift time of both of its precursors. (c) Ion mobility spectra (from the same data) of acetyl norfentanyl and its fragment m/z 84 showing that both peaks have the same arrival time. (d) Ion chronograms for 4-fluoroisobutyrylfentanyl, acetyl fentanyl, and their fragment m/z 188 showing that the product ion frequency is a combination of both precursor ion frequencies. (e) Ion chronograms for acetyl norfentanyl and its product ion m/z 84 showing that the product ion maintains the frequency of the acetyl norfentanyl precursor.

While the two amphetamines have different product ions, it is also possible to recognize samples with having two precursors fragmenting to the same product ions. Acetyl fentanyl and 4-fluoroisobutyrylfentanyl both fragment to m/z 188. In the same experiment, acetyl norfentanyl,

which fragments to a different product ion (m/z 84), was also examined. The ion mobility spectra of 4-fluoroisobutyryl fentanyl, acetyl fentanyl, and its product ion as well as acetyl norfentanyl and its product ion, are given in Figure 4.8a. The ion mobility spectra (plotted from the same data) for acetyl fentanyl and 4-fluoroisobutyryl fentanyl and their common product ion (plotted alone) show that the product ion has two peaks corresponding to the arrival times of both precursors (Figure 4.8b). Similarly, the ion mobility spectrum for acetyl norfentanyl and its fragment (plotted alone) show that the product ion has the same arrival time as the precursor (Figure 4.8c). The arrival frequencies for both precursors is different, and the product ion frequency is a combination of both of those frequencies (Figure 4.8d). The arrival frequencies for acetyl norfentanyl and its product ion, similar to the amphetamines, are the same (Figure 4.8e).

Performance achieved for the drugs of abuse in the FT-IMS method was comparable to that reported in the literature.¹¹⁰ However, signal intensity is greatly increased for the FT-IMS method. Therefore, using FT-IMS, simultaneous ion fragmentation and mobility information can be obtained more quickly (four minutes versus approximately 20 minutes) than the previously described method.

4.3.4 Separation of Explosives

Explosives have been analyzed using both standalone IMS instruments³⁵ as well as IMS-MS instruments^{106, 108}. These compounds are commonly observed in negative nanoelectrospray as chloride, nitrite, or nitrate adducts. In these experiments, only the chloride and nitrate adducts of the molecules were observed. A chloride adduct of the HMX dimer was observed as well.

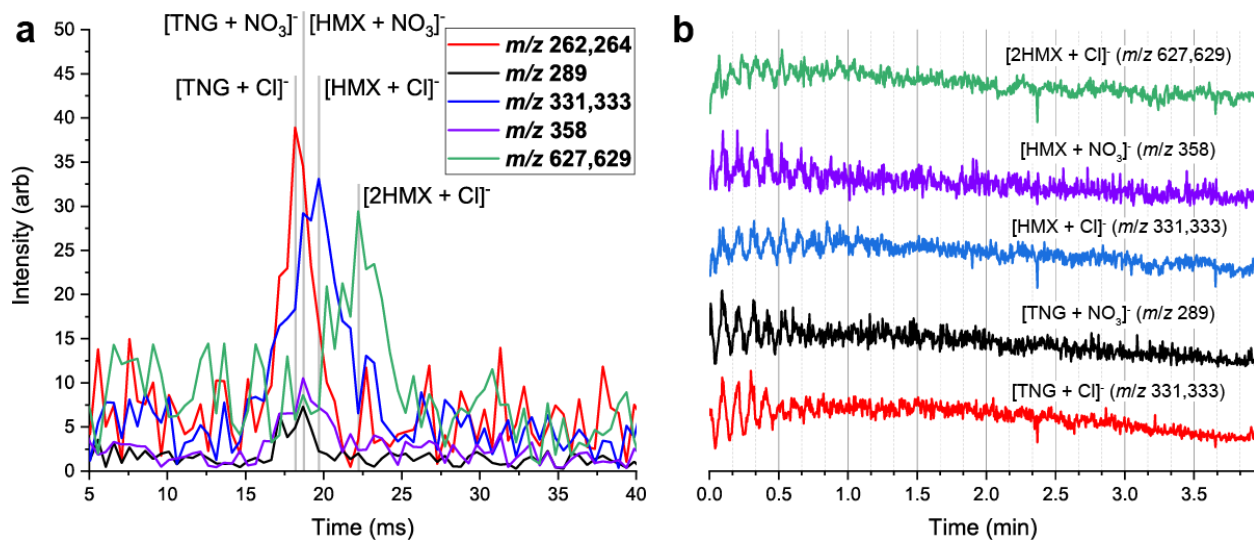


Figure 4.9 (a) Ion mobility spectra of trinitroglycerin chloride adduct (m/z 262,264), trinitroglycerin NO₃ adduct (m/z 289), HMX chloride adduct (m/z 331,333), HMX NO₃ adduct (m/z 358) and HMX dimer chloride adduct (m/z 627,629). (b) Ion chronograms for all ions. Low signal intensity for this measurement shows that poor signal intensity gives rise to artifacts in the Fourier transform, i.e. the ion mobility spectrum.

Negative ion mode experiments were performed analogously to positive mode experiments with opposite polarity of ion mobility voltages. The ion mobility spectra for each observed ion is shown in Figure 4.9a. Ion chronograms for each ion are shown in Figure 4.9b. Signal intensity for these experiments was much lower than for the experiments with the drugs of abuse, an effect seen in both the absolute signal intensity and in the signal/noise level. The noise seen in the frequency domain signal has a negative effect on the transformed arrival time distribution, i.e. the ion mobility spectrum.

Tandem mass spectrometry of chloride adducted HMX is limited to the fragmentation of the dimers back to monomers.^{139, 140} Moreover, the fragmentation of the NO₃ adduct is inefficient.¹⁴¹ As a result, attempts to perform fragmentation on the explosives were unsuccessful. The source fragmentation potential was either insufficient to induce fragmentation or resulted in a total loss in signal intensity. This highlights the need for broadband excitation capability to perform the experiment in the ion trap.

4.3.5 Optimization of Ion Gates

Two related ion gates commonly used for ion mobility spectrometers are the Tyndall Powell gate¹⁴² and the Bradbury-Nielson gate¹⁴³. In the Bradbury-Nielson gate, closely spaced, interdigitated wires are placed in a single plane. The gate is open when the potentials on the two sets of wires are the same. The gate is closed when the one set of wires is offset in voltage from the other. The performance of this gate is high, but the construction is quite difficult.¹⁴⁴⁻¹⁴⁶ Alternatively, the Tyndall-Powell gate is formed by two adjacent meshes in which the voltages are adjusted to either allow ions to pass or block them. The advantages of this gate versus the Bradbury-Nielson is the ease of construction.¹³⁵ The disadvantage of the Tyndall-Powell gate is that performance of the gate is inherently mobility dependent. Two parameters can be used to optimize the Tyndall-Powell gate: the voltage drop when the gate is open and the inter-mesh distance.

The distance between the two meshes was chosen such that the 3D printer was able to print an insulating wall between adjacent electrodes. Consequently, the distance was chosen to be approximately 1 mm. As the normally closed ion gate opens, ions enter the region between the two meshes. Therefore, these ions must exit this region before the gate closes again or they will not enter the drift tube. Moreover, if the inter-mesh distance is large a longer injection time will be required for any ions to exit the gating region.

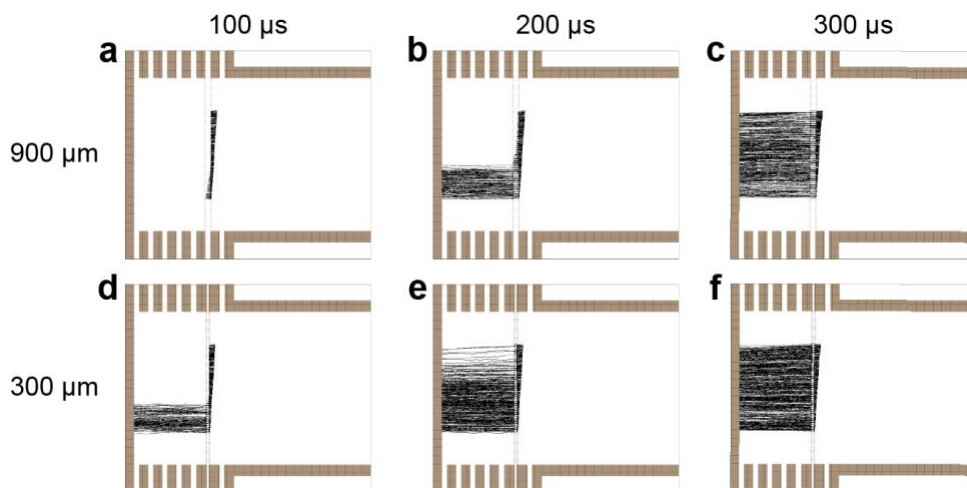


Figure 4.10 Simulation of Tyndall-Powell gate with inter-mesh distance of 900 μm vs 300 μm for various injection times. Ion initial positions were diagonal behind the first mesh. For the 300 μm inter-mesh distance even at the shortest injection time ions were able to pass through the gate whereas all ions are blocked for a 100 μs injection time with a 900 μs inter-mesh distance.

A simulation using SIMION was done to investigate the performance of two different inter-mesh distances. All other parameters between the two simulations were identical. Ions were started in a diagonal behind the first mesh. For the 900 μm inter-mesh distance, the ions are not travelling fast enough to traverse 900 μm in 100 μs . In contrast, for the 300 μm inter-mesh distance some of the ions are able to enter the drift region. In either case, as the injection time is increased more ions are able to enter the drift region. Note that the number of ions able to traverse this region could also be increased by increasing the drift voltage in this region (i.e., if the ions were going faster).

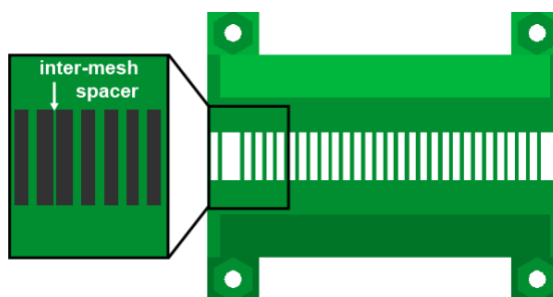


Figure 4.11 Fabrication of a 3D printed holder capable of sub-1 mm inter-mesh distance required the removal of the divider between those two electrodes and thicker electrodes to fill the space.

As discussed previously, fabrication limitations guided the choice of inter-mesh distance. In order to reduce this distance, the plastic dividing the space between these two electrodes was removed. A 300 μm spacer was printed using PLA/PHA and the electrodes were thickened to fill the entire space. To test the gates experimentally, the ion intensity and resolution for the C_6 TAA cation was measured for various gate opening times.

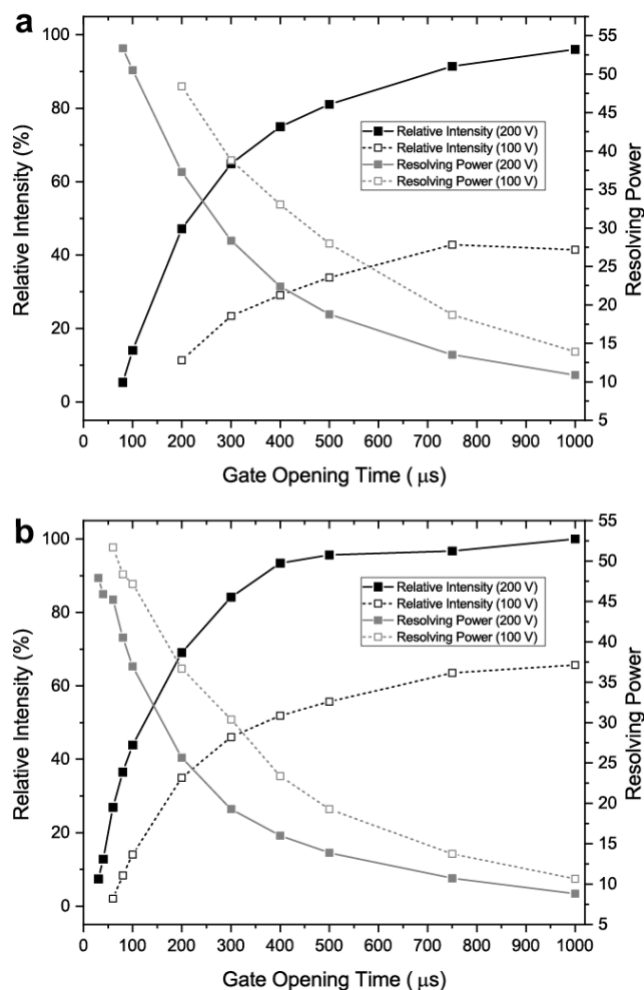


Figure 4.12 (a) Ion intensity and resolving power for a 900 μm inter-mesh distance for a voltage difference of 100 V and 200 V. (b) Ion intensity and resolving power for a 900 μm inter-mesh distance for a voltage difference of 100 V and 200 V. In both cases, both voltage and distance decrease the minimum gate opening time for which ion signal is observed.

For both the 300 μm and 900 μm gate, an increase in the voltage difference (100 V versus 200 V) resulted in lower minimum gate opening times required to see ion intensity. Further, the 300 μm also had a lower minimum gate opening time than the 900 μm gate as expected.

In FT-IMS, the ion injection time ranges in the experiment, depending on the frequency range, from 250 ms (5 Hz) to approximately 150 μs (7,005 Hz). Therefore, depending on the inter-mesh distance, a different number of ions would pass for these frequencies. It would also be expected that at a large enough frequency no signal would be observed because the pulses would be too short for any ions to pass. Interestingly, for the stainless steel meshes, this effect was not observed for the parameters described in Table 4.1.

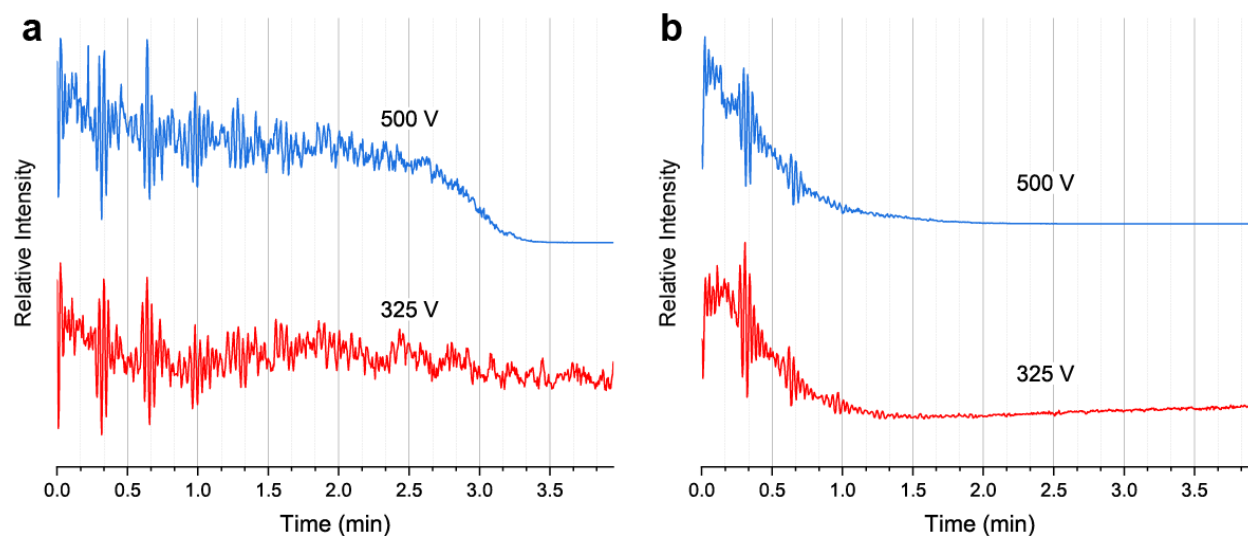


Figure 4.13 (a) Ion chronogram for TAA cations for a gate two blocking voltage of 500 V (blue) versus 325 V (red) for stainless steel mesh sheets. (b) Ion chronogram for TAA cations for gate two blocking voltage of 500 V (blue) versus 325 V (red) for MN17 nickel mesh.

As described in 3.2.4, the mesh was changed from a stainless-steel mesh manufactured by E-fab to a nickel mesh manufactured by Precision Eforming. Interestingly, for corresponding FT-IMS parameters, the observed signal is different. The blocking voltage for the second gate used for previously described experiments was 325 V and ion signal was observed through the entire experiment with stainless steel meshes (Figure 4.13a). When this voltage was raised to 500 V, ion signal drops to zero over the course of the experiment. With the nickel mesh (Figure 4.13b) the ion signal drops to zero much earlier in the experiment. Both of these experiments were performed with an inter-mesh distance of 900 μm . The reason for these effects is not fully understood but is likely a result of the pneumatic forces pulling the ions into the mass spectrometer overcoming the electrostatic forces at lower voltages (325 V). The thin wire of the nickel mesh versus the large metal area between holes in the stainless-steel mesh likely effect the electrostatic forces that the ions feel.

4.4 Conclusions

Fourier transform ion mobility offers the ability to efficiently couple a 3D printed drift tube for ion mobility to a linear ion trap. When compared to the low duty cycle mobility window selection mode of operation, resolving power was slightly reduced, but signal intensity was improved by more than an order of magnitude. This performance may be improved further by

employing a Bradbury-Neilson style gate as opposed to the Tyndall-Powell gate currently used. The Fourier transform mode of operation offered the additional advantage of the ability to perform simultaneous tandem mass spectrometry without ion isolation in the ion trap. Because product ions generated in the mass spectrometer maintain the arrival frequency of the precursors from which they were formed correlation of related precursors and product ions were easily recognized when all ions were fragmented without isolation. The use of a 3D printing technology to construct the ion mobility device allows easy implementation of this method into an analytical workflow. This is especially important in forensic applications where multiple analysis methods are desirable.

CHAPTER 5. COUPLING OF ATMOSPHERIC DRIFT TUBE ION MOBILITY WITH TWO-DIMENSIONAL TANDEM MASS SPECTROMETRY

Portions of this work have been published in the journal *Journal of the American Society of Mass Spectrometry* as the article: “Schrader, R. L.; Marsh, B. M.; Cooks, R. G., Atmospheric Pressure Drift Tube Ion Mobility Spectrometry Coupled with Two-Dimensional Tandem Mass Spectrometry, *J. Am. Soc. Mass Spectrom.* **2021**, DOI: 10.1021/jasms.1c00180”

5.1 Introduction

One of the advantages of performing ion mobility prior to mass spectrometry measurements is a reduction in chemical noise,¹⁴⁷ similar to the advantage achieved using tandem mass spectrometry.¹⁴⁸ The combination of ion mobility and tandem mass spectrometry has also proven useful.¹⁴⁹⁻¹⁵¹ The need for ion isolation to perform tandem mass spectrometry, either in time or space, reduces the quantity of data that can be acquired in a single experiment. Since the drift times and ion trap scan rates are both on the order of milliseconds, data collection is slow.¹⁵² Without multiplexing experiments^{124, 133}, more than 99.99% of the ions do not make it to the mass spectrometer. Therefore, ion isolation would make collecting ion mobility and tandem mass spectrometry data prohibitively time consuming.

2D MS/MS, performed in a linear ion trap, has been demonstrated to enable the collection of the entire MS/MS data domain in a single scan.^{153, 154} In this experiment, the product ion spectrum of every precursor ion is collected without ion isolation. In this work, 2D MS/MS has been combined with atmospheric pressure drift tube ion mobility to perform a single experiment in which both ion mobility data and the entire MS/MS data domain are collected.

5.2 Experimental

5.2.1 Chemicals

HPLC-grade methanol and acetonitrile were purchased from Fisher Scientific (Hampton, NH). Ammonium acetate was purchased from Sigma-Aldrich (St. Louis, MO). Standards of two phosphatidylethanolamines (12:0 and 18:1) and two phosphatidylcholines (14:1 and 18:1) were purchased from Avanti Polar Lipids (Alabaster, AL) as powders. A solution of the four lipids was

prepared at 100 ppm in 3.35:6.65:0.35 acetonitrile:methanol:300 mM ammonium acetate (v/v/v). Puromycin hydrochloride and terfenadine were purchased from Cayman Chemical Company (Ann Arbor, MI) and prepared at 10 ppm in methanol. Tetraalkylammonium bromides (C₂ – C₈) were purchased from Sigma Aldrich.

5.2.2 Drift Tube Ion Mobility

A 3D printed drift tube ion mobility spectrometer was used with slight modifications to previous iterations described elsewhere in detail.^{102, 110} Conductive polylactic acid (PLA) filament containing carbon black powder (Proto-pasta, Vancouver, WA) was used to construct one focusing electrode and 31 drift electrodes of 28 mm inner diameter. The focusing electrode incorporates a 25 mm cylindrical extrusion to confine the ions prior to the drift cell. The housing was printed from non-conductive polylactic acid/polyhydroxyalkanoate (PLA/PHA) filament (ColorFabb, Belfeld, Netherlands).

Entrance and exit gates (Tyndall-Powell) were created with four 90% transmission electroformed nickel mesh screens (MN17, Precision Eforming, Cortland, NY) affixed to the 1st, 2nd, 30th, and 31st drift electrode. Switched potentials on the 1st and 31st electrodes were supplied by a Behlke GHTS 60S (Billerica, MA) high voltage switch and a Directed Energy, Inc. PVX-4140 pulse generator (Fort Collins, CO), respectively. High voltages were supplied by a custom high voltage power supply and lower voltages were supplied by a Spectrum Solutions TD-500 power supply (Russelton, PA). A voltage divider constructed from a solderable breadboard (SB830, BusBoard Prototype Systems, Calgary, Canada) and 1 M Ω resistors (Stackpole Electronics, Inc., Raleigh, NC, $\pm 1\%$) was used to supply the voltages to the electrodes. The TTL input for the switched potentials were generated by a Keysight 33612A waveform generator (Santa Rosa, CA). The focusing electrode, gate 1, drift voltage, and gate 2 were operated at 3000 V, 2375/2500 V, 2400 V, 75/500 V.

Methods for coupling couple drift tube ion mobility with the relatively slow analysis time of the ion trap have been previously described.^{110, 152} Briefly, both the entrance and exit ion gates are normally closed. The first gate was opened for 400 μ s to allow ions to enter the drift tube. At varying times after the first gate (the drift time), the second gate was opened for 400 μ s. The time between these two pulses is stepped by 0.1 ms from low drift time to high drift time to collect the entire ion mobility spectrum.

5.2.3 Mass Spectrometry and 2D MS/MS

Ions were generated using nanoelectrospray ionization. Borosilicate glass capillaries (Sutter Instruments, Navajo, CA) of 10 cm length, 0.86 mm inner diameter, and 1.5 mm outer diameter were pulled to an approximately 5 μ m tip with a P-97 Flaming/Brown tip puller (Sutter Instruments). A Warner Instruments (Hamden, CT) E series electrode holder fitted with 0.2 mm diameter platinum wire (Sigma-Aldrich) was used to hold the pulled capillaries. High voltage (4.5 kV) was applied to the electrode holder from the LTQ.

A modified Thermo Finnigan LTQ (San Jose, CA) mass spectrometer was used to perform 2D MS/MS. The necessary modifications and experimental method to perform these experiments have been described in detail previously.^{153, 154} Briefly, with a constant RF trapping voltage, supplementary waveforms were applied to the x and y -rod pairs. A 900 ms inverse Mathieu q scan was applied to the y -rod pair to fragment precursor ions; meanwhile, sequential 1.5 ms inverse Mathieu q scans were applied to the x -rod pair with frequencies corresponding to masses lower than the current precursor. Nitrogen was used as the buffer gas with a pressure corresponding to 1.6 on the uncalibrated ion gauge. Excitation voltages of 900 mV (lipids) or 200 mV (drugs) and an ejection voltage of 2.2 V were used. Waveform spanned q values to 0.2. An RF modulation signal of 280 mV (lipids) or 300 mV (drugs) was applied in place of the normally supplied DC voltage to apply a constant RF voltage.

To align the two experiments in time, the IMS waveform generator was operated in burst mode with multiple IMS injection pulses at a rate of 20 Hz triggered on ion injection through the trigger supplied by the LTQ. An injection time of 800 ms was used (16 IMS pulses) which corresponds to a total scan time of approximately 2 seconds. For each drift time, 25 2D MS/MS spectra were collected and averaged. For 2D MS/MS experiments, this trigger is simultaneously used to start the supplementary waveforms. Data analysis was performed using MATLAB (The MathWorks, Inc., Natick, MA).

5.3 Results and Discussion

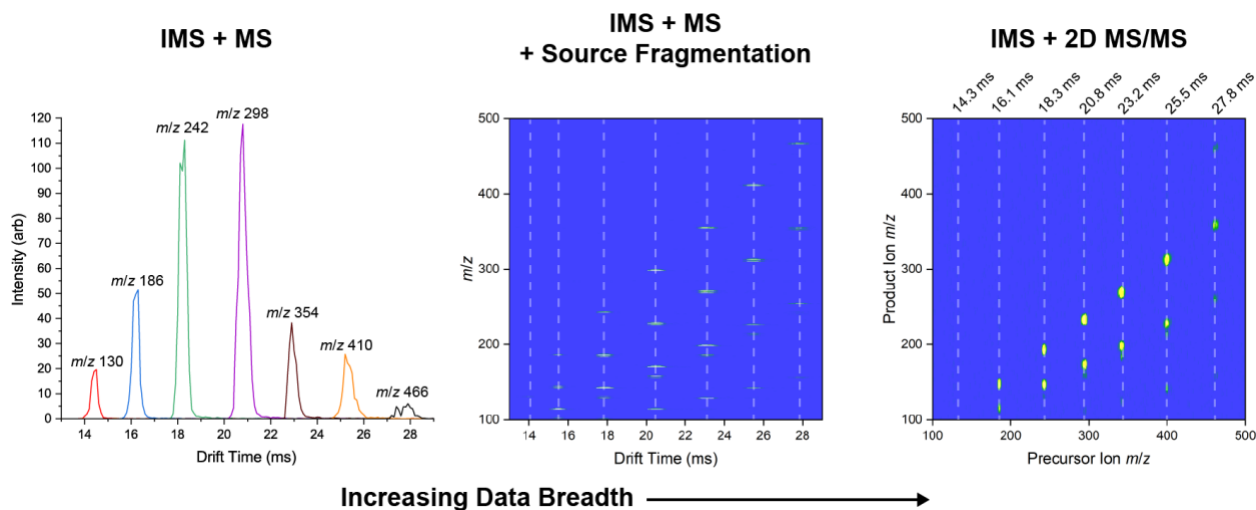


Figure 5.1. Ion mobility coupled with full scan MS gives mobility and mass information. By fragmenting ions in the source, related precursors and products were identified by their drift time. Ion mobility with 2D MS/MS gives mobility and the entire MS/MS data domain.

In a standalone ion mobility experiment, ions are separated in the drift tube and are detected when the ions impact a Faraday cup and are detected. This experiment gives only the mobility information of the ions. In order to increase the information obtained about the ions, IMS is coupled with mass spectrometry as the detector so that both mobility and mass-to-charge information are collected simultaneously. This was demonstrated for seven TAA cations in which the extracted ion intensity for each TAA m/z was used to plot the ion mobility spectrum (Figure 5.1a).

Ion fragmentation is an important diagnostic tool in the identification of molecules by mass spectrometry.¹⁵⁵ Though it is most often desirable to fragment ions after mass selection, ions can also be fragmented by the addition of energy in the source region prior to mass selection. Since the ions have been selected based on their mobility prior to entering the mass spectrometer, related precursors and product ions can be identified based on their ion mobility. This was demonstrated again with seven TAA cations in which a two-dimensional plot of mobility and m/z was obtained (Figure 5.1b). In order to achieve appropriate fragmentation for the wide range of TAAs, the source fragmentation energy was increased with m/z .¹⁵⁶ Fragments and unfragmented precursors were observed simultaneously. Unlike a traditional MS/MS experiment which includes ion isolation, in this experiment the identity of the precursor is unknown. While for small, singly charged

molecules the products will all be smaller in mass than the precursor, this will not be true for larger, multiply charged ions. Additionally, the ion mobility limits the resolving power for two different precursors and their fragments.

Coupling ion mobility with 2D MS/MS gives a four-dimensional data domain: mobility, precursor ion m/z , product ion m/z , and intensity. In the experiment, at each mobility “slice,” a 2D MS/MS spectrum was collected. Adding the intensities from each of these 2D MS/MS spectra gives a “total” 2D MS/MS spectrum (Figure 5.1c). The total 2D MS/MS is a reduction in the data as ion mobility information was also collected in the experiment. To reflect this, the drift for each TAA cation was annotated on the spectrum.

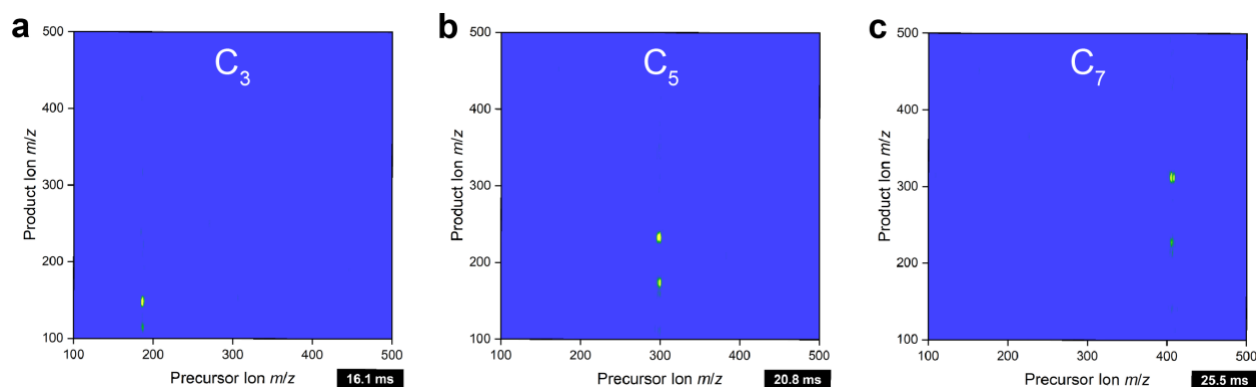


Figure 5.2 Individual 2D MS/MS spectra collected at various drift times where the (a) C₃, (b) C₅, and (c) C₇ TAA are the base peaks.

Another way of representing this data is a series of 2D MS/MS spectra. As the drift time is adjusted, different molecules will be observed by 2D MS/MS. An example of this is shown in Figure 5.2 where the 2D MS/MS spectra collected at 16.1 ms, 20.8 ms, and 25.5 ms, show the C₃, C₅, and C₇ TAA as the base peak, respectively.

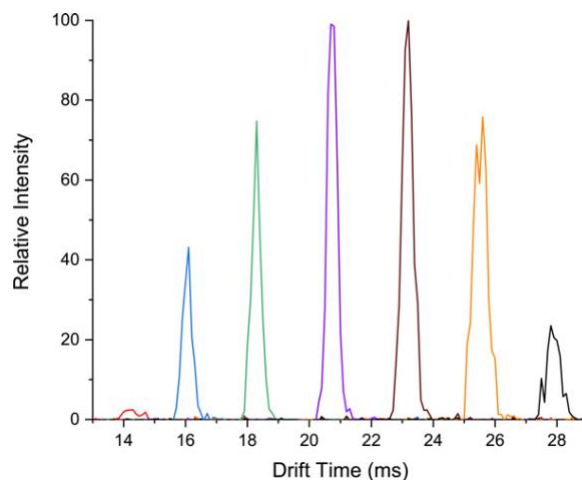


Figure 5.3 Ion mobility spectrum plotted from 2D MS/MS extracted ion intensities. The mobility spectrum is nearly identical to data collected with full scan MS but with additional MS/MS information collected in the same experiment.

The extracted ion intensities were also used to plot a traditional ion mobility spectrum (Figure 5.3). This spectrum looks nearly identical to the one in Figure 5.1a, but in the above spectrum the intensity comes from 2D MS/MS data versus full scan MS data. Whereas in Figure 5.1a, the entire amount of data collected is represented in the figure, this is not true for Figure 5.3. None of the 2D MS/MS data is represented in this spectrum. Both the total 2D MS/MS spectrum and the ion mobility spectrum do not capture the total amount of data collected in the experiment. This requires a fourth axis to display and is most easily seen as either an animated movie or a series of 2D MS/MS data domain plots. (Figure 5.2)

5.3.1 MS/MS Selective Ion Mobility Spectra for Lipids

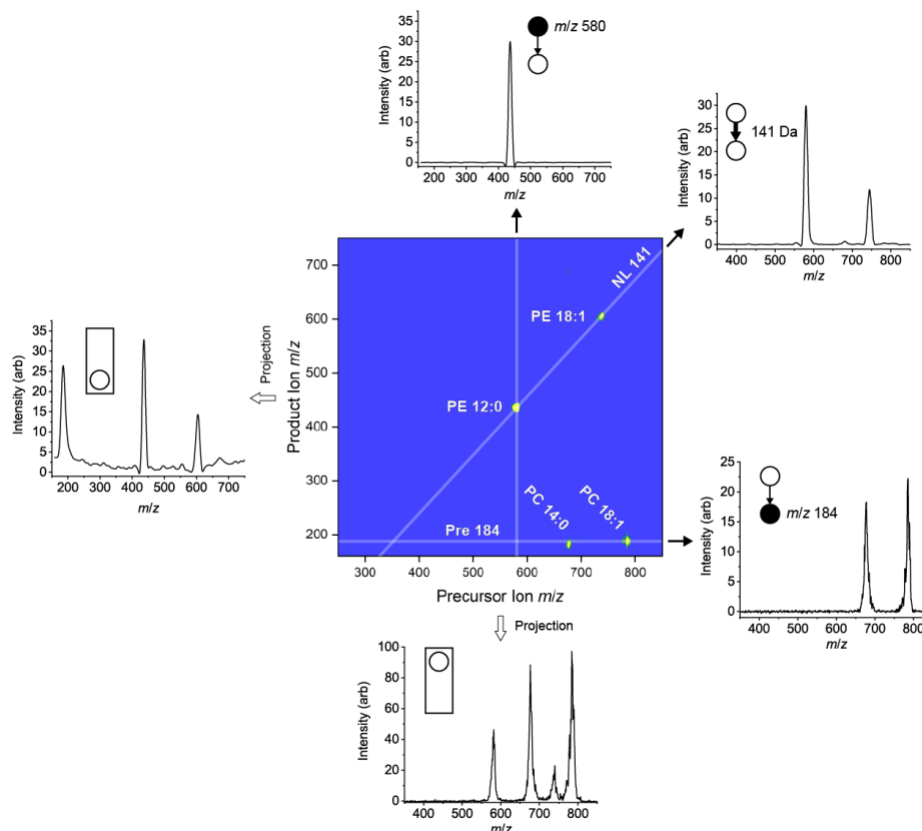


Figure 5.4. (a) Total 2D MS/MS spectrum of a lipid mixture showing characteristic fragments of m/z 184 for the two PCs and a characteristic neutral loss of 141 Da for the two PEs. Data projection and extraction give the mass spectra for each of the scan lines.

Ions from a standard mixture of four lipids, 12:0 PE, 18:1 PE, 14:0 PC, and 18:1 PC, were generated using nanoelectrospray. 2D MS/MS spectra were collected for drift times between 28 ms and 35 ms in 0.1 ms increments. The total 2D MS/MS spectrum is shown in Figure 5.4. The above figure is inspired by one appearing in a publication describing all possible MS/MS scan modes.¹⁵⁷ In this spectrum, the four lipids fall onto two characteristic scan lines (in addition to each product ion scan line). The PCs have a shared precursor ion of m/z 184, corresponding to the head group. The PEs have a shared neutral loss of 141 Da, also corresponding to the loss of the head group.¹⁵⁸ These scan lines can be used to plot the acquired ion mobility data. In addition to the scan lines, projection of the data onto the precursor or product ion axis results in the posterior and anterior mass spectrum, respectively.

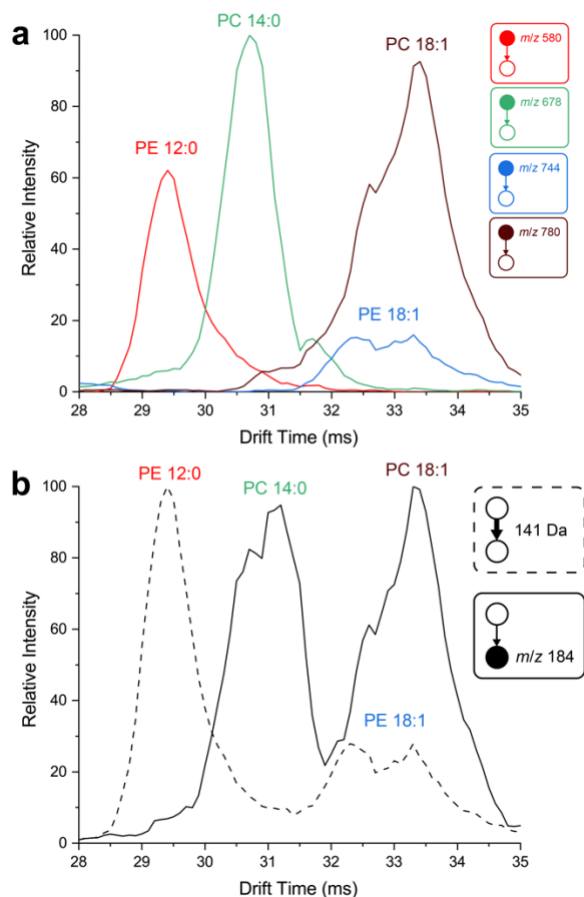


Figure 5.5 (a) Extracted product ion scan lines gives the ion mobility spectrum for each lipid. (b) Extracted neutral loss scan line gives an ion mobility spectrum of only the PEs in the mixture (dotted line) and extracted precursor ion scan line gives the ion mobility spectrum of the PCs in the mixture (solid line).

Ion intensities were determined from the mass spectrum collected at each mobility by adding the intensities along the MS/MS scan line. The resulting ion mobility spectra were filtered using a moving average and normalized. First, the ion mobility spectra were plotted from product ion scan lines for each lipid (Figure 5.5a). A box was added to the top right of the ion mobility spectrum with standard MS/MS nomenclature to denote scan line from which the ion intensity information is taken. Plotting the ion mobility data from product ion scan lines yields similar data to that can be collected with full scan mass spectra. Plotting ion mobility from precursor and product ion scan lines gives functional group specific ion mobility spectra. In Figure 5.5b, ion mobility spectra are shown from ion intensities from the m/z 184 precursor ion line (specific for PCs) and the 141 Da neutral loss line (specific for PEs). The PCs are shown as a solid line and the PEs as a dashed line. The use of 2D MS/MS allowed for the plotting of reduced data to aid in

analysis of the mixture, but the collected data was not reduced by ion isolation. The high dimensionality of the data (precursor ion m/z , product ion m/z , mobility, and ion intensity) makes the static display of all of the data simultaneously difficult.

5.3.2 Separation of Isobars Prior to 2D MS/MS by Ion Mobility Spectrometry

Ion mobility is often used for the separation of isobaric molecules.¹⁵⁹ High resolution mass spectrometers, such as time-of-flight¹⁶⁰ and Orbitrap¹¹⁴ analyzers, have sufficient mass resolution to separate isobaric molecules simply by their mass. Since the mass resolution for 2D MS/MS is insufficient to resolve isobaric molecules, ion mobility can be used for isobars of sufficient difference in collision cross section.

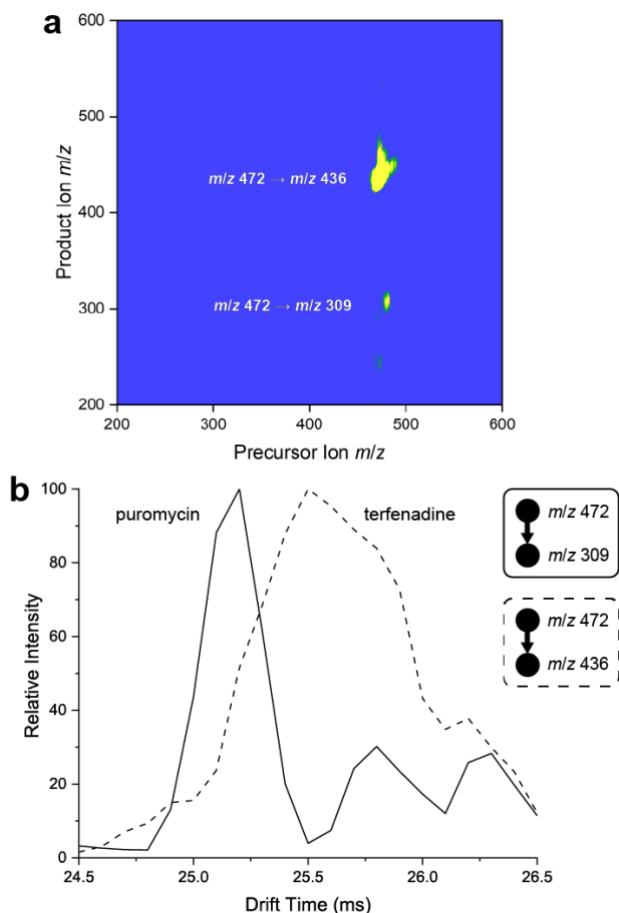


Figure 5.6. (a) Total 2D MS/MS spectrum of mixture of puromycin and terfenadine. Each compound shows a characteristic fragment, but since they are isobaric they cannot be distinguished from one compound with two fragments in 2D MS/MS. (b) Extracted normalized ion intensities for each MRM give the ion mobility spectrum for each compound.

Ions of puromycin and terfenadine were generated using nanoelectrospray. The literature values for their collision cross section are 204.4 and 226.8 Å², respectively.²⁶ 2D MS/MS spectra were collected for drift times from 24.5 ms to 26.5 ms in 0.1 ms increments. Both ions were observed as protonated molecules at m/z 472. The total 2D MS/MS (Figure 5.6a) shows two fragments for precursor m/z 472, one from puromycin (m/z 309) and another from terfenadine (m/z 436). Using the intensity from these two MRMs, ion mobility spectra are shown from each molecule. The ion mobility spectra were filtered using a moving average and normalized. The ion mobility was able to separate the two molecules by their collision cross section prior to 2D MS/MS analysis.

5.4 Conclusions

The combination of drift tube ion mobility with traditional ion trap CID experiments would be time consuming because of the mismatch between the duty cycle of the two measurements. The use of 2D MS/MS in a linear ion trap allows for the collection of the entire MS/MS data domain in a single scan along with ion mobility. This combination improves both methods symbiotically. The mobility measurement is improved by the ability to plot mobility spectra based on functional groups through specific MS/MS transitions. Equally, ion mobility has the ability separate isobars that would not be separated by 2D MS/MS.

REFERENCES

1. Douglas, D. J.; Konenkov, N. V., Mass resolution of linear quadrupole ion traps with round rods. *Rapid Commun. Mass Spectrom.* **2014**, 28 (21), 2252-2258.
2. Makarov, A., Orbitrap journey: taming the ion rings. *Nat. Comm.* **2019**, 10 (1), 3743.
3. Agrawaal, H.; Thompson, J. E., Additive manufacturing (3D printing) for analytical chemistry. *Talanta Open* **2021**, 3, 100036.
4. Gross, B.; Lockwood, S. Y.; Spence, D. M., Recent Advances in Analytical Chemistry by 3D Printing. *Anal. Chem.* **2017**, 89 (1), 57-70.
5. Shahrubudin, N.; Lee, T. C.; Ramlan, R., An Overview on 3D Printing Technology: Technological, Materials, and Applications. *Procedia Manuf.* **2019**, 35, 1286-1296.
6. Melchels, F. P. W.; Feijen, J.; Grijpma, D. W., A review on stereolithography and its applications in biomedical engineering. *Biomaterials* **2010**, 31 (24), 6121-6130.
7. Liu, J.; Wang, H.; Manicke, N. E.; Lin, J.-M.; Cooks, R. G.; Ouyang, Z., Development, Characterization, and Application of Paper Spray Ionization. *Anal. Chem.* **2010**, 82 (6), 2463-2471.
8. Wang, H.; Liu, J.; Cooks, R. G.; Ouyang, Z., Paper Spray for Direct Analysis of Complex Mixtures Using Mass Spectrometry. *Angew. Chem. Int. Ed.* **2010**, 49 (5), 877-880.
9. Espy, R. D.; Muliadi, A. R.; Ouyang, Z.; Cooks, R. G., Spray mechanism in paper spray ionization. *Int. J. Mass Spectrom.* **2012**, 325-327, 167-171.
10. Cooks, R. G.; Ouyang, Z.; Takats, Z.; Wiseman, J. M., Ambient Mass Spectrometry. *Science* **2006**, 311 (5767), 1566.
11. Zhang, C.; Glaros, T.; Manicke, N. E., Targeted Protein Detection Using an All-in-One Mass Spectrometry Cartridge. *J. Am. Chem. Soc.* **2017**, 139 (32), 10996-10999.
12. Salentijn, G. I.; Oleschuk, R. D.; Verpoorte, E., 3D-Printed Paper Spray Ionization Cartridge with Integrated Desolvation Feature and Ion Optics. *Anal. Chem.* **2017**, 89 (21), 11419-11426.
13. Salentijn, G. I. J.; Permentier, H. P.; Verpoorte, E., 3D-Printed Paper Spray Ionization Cartridge with Fast Wetting and Continuous Solvent Supply Features. *Anal. Chem.* **2014**, 86 (23), 11657-11665.
14. Brown, H. M.; Fedick, P. W., Rapid, low-cost, and in-situ analysis of per- and polyfluoroalkyl substances in soils and sediments by ambient 3D-printed cone spray ionization mass spectrometry. *Chemosphere* **2021**, 272, 129708.

15. Zemaitis, K. J.; Wood, T. D., Integration of 3D-printing for a desorption electrospray ionization source for mass spectrometry. *Rev. Sci. Instrum.* **2020**, *91* (10), 104102.
16. Martínez-Jarquín, S.; Moreno-Pedraza, A.; Guillén-Alonso, H.; Winkler, R., Template for 3D Printing a Low-Temperature Plasma Probe. *Anal. Chem.* **2016**, *88* (14), 6976-6980.
17. Brkić, B.; France, N.; Clare, A. T.; Sutcliffe, C. J.; Chalker, P. R.; Taylor, S., Development of quadrupole mass spectrometers using rapid prototyping technology. *J. Am. Soc. Mass. Spectrom.* **2009**, *20* (7), 1359-1365.
18. Clare, A. T.; Gao, L.; Brkić, B.; Chalker, P. R.; Taylor, S., Linear Ion Trap Fabricated Using Rapid Manufacturing Technology. *J. Am. Soc. Mass. Spectrom.* **2010**, *21* (2), 317-322.
19. Fico, M.; Maas, J. D.; Smith, S. A.; Costa, A. B.; Ouyang, Z.; Chappell, W. J.; Cooks, R. G., Circular arrays of polymer-based miniature rectilinear ion traps. *Analyst* **2009**, *134* (7), 1338-1347.
20. Vaezi, M.; Seitz, H.; Yang, S., A review on 3D micro-additive manufacturing technologies. *Int. J. Adv. Manuf. Tech* **2013**, *67* (5), 1721-1754.
21. Nikolaev, E.; Sudakov, M.; Vladimirov, G.; Velásquez-García, L. F.; Borisovets, P.; Fursova, A., Multi-electrode Harmonized Kingdon Traps. *J. Am. Soc. Mass. Spectrom.* **2018**, *29* (11), 2173-2181.
22. Buryakov, I. A.; Krylov, E. V.; Nazarov, E. G.; Rasulev, U. K., A new method of separation of multi-atomic ions by mobility at atmospheric pressure using a high-frequency amplitude-asymmetric strong electric field. *Int. J. Mass Spectrom. Ion Processes* **1993**, *128* (3), 143-148.
23. Verbeck, G. F.; Ruotolo, B. T.; Gillig, K. J.; Russell, D. H., Resolution equations for high-field ion mobility. *J. Am. Soc. Mass. Spectrom.* **2004**, *15* (9), 1320-1324.
24. Revercomb, H. E.; Mason, E. A., Theory of plasma chromatography/gaseous electrophoresis. Review. *Anal. Chem.* **1975**, *47* (7), 970-983.
25. Bush, M. F.; Hall, Z.; Giles, K.; Hoyes, J.; Robinson, C. V.; Ruotolo, B. T., Collision Cross Sections of Proteins and Their Complexes: A Calibration Framework and Database for Gas-Phase Structural Biology. *Anal. Chem.* **2010**, *82* (22), 9557-9565.
26. Hines, K. M.; Ross, D. H.; Davidson, K. L.; Bush, M. F.; Xu, L., Large-Scale Structural Characterization of Drug and Drug-Like Compounds by High-Throughput Ion Mobility-Mass Spectrometry. *Anal. Chem.* **2017**, *89* (17), 9023-9030.
27. Picache, J. A.; Rose, B. S.; Balinski, A.; Leaptrot, Katrina L.; Sherrod, S. D.; May, J. C.; McLean, J. A., Collision cross section compendium to annotate and predict multi-omic compound identities. *Chem. Sci.* **2019**, *10* (4), 983-993.

28. Mäkinen, M. A.; Anttalainen, O. A.; Sillanpää, M. E. T., Ion Mobility Spectrometry and Its Applications in Detection of Chemical Warfare Agents. *Anal. Chem.* **2010**, 82 (23), 9594-9600.
29. Puton, J.; Namieśnik, J., Ion mobility spectrometry: Current status and application for chemical warfare agents detection. *TrAC, Trends Anal. Chem.* **2016**, 85, 10-20.
30. Seto, Y.; Hashimoto, R.; Taniguchi, T.; Ohru, Y.; Nagoya, T.; Iwamatsu, T.; Komaru, S.; Usui, D.; Morimoto, S.; Sakamoto, Y.; Ishizaki, A.; Nishide, T.; Inoue, Y.; Sugiyama, H.; Nakano, N., Development of Ion Mobility Spectrometry with Novel Atmospheric Electron Emission Ionization for Field Detection of Gaseous and Blister Chemical Warfare Agents. *Anal. Chem.* **2019**, 91 (8), 5403-5414.
31. Satoh, T.; Kishi, S.; Nagashima, H.; Tachikawa, M.; Kanamori-Kataoka, M.; Nakagawa, T.; Kitagawa, N.; Tokita, K.; Yamamoto, S.; Seto, Y., Ion mobility spectrometric analysis of vaporous chemical warfare agents by the instrument with corona discharge ionization ammonia dopant ambient temperature operation. *Anal. Chim. Acta* **2015**, 865, 39-52.
32. Lawrence, A. H., Detection of drug residues on the hands of subjects by surface sampling and ion mobility spectrometry. *Forensic Sci. Int.* **1987**, 34 (1), 73-83.
33. Keller, T.; Miki, A.; Regenscheit, P.; Dirnhofer, R.; Schneider, A.; Tsuchihashi, H., Detection of designer drugs in human hair by ion mobility spectrometry (IMS). *Forensic Sci. Int.* **1998**, 94 (1), 55-63.
34. Garofolo, F.; Migliozi, V.; Roio, B.; Davies, J. H., Application of ion mobility spectrometry to the identification of trace levels of explosives in the presence of complex matrices. *Rapid Commun. Mass Spectrom.* **1994**, 8 (7), 527-532.
35. Ewing, R. G.; Atkinson, D. A.; Eiceman, G. A.; Ewing, G. J., A critical review of ion mobility spectrometry for the detection of explosives and explosive related compounds. *Talanta* **2001**, 54 (3), 515-529.
36. Li, L.; Chen, T.-C.; Ren, Y.; Hendricks, P. I.; Cooks, R. G.; Ouyang, Z., Mini 12, Miniature Mass Spectrometer for Clinical and Other Applications—Introduction and Characterization. *Anal. Chem.* **2014**, 86 (6), 2909-2916.
37. Snyder, D. T.; Pulliam, C. J.; Ouyang, Z.; Cooks, R. G., Miniature and Fieldable Mass Spectrometers: Recent Advances. *Anal. Chem.* **2016**, 88 (1), 2-29.
38. McDaniel, E. W.; Martin, D. W.; Barnes, W. S., Drift Tube-Mass Spectrometer for Studies of Low-Energy Ion-Molecule Reactions. *Rev. Sci. Instrum.* **1962**, 33 (1), 2-7.
39. Ibrahim, Y. M.; Baker, E. S.; Danielson, W. F.; Norheim, R. V.; Prior, D. C.; Anderson, G. A.; Belov, M. E.; Smith, R. D., Development of a new ion mobility time-of-flight mass spectrometer. *Int. J. Mass Spectrom.* **2015**, 377, 655-662.

40. Giles, K.; Ujma, J.; Wildgoose, J.; Pringle, S.; Richardson, K.; Langridge, D.; Green, M., A Cyclic Ion Mobility-Mass Spectrometry System. *Anal. Chem.* **2019**, *91* (13), 8564-8573.
41. Bohrer, B. C.; Merenbloom, S. I.; Koeniger, S. L.; Hilderbrand, A. E.; Clemmer, D. E., Biomolecule Analysis by Ion Mobility Spectrometry. *Ann. Rev. Anal. Chem.* **2008**, *1* (1), 293-327.
42. Gillig, K. J.; Chen, C.-H., Critical Examination of Gas-Phase Protein Conformation/Multimer Ion Formation by Electrospray Ion Mobility-Mass Spectrometry. *Anal. Chem.* **2013**, *85* (4), 2177-2182.
43. Ruotolo, B. T.; Gillig, K. J.; Stone, E. G.; Russell, D. H., Peak capacity of ion mobility mass spectrometry:: Separation of peptides in helium buffer gas. *J. Chromatogr. B* **2002**, *782* (1), 385-392.
44. Cuyckens, F., Ion mobility mass spectrometry: Small molecule applications. *Rapid Commun. Mass Spectrom.* **2019**, *33* (S2), 1-2.
45. Zhang, J. D.; Mohibul Kabir, K. M.; Donald, W. A., Chapter Three - Ion-Mobility Mass Spectrometry for Chiral Analysis of Small Molecules. In *Comprehensive Analytical Chemistry*, Donald, W. A.; Prell, J. S., Eds. Elsevier: 2019; Vol. 83, pp 51-81.
46. Shevlin, M., Practical High-Throughput Experimentation for Chemists. *ACS Med. Chem. Lett.* **2017**, *8* (6), 601-607.
47. Peng, T.; Nagy, G.; Trinidad, J. C.; Jackson, J. M.; Pohl, N. L. B., A High-Throughput Mass-Spectrometry-Based Assay for Identifying the Biochemical Functions of Putative Glycosidases. *ChemBioChem* **2017**, *18* (23), 2306-2311.
48. Macarron, R.; Banks, M. N.; Bojanic, D.; Burns, D. J.; Cirovic, D. A.; Garyantes, T.; Green, D. V. S.; Hertzberg, R. P.; Janzen, W. P.; Paslay, J. W.; Schopfer, U.; Sittampalam, G. S., Impact of high-throughput screening in biomedical research. *Nat. Rev. Drug Discov.* **2011**, *10*, 188.
49. Roddy, T. P.; Horvath, C. R.; Stout, S. J.; Kenney, K. L.; Ho, P.-I.; Zhang, J.-H.; Vickers, C.; Kaushik, V.; Hubbard, B.; Wang, Y. K., Mass Spectrometric Techniques for Label-free High-Throughput Screening in Drug Discovery. *Anal. Chem.* **2007**, *79* (21), 8207-8213.
50. Renom-Carrasco, M.; Lefort, L., Ligand libraries for high throughput screening of homogeneous catalysts. *Chem. Soc. Rev.* **2018**, *47* (13), 5038-5060.
51. Senkan, S. M., High-throughput screening of solid-state catalyst libraries. *Nature* **1998**, *394*, 350.

52. Jaman, Z.; Mufti, A.; Sah, S.; Avramova, L.; Thompson, D. H., High Throughput Experimentation and Continuous Flow Validation of Suzuki–Miyaura Cross-Coupling Reactions. *Chem. Eur. J.* **2018**, *24* (38), 9546-9554.
53. Wleklinski, M.; Loren, B. P.; Ferreira, C. R.; Jaman, Z.; Avramova, L.; Sobreira, T. J. P.; Thompson, D. H.; Cooks, R. G., High throughput reaction screening using desorption electrospray ionization mass spectrometry. *Chem. Sci.* **2018**.
54. Jaman, Z.; Sobreira, T. J. P.; Mufti, A.; Ferreira, C. R.; Cooks, R. G.; Thompson, D. H., Rapid On-Demand Synthesis of Lomustine under Continuous Flow Conditions. *Org. Process Res. Dev* **2019**.
55. Dreher, S. D.; Dormer, P. G.; Sandrock, D. L.; Molander, G. A., Efficient Cross-Coupling of Secondary Alkyltrifluoroborates with Aryl Chlorides—Reaction Discovery Using Parallel Microscale Experimentation. *J. Am. Chem. Soc.* **2008**, *130* (29), 9257-9259.
56. Lin, S.; Dikler, S.; Blincoe, W. D.; Ferguson, R. D.; Sheridan, R. P.; Peng, Z.; Conway, D. V.; Zawatzky, K.; Wang, H.; Cernak, T.; Davies, I. W.; DiRocco, D. A.; Sheng, H.; Welch, C. J.; Dreher, S. D., Mapping the dark space of chemical reactions with extended nanomole synthesis and MALDI-TOF MS. *Science* **2018**, *361* (6402), eaar6236.
57. Perera, D.; Tucker, J. W.; Brahmabhatt, S.; Helal, C. J.; Chong, A.; Farrell, W.; Richardson, P.; Sach, N. W., A platform for automated nanomole-scale reaction screening and micromole-scale synthesis in flow. *Science* **2018**, *359* (6374), 429.
58. Troshin, K.; Hartwig, J. F., Snap deconvolution: An informatics approach to high-throughput discovery of catalytic reactions. *Science* **2017**, *357* (6347), 175.
59. Buitrago Santanilla, A.; Regalado, E. L.; Pereira, T.; Shevlin, M.; Bateman, K.; Campeau, L.-C.; Schneeweis, J.; Bertritt, S.; Shi, Z.-C.; Nantermet, P.; Liu, Y.; Helmy, R.; Welch, C. J.; Vachal, P.; Davies, I. W.; Cernak, T.; Dreher, S. D., Nanomole-scale high-throughput chemistry for the synthesis of complex molecules. *Science* **2015**, *347* (6217), 49.
60. Leveridge, M.; Buxton, R.; Argyrou, A.; Francis, P.; Leavens, B.; West, A.; Rees, M.; Hardwicke, P.; Bridges, A.; Ratcliffe, S.; Chung, C.-w., Demonstrating Enhanced Throughput of RapidFire Mass Spectrometry through Multiplexing Using the JmjD2d Demethylase as a Model System. *J. Biomol. Screen.* **2013**, *19* (2), 278-286.
61. Sinclair, I.; Stearns, R.; Pringle, S.; Wingfield, J.; Datwani, S.; Hall, E.; Ghislain, L.; Majlof, L.; Bachman, M., Novel Acoustic Loading of a Mass Spectrometer: Toward Next-Generation High-Throughput MS Screening. *J. Lab Autom.* **2015**, *21* (1), 19-26.
62. Kennedy, D. F.; Messerle, B. A.; Rumble, S. L., Application of UV-Vis spectroscopy to high throughput screening of hydroamination catalysts. *New J. Chem.* **2009**, *33* (4), 818-824.

63. Dennis, E. A.; Ray, S. J.; Enke, C. G.; Gundlach-Graham, A. W.; Barinaga, C. J.; Koppenaal, D. W.; Hieftje, G. M., Distance-of-Flight Mass Spectrometry with IonCCD Detection and an Inductively Coupled Plasma Source. *J. Am. Soc. Mass. Spectrom.* **2016**, 27 (3), 371-379.
64. Schwartz, A. J.; Shelley, J. T.; Walton, C. L.; Williams, K. L.; Hieftje, G. M., Atmospheric-pressure ionization and fragmentation of peptides by solution-cathode glow discharge. *Chem. Sci.* **2016**, 7 (10), 6440-6449.
65. Nichols, C. M.; May, J. C.; Sherrod, S. D.; McLean, J. A., Automated flow injection method for the high precision determination of drift tube ion mobility collision cross sections. *Analyst* **2018**, 143 (7), 1556-1559.
66. Westphall, M. S.; Jorabchi, K.; Smith, L. M., Mass Spectrometry of Acoustically Levitated Droplets. *Anal. Chem.* **2008**, 80 (15), 5847-5853.
67. Gard, E.; Mayer, J. E.; Morrical, B. D.; Dienes, T.; Fergenson, D. P.; Prather, K. A., Real-Time Analysis of Individual Atmospheric Aerosol Particles: Design and Performance of a Portable ATOFMS. *Anal. Chem.* **1997**, 69 (20), 4083-4091.
68. Capel, A. J.; Rimington, R. P.; Lewis, M. P.; Christie, S. D. R., 3D printing for chemical, pharmaceutical and biological applications. *Nat. Rev. Chem.* **2018**, 2 (12), 422-436.
69. Tucker, L. H.; Conde-González, A.; Cobice, D.; Hamm, G. R.; Goodwin, R. J. A.; Campbell, C. J.; Clarke, D. J.; Mackay, C. L., MALDI Matrix Application Utilizing a Modified 3D Printer for Accessible High Resolution Mass Spectrometry Imaging. *Anal. Chem.* **2018**, 90 (15), 8742-8749.
70. Chambers, M. C.; Maclean, B.; Burke, R.; Amodei, D.; Ruderman, D. L.; Neumann, S.; Gatto, L.; Fischer, B.; Pratt, B.; Egertson, J.; Hoff, K.; Kessner, D.; Tasman, N.; Shulman, N.; Frewen, B.; Baker, T. A.; Brusniak, M.-Y.; Paulse, C.; Creasy, D.; Flashner, L.; Kani, K.; Moulding, C.; Seymour, S. L.; Nuwaysir, L. M.; Lefebvre, B.; Kuhlmann, F.; Roark, J.; Rainer, P.; Detlev, S.; Hemenway, T.; Huhmer, A.; Langridge, J.; Connolly, B.; Chadick, T.; Holly, K.; Eckels, J.; Deutsch, E. W.; Moritz, R. L.; Katz, J. E.; Agus, D. B.; MacCoss, M.; Tabb, D. L.; Mallick, P., A cross-platform toolkit for mass spectrometry and proteomics. *Nat. Biotechnol.* **2012**, 30, 918.
71. Littke, A. F.; Dai, C.; Fu, G. C., Versatile Catalysts for the Suzuki Cross-Coupling of Arylboronic Acids with Aryl and Vinyl Halides and Triflates under Mild Conditions. *J. Am. Chem. Soc.* **2000**, 122 (17), 4020-4028.
72. Miyaura, N.; Suzuki, A., Palladium-Catalyzed Cross-Coupling Reactions of Organoboron Compounds. *Chem. Rev.* **1995**, 95 (7), 2457-2483.
73. Brown, D. G.; Boström, J., Analysis of Past and Present Synthetic Methodologies on Medicinal Chemistry: Where Have All the New Reactions Gone? *J. Med. Chem.* **2016**, 59 (10), 4443-4458.

74. Reizman, B. J.; Wang, Y.-M.; Buchwald, S. L.; Jensen, K. F., Suzuki–Miyaura cross-coupling optimization enabled by automated feedback. *React. Chem. Eng.* **2016**, *1* (6), 658-666.
75. Elangovan, S.; Neumann, J.; Sortais, J.-B.; Junge, K.; Darcel, C.; Beller, M., Efficient and selective N-alkylation of amines with alcohols catalysed by manganese pincer complexes. *Nat. Comm.* **2016**, *7*, 12641.
76. Hammett, L. P., Linear free energy relationships in rate and equilibrium phenomena. *Trans. Faraday Soc.* **1938**, *34* (0), 156-165.
77. Hansch, C.; Leo, A.; Taft, R. W., A survey of Hammett substituent constants and resonance and field parameters. *Chem. Rev.* **1991**, *91* (2), 165-195.
78. Bain, R. M.; Pulliam, C. J.; Yan, X.; Moore, K. F.; Müller, T.; Cooks, R. G., Mass Spectrometry in Organic Synthesis: Claisen–Schmidt Base-Catalyzed Condensation and Hammett Correlation of Substituent Effects. *J. Chem. Educ.* **2014**, *91* (11), 1985-1989.
79. Brown, H. C.; Okamoto, Y., Electrophilic Substituent Constants. *J. Am. Chem. Soc.* **1958**, *80* (18), 4979-4987.
80. Yan, X.; Augusti, R.; Li, X.; Cooks, R. G., Chemical Reactivity Assessment Using Reactive Paper Spray Ionization Mass Spectrometry: The Katritzky Reaction. *ChemPlusChem* **2013**, *78* (9), 1142-1148.
81. Merenbloom, S. I.; Glaskin, R. S.; Henson, Z. B.; Clemmer, D. E., High-Resolution Ion Cyclotron Mobility Spectrometry. *Anal. Chem.* **2009**, *81* (4), 1482-1487.
82. Deng, L.; Ibrahim, Y. M.; Hamid, A. M.; Garimella, S. V. B.; Webb, I. K.; Zheng, X.; Prost, S. A.; Sandoval, J. A.; Norheim, R. V.; Anderson, G. A.; Tolmachev, A. V.; Baker, E. S.; Smith, R. D., Ultra-High Resolution Ion Mobility Separations Utilizing Traveling Waves in a 13 m Serpentine Path Length Structures for Lossless Ion Manipulations Module. *Anal. Chem.* **2016**, *88* (18), 8957-8964.
83. Adamson, B. D.; Coughlan, N. J. A.; Markworth, P. B.; Continetti, R. E.; Bieske, E. J., An ion mobility mass spectrometer for investigating photoisomerization and photodissociation of molecular ions. *Rev. Sci. Instrum.* **2014**, *85* (12), 123109.
84. Syka, J. E. P.; Schoen, A. E., Characteristics of linear and non-linear r.f.-only quadrupole collision cells. *Int. J. Mass Spectrom. Ion Processes* **1990**, *96* (1), 97-109.
85. Michalski, A.; Damoc, E.; Hauschild, J.-P.; Lange, O.; Wieghaus, A.; Makarov, A.; Nagaraj, N.; Cox, J.; Mann, M.; Horning, S., Mass Spectrometry-based Proteomics Using Q Exactive, a High-performance Benchtop Quadrupole Orbitrap Mass Spectrometer. *Mol. Cell. Proteomics* **2011**, *10* (9), M111.011015.

86. Michalski, A.; Damoc, E.; Lange, O.; Denisov, E.; Nolting, D.; Müller, M.; Viner, R.; Schwartz, J.; Remes, P.; Belford, M.; Dunyach, J.-J.; Cox, J.; Horning, S.; Mann, M.; Makarov, A., Ultra High Resolution Linear Ion Trap Orbitrap Mass Spectrometer (Orbitrap Elite) Facilitates Top Down LC MS/MS and Versatile Peptide Fragmentation Modes. *Mol. Cell. Proteomics* **2012**, *11* (3), O111.013698.
87. Mahaffy, P. R.; Lai, K., An electrostatic quadrupole deflector for mass spectrometer applications. *J. Vac. Sci. Technol. A* **1990**, *8* (4), 3244-3246.
88. Baird, Z.; Wei, P.; Cooks, R. G., Ion creation, ion focusing, ion/molecule reactions, ion separation, and ion detection in the open air in a small plastic device. *Analyst* **2015**, *140* (3), 696-700.
89. Iyer, K.; Marsh, B. M.; Capek, G. O.; Schrader, R. L.; Tichy, S.; Cooks, R. G., Ion Manipulation in Open Air Using 3D-Printed Electrodes. *J. Am. Soc. Mass. Spectrom.* **2019**, *30* (12), 2584-2593.
90. Webb, I. K.; Garimella, S. V. B.; Tolmachev, A. V.; Chen, T.-C.; Zhang, X.; Norheim, R. V.; Prost, S. A.; LaMarche, B.; Anderson, G. A.; Ibrahim, Y. M.; Smith, R. D., Experimental Evaluation and Optimization of Structures for Lossless Ion Manipulations for Ion Mobility Spectrometry with Time-of-Flight Mass Spectrometry. *Anal. Chem.* **2014**, *86* (18), 9169-9176.
91. Garimella, S. V. B.; Ibrahim, Y. M.; Webb, I. K.; Ipsen, A. B.; Chen, T.-C.; Tolmachev, A. V.; Baker, E. S.; Anderson, G. A.; Smith, R. D., Ion manipulations in structures for lossless ion manipulations (SLIM): computational evaluation of a 90° turn and a switch. *Analyst* **2015**, *140* (20), 6845-6852.
92. Fenn, J. B., Mass spectrometric implications of high-pressure ion sources. *Int. J. Mass Spectrom.* **2000**, *200* (1), 459-478.
93. Shaffer, S. A.; Tang, K.; Anderson, G. A.; Prior, D. C.; Udseth, H. R.; Smith, R. D., A novel ion funnel for focusing ions at elevated pressure using electrospray ionization mass spectrometry. *Rapid Commun. Mass Spectrom.* **1997**, *11* (16), 1813-1817.
94. Kelly, R. T.; Tolmachev, A. V.; Page, J. S.; Tang, K.; Smith, R. D., The ion funnel: Theory, implementations, and applications. *Mass Spectrom. Rev.* **2010**, *29* (2), 294-312.
95. Ahmed, E.; Xiao, D.; Kabir, K. M. M.; Fletcher, J.; Donald, W. A., Ambient Pressure Ion Funnel: Concepts, Simulations, and Analytical Performance. *Anal. Chem.* **2020**, *92* (24), 15811-15817.
96. Baird, Z.; Peng, W.-P.; Cooks, R. G., Ion transport and focal properties of an ellipsoidal electrode operated at atmospheric pressure. *Int. J. Mass Spectrom.* **2012**, *330-332*, 277-284.
97. Saf, R.; Goriup, M.; Steindl, T.; Hamedinger, T. E.; Sandholzer, D.; Hayn, G., Thin organic films by atmospheric-pressure ion deposition. *Nat. Mat.* **2004**, *3* (5), 323-329.

98. Han, F.; Li, H., A study of focusing effect in the variable DC electric fields Ion mobility spectrometry. *Int. J. Ion Mobil. Spectrom.* **2014**, *17* (1), 11-18.
99. Fort, K. L.; Silveira, J. A.; Russell, D. H., The Periodic Focusing Ion Funnel: Theory, Design, and Experimental Characterization by High-Resolution Ion Mobility-Mass Spectrometry. *Anal. Chem.* **2013**, *85* (20), 9543-9548.
100. Appelhans, A. D.; Dahl, D. A., SIMION ion optics simulations at atmospheric pressure. *Int. J. Mass Spectrom.* **2005**, *244* (1), 1-14.
101. Kaur-Atwal, G.; O'Connor, G.; Aksenov, A. A.; Bocos-Bintintan, V.; Paul Thomas, C. L.; Creaser, C. S., Chemical standards for ion mobility spectrometry: a review. *Int. J. Ion Mobil. Spectrom.* **2009**, *12* (1), 1-14.
102. Hollerbach, A.; Baird, Z.; Cooks, R. G., Ion Separation in Air Using a Three-Dimensional Printed Ion Mobility Spectrometer. *Anal. Chem.* **2017**, *89* (9), 5058-5065.
103. Lai, H.; McJunkin, T. R.; Miller, C. J.; Scott, J. R.; Almirall, J. R., The predictive power of SIMION/SDS simulation software for modeling ion mobility spectrometry instruments. *Int. J. Mass Spectrom.* **2008**, *276* (1), 1-8.
104. Potjewyd, J. Focusing of Ions in Atmospheric Pressure Gases Using Electrostatic Fields. Ph.D. Thesis, University of Toronto, 1983.
105. Wu, C.; Siems, W. F.; Hill, H. H., Secondary Electrospray Ionization Ion Mobility Spectrometry/Mass Spectrometry of Illicit Drugs. *Anal. Chem.* **2000**, *72* (2), 396-403.
106. Kozole, J.; Stairs, J. R.; Cho, I.; Harper, J. D.; Lukow, S. R.; Lareau, R. T.; DeBono, R.; Kuja, F., Interfacing an Ion Mobility Spectrometry Based Explosive Trace Detector to a Triple Quadrupole Mass Spectrometer. *Anal. Chem.* **2011**, *83* (22), 8596-8603.
107. Liuni, P.; Romanov, V.; Binette, M.-J.; Zaknoun, H.; Tam, M.; Pilon, P.; Hendrikse, J.; Wilson, D. J., Unambiguous Characterization of Analytical Markers in Complex, Seized Opiate Samples Using an Enhanced Ion Mobility Trace Detector-Mass Spectrometer. *Anal. Chem.* **2014**, *86* (21), 10772-10779.
108. Du, Z.; Sun, T.; Zhao, J.; Wang, D.; Zhang, Z.; Yu, W., Development of a plug-type IMS-MS instrument and its applications in resolving problems existing in in-situ detection of illicit drugs and explosives by IMS. *Talanta* **2018**, *184*, 65-72.
109. March, R. E., An Introduction to Quadrupole Ion Trap Mass Spectrometry. *J. Mass Spectrom.* **1997**, *32* (4), 351-369.
110. Hollerbach, A.; Fedick, P. W.; Cooks, R. G., Ion Mobility–Mass Spectrometry Using a Dual-Gated 3D Printed Ion Mobility Spectrometer. *Anal. Chem.* **2018**, *90* (22), 13265-13272.

111. Keelor, J. D.; Zambrzycki, S.; Li, A.; Clowers, B. H.; Fernández, F. M., Atmospheric Pressure Drift Tube Ion Mobility–Orbitrap Mass Spectrometry: Initial Performance Characterization. *Anal. Chem.* **2017**, 89 (21), 11301-11309.
112. Kirk, A. T.; Allers, M.; Cochems, P.; Langejuergen, J.; Zimmermann, S., A compact high resolution ion mobility spectrometer for fast trace gas analysis. *Analyst* **2013**, 138 (18), 5200-5207.
113. Marshall, A. G.; Hendrickson, C. L.; Jackson, G. S., Fourier transform ion cyclotron resonance mass spectrometry: A primer. *Mass Spectrom. Rev.* **1998**, 17 (1), 1-35.
114. Perry, R. H.; Cooks, R. G.; Noll, R. J., Orbitrap mass spectrometry: Instrumentation, ion motion and applications. *Mass Spectrom. Rev.* **2008**, 27 (6), 661-699.
115. Eliuk, S.; Makarov, A., Evolution of Orbitrap Mass Spectrometry Instrumentation. *Ann. Rev. Anal. Chem.* **2015**, 8 (1), 61-80.
116. Syka, J. E. P.; Williams, J. R.; Fieser, J. Fourier transform quadrupole mass spectrometer and method. 4,755,670, 1988.
117. Soni, M.; Frankevich, V.; Nappi, M.; Santini, R. E.; Amy, J. W.; Cooks, R. G., Broad-Band Fourier Transform Quadrupole Ion Trap Mass Spectrometry. *Anal. Chem.* **1996**, 68 (19), 3314-3320.
118. Knorr, F. J.; Ajami, M.; Chatfield, D. A., Fourier transform time-of-flight mass spectrometry. *Anal. Chem.* **1986**, 58 (4), 690-694.
119. Morrison, K. A.; Siems, W. F.; Clowers, B. H., Augmenting Ion Trap Mass Spectrometers Using a Frequency Modulated Drift Tube Ion Mobility Spectrometer. *Anal. Chem.* **2016**, 88 (6), 3121-3129.
120. Morrison, K. A.; Bendiak, B. K.; Clowers, B. H., Enhanced Mixture Separations of Metal Adducted Tetrasaccharides Using Frequency Encoded Ion Mobility Separations and Tandem Mass Spectrometry. *J. Am. Soc. Mass. Spectrom.* **2017**, 28 (4), 664-677.
121. Poltash, M. L.; McCabe, J. W.; Shirzadeh, M.; Laganowsky, A.; Clowers, B. H.; Russell, D. H., Fourier Transform-Ion Mobility-Orbitrap Mass Spectrometer: A Next-Generation Instrument for Native Mass Spectrometry. *Anal. Chem.* **2018**, 90 (17), 10472-10478.
122. Poltash, M. L.; McCabe, J. W.; Shirzadeh, M.; Laganowsky, A.; Russell, D. H., Native IM-Orbitrap MS: Resolving what was hidden. *TrAC, Trends Anal. Chem.* **2019**.
123. Clowers, B. H.; Siems, W. F.; Hill, H. H.; Massick, S. M., Hadamard Transform Ion Mobility Spectrometry. *Anal. Chem.* **2006**, 78 (1), 44-51.
124. Szumilas, A. W.; Ray, S. J.; Hieftje, G. M., Hadamard Transform Ion Mobility Spectrometry. *Anal. Chem.* **2006**, 78 (13), 4474-4481.

125. Tummalacherla, M.; Garimella, S. V. B.; Prost, S. A.; Ibrahim, Y. M., Toward artifact-free data in Hadamard transform-based double multiplexing of ion mobility-Orbitrap mass spectrometry. *Analyst* **2017**, *142* (10), 1735-1745.
126. Brock, A.; Rodriguez, N.; Zare, R. N., Characterization of a Hadamard transform time-of-flight mass spectrometer. *Rev. Sci. Instrum.* **2000**, *71* (3), 1306-1318.
127. Zare, R. N.; Fernández, F. M.; Kimmel, J. R., Hadamard Transform Time-of-Flight Mass Spectrometry: More Signal, More of the Time. *Angew. Chem. Int. Ed.* **2003**, *42* (1), 30-35.
128. Kaplan, K.; Graf, S.; Tanner, C.; Gonin, M.; Fuhrer, K.; Knochenmuss, R.; Dwivedi, P.; Hill, H. H., Resistive Glass IM-TOFMS. *Anal. Chem.* **2010**, *82* (22), 9336-9343.
129. Bohnhorst, A.; Kirk, A. T.; Zimmermann, S., Simulation aided design of a low cost ion mobility spectrometer based on printed circuit boards. *Int. J. Ion Mobil. Spectrom.* **2016**, *19* (2), 167-174.
130. Reinecke, T.; Clowers, B. H., Implementation of a flexible, open-source platform for ion mobility spectrometry. *HardwareX* **2018**, *4*, e00030.
131. Ibrahim, Y. M.; Hamid, A. M.; Deng, L.; Garimella, S. V. B.; Webb, I. K.; Baker, E. S.; Smith, R. D., New frontiers for mass spectrometry based upon structures for lossless ion manipulations. *Analyst* **2017**, *142* (7), 1010-1021.
132. Barmounis, K.; Maisser, A.; Schmidt-Ott, A.; Biskos, G., Lightweight differential mobility analyzers: Toward new and inexpensive manufacturing methods. *Aerosol Sci. Technol.* **2016**, *50* (1), 2-5.
133. Knorr, F. J.; Eatherton, R. L.; Siems, W. F.; Hill, H. H., Fourier Transform Ion Mobility Spectrometry. *Anal. Chem.* **1985**, *57* (2), 402-406.
134. Puton, J.; Knap, A.; Siodłowski, B., Modelling of penetration of ions through a shutter grid in ion mobility spectrometers. *Sens. Actuators B Chem.* **2008**, *135* (1), 116-121.
135. Chen, C.; Chen, H.; Li, H., Pushing the Resolving Power of Tyndall–Powell Gate Ion Mobility Spectrometry over 100 with No Sensitivity Loss for Multiple Ion Species. *Anal. Chem.* **2017**, *89* (24), 13398-13404.
136. Guntner, A. S.; Thalhamer, B.; Klampfl, C.; Buchberger, W., Collision cross sections obtained with ion mobility mass spectrometry as new descriptor to predict blood-brain barrier permeation by drugs. *Sci. Rep.* **2019**, *9* (1), 19182.
137. Julian, R. K.; Cooks, R. G., Broad-band excitation in the quadrupole ion trap mass spectrometer using shaped pulses created with the inverse Fourier transform. *Anal. Chem.* **1993**, *65* (14), 1827-1833.

138. Louris, J. N.; Cooks, R. G.; Syka, J. E. P.; Kelley, P. E.; Stafford, G. C.; Todd, J. F. J., Instrumentation, applications, and energy deposition in quadrupole ion-trap tandem mass spectrometry. *Anal. Chem.* **1987**, *59* (13), 1677-1685.
139. Cotte-Rodríguez, I.; Takáts, Z.; Talaty, N.; Chen, H.; Cooks, R. G., Desorption Electrospray Ionization of Explosives on Surfaces: Sensitivity and Selectivity Enhancement by Reactive Desorption Electrospray Ionization. *Anal. Chem.* **2005**, *77* (21), 6755-6764.
140. Fedick, P. W.; Bills, B. J.; Manicke, N. E.; Cooks, R. G., Forensic Sampling and Analysis from a Single Substrate: Surface-Enhanced Raman Spectroscopy Followed by Paper Spray Mass Spectrometry. *Anal. Chem.* **2017**, *89* (20), 10973-10979.
141. Garcia-Reyes, J. F.; Harper, J. D.; Salazar, G. A.; Charipar, N. A.; Ouyang, Z.; Cooks, R. G., Detection of Explosives and Related Compounds by Low-Temperature Plasma Ambient Ionization Mass Spectrometry. *Anal. Chem.* **2011**, *83* (3), 1084-1092.
142. Tyndall, A. M.; Powell, C. F., The Mobility of Ions in Pure Gases. *Proc. R. Soc. Lond.* **1930**, *129* (809), 162-180.
143. Bradbury, N. E.; Nielsen, R. A., Absolute Values of the Electron Mobility in Hydrogen. *Phys. Rev.* **1936**, *49* (5), 388-393.
144. Zuleta, I. A.; Barbula, G. K.; Robbins, M. D.; Yoon, O. K.; Zare, R. N., Micromachined Bradbury-Nielsen Gates. *Anal. Chem.* **2007**, *79* (23), 9160-9165.
145. Yoon, O. K.; Zuleta, I. A.; Robbins, M. D.; Barbula, G. K.; Zare, R. N., Simple Template-Based Method to Produce Bradbury-Nielsen Gates. *J. Am. Soc. Mass. Spectrom.* **2007**, *18* (11), 1901-1908.
146. Ni, K.; Guo, J.; Yu, Z.; Cao, L.; Yu, Q.; Qian, X.; Wang, X., A progressively reduced pretension method to fabricate Bradbury-Nielsen gates with uniform tension. *Rev. Sci. Instrum.* **2015**, *86* (11), 115105.
147. Kanu, A. B.; Dwivedi, P.; Tam, M.; Matz, L.; Hill Jr, H. H., Ion mobility-mass spectrometry. *J. Mass Spectrom.* **2008**, *43* (1), 1-22.
148. Yost, R. A.; Fetterolf, D. D., Tandem mass spectrometry (MS/MS) instrumentation. *Mass Spectrom. Rev.* **1983**, *2* (1), 1-45.
149. Zhu, F.; Lee, S.; Valentine, S. J.; Reilly, J. P.; Clemmer, D. E., Mannose7 Glycan Isomer Characterization by IMS-MS/MS Analysis. *J. Am. Soc. Mass. Spectrom.* **2012**, *23* (12), 2158-2166.
150. Zucker, S. M.; Lee, S.; Webber, N.; Valentine, S. J.; Reilly, J. P.; Clemmer, D. E., An Ion Mobility/Ion Trap/Photodissociation Instrument for Characterization of Ion Structure. *J. Am. Soc. Mass. Spectrom.* **2011**, *22* (9).

151. Harvey, D. J.; Crispin, M.; Bonomelli, C.; Scrivens, J. H., Ion Mobility Mass Spectrometry for Ion Recovery and Clean-Up of MS and MS/MS Spectra Obtained from Low Abundance Viral Samples. *J. Am. Soc. Mass. Spectrom.* **2015**, *26* (10), 1754-1767.
152. Clowers, B. H.; Hill, H. H., Mass Analysis of Mobility-Selected Ion Populations Using Dual Gate, Ion Mobility, Quadrupole Ion Trap Mass Spectrometry. *Anal. Chem.* **2005**, *77* (18), 5877-5885.
153. Snyder, D. T.; Szalwinski, L. J.; St. John, Z.; Cooks, R. G., Two-Dimensional Tandem Mass Spectrometry in a Single Scan on a Linear Quadrupole Ion Trap. *Anal. Chem.* **2019**, *91* (21), 13752-13762.
154. Szalwinski, L. J.; Holden, D. T.; Morato, N. M.; Cooks, R. G., 2D MS/MS Spectra Recorded in the Time Domain Using Repetitive Frequency Sweeps in Linear Quadrupole Ion Traps. *Anal. Chem.* **2020**, *92* (14), 10016-10023.
155. De Vijlder, T.; Valkenburg, D.; Lemièrre, F.; Romijn, E. P.; Laukens, K.; Cuyckens, F., A tutorial in small molecule identification via electrospray ionization-mass spectrometry: The practical art of structural elucidation. *Mass Spectrom. Rev.* **2018**, *37* (5), 607-629.
156. Baker, E. S.; Tang, K.; Danielson, W. F.; Prior, D. C.; Smith, R. D., Simultaneous fragmentation of multiple ions using IMS drift time dependent collision energies. *J. Am. Soc. Mass. Spectrom.* **2008**, *19* (3), 411-419.
157. Schwartz, J. C.; Wade, A. P.; Enke, C. G.; Cooks, R. G., Systematic delineation of scan modes in multidimensional mass spectrometry. *Anal. Chem.* **1990**, *62* (17), 1809-1818.
158. Harkewicz, R.; Dennis, E. A., Applications of Mass Spectrometry to Lipids and Membranes. *Annu. Rev. Biochem* **2011**, *80* (1), 301-325.
159. Cumeras, R.; Figueras, E.; Davis, C. E.; Baumbach, J. I.; Gràcia, I., Review on ion mobility spectrometry. Part 1: current instrumentation. *The Analyst* **2015**, *140* (5), 1376-1390.
160. Dickel, T.; Plaß, W. R.; Lippert, W.; Lang, J.; Yavor, M. I.; Geissel, H.; Scheidenberger, C., Isobar Separation in a Multiple-Reflection Time-of-Flight Mass Spectrometer by Mass-Selective Re-Trapping. *J. Am. Soc. Mass. Spectrom.* **2017**, *28* (6), 1079-1090.

VITA

Robert L. Schrader was born in State College, PA and moved to O'Fallon, IL; Watertown, NY; and Asheville, NC before settling in Rochester, NY. He earned a bachelor's degree *summa cum laude* in chemistry with a minor in mathematics from the State University of New York at Fredonia in 2016. His undergraduate research at Fredonia was on polyaromatic hydrocarbon contamination of soils in the Buffalo, NY area using gas chromatography/mass spectrometry. During his undergraduate education he completed two NSF REU programs: one at the State University of New York at Buffalo and the other at the University of Rochester. Both research experiences were computational in nature: the first on the calculation of π to π^* excitation energies of rhodamine-like dye derivatives and the second on the benchmarking of RNA design software packages.


Robert began his doctoral studies in 2016 and later joined the group of R. Graham Cooks. His early work in the group involved the modification of a commercial 3D printer to perform high-throughput reaction screening. He used the knowledge that he learned about 3D printers to study fundamentals of ions at atmospheric pressure using simulations and 3D printed devices. Along with fundamental studies, he worked on applications of a 3D printed ion mobility spectrometer with ion trap mass spectrometry. This work has resulted in the publication of eight peer-reviewed publications with one more forthcoming.

LIST OF PUBLICATIONS

1. Snyder, D. T.; Szalwinski, L. J.; Schrader, R. L.; Pirro, V.; Hilger, R.; Cooks, R. G., Precursor and Neutral Loss Scans in an RF Scanning Linear Quadrupole Ion Trap. *J. Am. Soc. Mass Spectrom.* **2018**, 29, 1345-1354.
2. Fedick, P. W.; Schrader, R. L.; Ayrton, S. T.; Pulliam, C. J.; Cooks, R. G. Process Analytical Technology for On-line Monitoring of Organic Reactions by Mass Spectrometry and UV-Vis Spectroscopy. *J. Chem. Educ.* **2019**, 96, 124-133.
3. Schrader, R. L.; Fedick, P. W.; Mehari, T. F.; Cooks, R. G. Accelerated Chemical Synthesis: Three Ways of Performing the Katritzky Transamination Reaction, *J. Chem. Educ.* **2019**, 96, 360-365.
4. Schrader, R. L.; Ayrton, S. T.; Kaerner, A.; Cooks, R. G. High Throughput, Low Cost Reaction Screening using a Modified 3D Printer. *Analyst*, **2019**, 144, 4978-4984.
5. Iyer, K; Marsh, B. M.; Capek, G. O.; Schrader, R. L.; Tichy, S.; Cooks, R. G. Ion Manipulation in Open Air Using 3D-Printed Electrodes. *J. Am. Soc. Mass Spectrom.* **2019**, 30, 2584-2593.
6. Schrader, R. L.; Marsh, B. M.; Cooks, R. G., Fourier Transform Ion Mobility Linear Ion Trap Mass Spectrometer Frequency Encoding for Recognition of Related Compounds in a Single Acquisition, *Anal. Chem.* **2020**, 92, 5107-5115.
7. Schrader, R. L.; Marsh, B. M.; Cooks, R. G., Temporal Distribution of Ions in Ambient Pressure Drift Tubes with Turns, *Int. J. Mass Spectrom.* **2020**, 456, 116391
8. Schrader, R. L.; Marsh, B. M.; Cooks, R. G., Atmospheric Pressure Drift Tube Ion Mobility Spectrometry Coupled with Two-Dimensional Tandem Mass Spectrometry, *J. Am. Soc. Mass Spectrom.* **2021**, DOI: 10.1021/jasms.1c00180
9. Schrader, R. L.; Marsh, B. M.; Cooks, R. G., Ion Focusing in a Funnel-like Device at Atmospheric Pressure using only DC-fields, *in preparation*

Cite this: *Analyst*, 2019, **144**, 4978

High-throughput, low-cost reaction screening using a modified 3D printer†

Robert L. Schrader,^a Stephen T. Ayrton,^a Andreas Kaerner^b and R. Graham Cooks  [✉]

We describe a reaction screening system, based on a 96-well array, and scaled to suit use on the individual scientist's bench. The system was built by modifying a desktop 3D printer and fitting it with a glass syringe and microtiter plate. The effects of experimental variables were characterized, and the performance of the system was optimized. Precise volumes of reaction mixtures (<3% CV) were dispensed into the 96-well array in ca. 40 minutes. The system was used to screen reagents and solvents for the *N*-alkylation, Katritzky trans-amination, and Suzuki cross-coupling reactions. Product distributions derived from electrospray mass spectra and represented as heat maps facilitated recognition of optimum conditions. Screening of 96 reaction mixtures was completed in the modest time of approximately 105 minutes (~65 seconds per reaction mixture). The system is constructed from open-source software and inexpensive 3D printer hardware.

Received 30th April 2019,
Accepted 15th July 2019

DOI: 10.1039/c9an00785g

rsc.li/analyst

Introduction

The combination of modern robotics and analytical instrumentation has allowed the rapid preparation and analysis of reaction mixtures. These experiments require less effort per reaction mixture than traditional synthetic and analytical methods.¹ High-throughput experimentation (HTE) utilizing mass spectrometry has been used in many areas such as biochemistry,² drug discovery,^{3,4} and catalysis.^{5,6} HTE has been applied to organic synthesis for the optimization of known reactions^{7–12} as well as the discovery of new ones.¹³

Chromatography-based high-throughput screening (HTS) systems in the microtiter format can have throughputs of 5–22 s per sample.¹⁴ The Agilent RapidFire system is a high throughput screening system coupled to SPE-MS with a sample throughput of ~8 s per sample.¹⁵ Other systems forgo chromatography, such as those using desorption electrospray ionization⁸ or acoustic droplet ejection¹⁶ and offer higher throughputs. Most such systems use mass spectrometry for analysis, although optical methods are also used.¹⁷ Here, we use an electrospray ionization (ESI) based method by applying a high voltage directly to the metal needle of a glass syringe for direct MS analysis of reaction mixtures. ESI-MS based systems are widely applicable to reaction screening, subject to

the limitations of ionization in which the product must be amenable to ionization by protonation, metal adduction, or derivatization. While the value of HTE is clear, the tools required to perform these experiments are expensive, making it difficult for most investigators to utilize.

Analytical chemistry has long embraced new technologies with examples from across the subject.^{18–22} Three-dimensional printing (3D printing) technology has developed greatly over the past few years and has made a significant impact in chemistry.^{23,24} The commercial 3D printer offers an easy-to-use platform for modification to perform tasks requiring simple robotics, for example a MALDI matrix application using a modified 3D printer.²⁵ Here we have utilized a Delta 3D printer, which utilizes three stepper motors at the base arranged in an equilateral triangle to move a hot extruder in the *x*, *y*, and *z* dimension. A typical Cartesian 3D printer uses stepper motors to directly control each axis. This hot extruder was replaced with a glass syringe whose plunger was controlled by an additional stepper motor (the “extruder” motor). Printers of this type are low cost and the additional parts necessary for modifications made can be purchased for an additional low cost. After calibration and optimization, this system was used to prepare 96-well microtiter plates with reaction being followed by analysis of products by mass spectrometry (Fig. 1).

Experimental

Commercial 3D printer modifications

The hotend assembly was removed from an assembled Anyubic Kossel 3D printer (Guandong, China) and replaced

^aPurdue University Department of Chemistry, West Lafayette, IN 47907, USA.
E-mail: cooks@purdue.edu

^bDiscovery Chemistry Research and Development, Eli Lilly and Company,
Lilly Corporate Center, Indianapolis, IN 46285, USA

† Electronic supplementary information (ESI) available. See DOI: 10.1039/c9an00785g



Fig. 1 Photographs of (a) the device in its home position in front of the mass spectrometer, (b) the custom syringe assembly moved to the spray position, and (c) a closeup of the syringe in the spray position showing the 90° bent capillary.

with a 250 μL Hamilton 750 series syringe with removable needle (Reno, NV). The needle length is 51 mm with an inner diameter of 0.15 mm and outer diameter of 0.72 mm. A short height NEMA 17 motor from OMC Corporation (Nanjing City, China) was held in place with a custom 3D printed bracket. The syringe was attached to a 125 mm beam from MakerBeam (Utrecht, Netherlands) with a custom 3D printed bracket and the syringe plunger controlled by the stepper motor through a timing belt. The stock 3D printer firmware was modified with a dummy temperature to allow movement of the extruder motor. All 3D printed pieces were designed in-house with Autodesk Inventor (San Rafael, CA), converted to STL, and 3D-printed using a Mendelmax 3 (Makers Tool Works, Oklahoma City, OK) with polylactic acid/polyhydroxyalkanoate (PLA/PHA) filament (ColorFabb, Belfeld, Netherlands). Additional information is included in the ESI.†

The custom bed was 3D printed with pre-defined holes to place two 96-well plates conforming to ANSI SLAS Standards 1 to 4–2004 with outer dimensions of approximately 127 by 85 mm. Additional holes allow for 20 mL vials and 4 mL vials containing wash solvent or reagent vials for well plate preparation. The x , y , z coordinates of each well was determined and controlled with G-code instructions.

Mass spectrometry

All mass spectrometry measurements were made with a Thermo-Fisher LTQ XL-Orbitrap or LTQ MS (San Jose, CA). An Arduino Uno (Adafruit, New York, NY) was used to supply a contact closure signal to the mass spectrometer by contact with a mechanical endstop (Bigtree Technology, Shenzhen City, China) upon reaching the spray position. The endstop was supported by metal beams (Makerbeam) and 3D printed brackets. Electrospray was generated directly from the syringe needle by applying high voltage (5 kV) to the needle. The stan-

dard inlet was replaced with an extended capillary bent 90° such that it was coaxial with the syringe needle in the spray position. Parameters for the MS were: spray voltage 4.5 kV, capillary voltage 15 V, tube lens 65 V, and capillary temperature 150 °C and a mass range of m/z 50–700.

Data analysis

Individual wells were saved as individual '.RAW' files by the instrument and were converted to the open-source '.mzXML' format using MSConvert.²⁶ Individual '.mzXML' files were imported into MATLAB (The MathWorks, Inc., Natick, MA) with the Bioinformatics toolbox. Using a user-supplied table of starting material and product m/z values, mass spectra in which one of these supplied m/z values was not the base peak were automatically removed. This serves to remove both scans in which noise was a significant portion of the spectrum and those in which no data was collected such that only data representative of the sample well was included. Data from each well was normalized and then displayed as a heat map of intensities covering the entire 96-well plate.

Reagents and supplies

All chemicals were purchased from Sigma-Aldrich (St Louis, MO). HPLC grade methanol was purchased from Fisher Scientific (Hampton, NH). Microtiter plates were purchased from Greiner Bio-One (Kremsmünster, Austria).

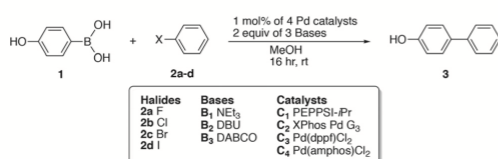
For the Suzuki reaction, solutions were prepared using 40 mM concentration of the halobenzene and 4-hydroxyphenylboronic acid, using 80 mM for the various bases, and 0.04–4 mM for the various catalysts. Aliquots of the appropriate reagents were robotically pipetted into each well and the microtiter plate was sealed with a silicone cover. The reaction mixtures were diluted 100 times in methanol for analysis manually.

fold. Since the signal intensity is over an order of magnitude larger than the carried over intensity, this suggests that carry-over is small, even when no wash step is done.

Screening of the Suzuki cross-coupling reaction

The use of metal catalyzed reactions to form C–C bonds has revolutionized synthetic organic chemistry. For example, the Suzuki cross-coupling forms a carbon–carbon single bond using an organoboron and a halide reagent.^{27,28} This reaction is especially important in the synthesis of drug targets.²⁹ This reaction has a strong dependence on experimental conditions, so establishing of a reactivity landscape for the reaction is very important,^{12,30} especially given its significance in medicinal chemistry.²⁹ Many combinations exist with various leaving groups, bases, solvents, and catalyst. In order to investigate the use of this device as a reaction screening tool, the Suzuki cross-coupling of 4-hydroxyphenylboronic acid (**1**) with various alkyl benzenes (**2a–d**) was studied using four pre-formed, air and moisture tolerant palladium catalysts (PEPPSI-*i*Pr, XPhosPd G3, Pd(dppf)Cl₂, and Pd(amphos)Cl₂) with triethylamine, DBU, and DABCO base (Scheme 1). After preparation, reaction mixtures were allowed to stand at room temperature for 16 hours.

The reactivity landscape of this reaction was tested *via* a base screen and catalyst loading screen (Fig. 3). These reac-



Scheme 1 Suzuki cross-coupling of 4-hydroxyphenylboronic acid (**1**) with various alkyl benzenes (**2a–d**) to form 4-phenylphenol (**3**).

tions were performed in the open air, but all catalysts used are relatively air and moisture stable. In all cases, the iodobenzene showed the greatest reactivity while the Pd(dppf)Cl₂ and Pd(amphos)Cl₂ catalysts gave the greatest yields. Fig. 3b shows a screen of catalyst loading using triethylamine base. As expected, increasing catalyst loading percentage increases reactivity. Increased catalyst loading percentages increased yield, but it is important to find optimal catalyst loading as this increases cost.

Previous DESI high-throughput screening work using a similar Suzuki coupling^{7,8} exclusively utilized the XPhosPd G3 catalyst. Other studies have shown the XPhosPd G3 catalyst to work very well, even for difficult substrates.¹² This work was done at room temperature and the differences in observed reactivity between those studies and this one is most likely due to differences in temperature.

Amine alkylation reaction and automated MS/MS acquisition

Amine alkylation reactions were also studied using this system. The carbon–nitrogen bond is a key step for the formation of a large number of compounds.³¹ The direct nucleophilic alkylation can be problematic because it forms both single and double alkylation products.⁸ The reaction of benzylamine (**4**) and benzyl bromide (**A**) (Scheme 2) shows a large conversion to the double alkylation product.

Heatmaps for the single alkylation product is shown in Fig. 4a and the double alkylation product in Fig. 4b. Some reaction is seen in other solvents, but this reaction proceeds the best in the polar, aprotic solvent acetonitrile. Benzyl bromide showed far greater reactivity than benzyl chloride, given that bromide is a stronger leaving group than chloride. Similarly, no reactivity was observed for bromoethylbenzene (**B**) due to the lack of stability of its carbocation when compared to the benzyl halides. Similar trends were seen for the reaction of the other amine reagents (**5–7**) shown in the ESI (Fig. S3 and S4†). Because the reaction mixtures were diluted

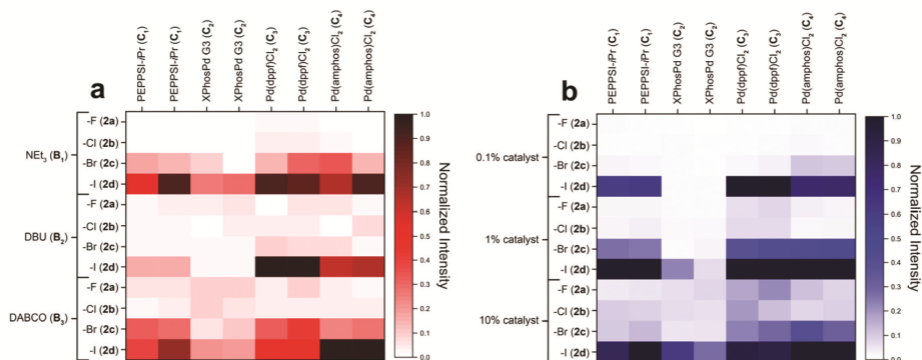


Fig. 3 Heatmap of normalized intensity of the product ion (observed as $[M - H]^+$ at m/z 169) for various halides, (a) 2 equivalents base and 1% catalyst, and (b) various catalyst loadings with 2 equivalents of trimethylamine. Each reaction mixture is run in duplicate with each adjacent well containing the same reaction mixture.

For the *N*-alkylation, both the amine and halide were prepared using 10 mM in methanol, ethanol, acetonitrile, and dioxane. The reagents were pipetted manually into each well of the microtiter plate. The reaction mixtures were diluted 1000 times in methanol for analysis.

For the Katritzky transamination, both the 2,4,6-triphenylpyrilium tetrafluoroborate and five substituted anilines were prepared using 20 mM in acetonitrile. The prepared solutions were pipetted into a microtiter plate manually in quadruplicate. The reaction mixtures were diluted 1000 times in acetonitrile for analysis.

Results and discussion

Liquid handling

The extruder motor was used to control the plunger of a glass syringe. The ability of the device to deliver accurate volumes is directly related to the motion of the stepper motor. The device was calibrated by measuring the volume of water delivered for a specific command distance, for example a 20 unit G-code command resulted in a delivered volume of 90.33 μL . Using

the resulting linear calibration, the volume delivery was tested at four different volumes in triplicate (Table 1).

An Eppendorf manual autopipette delivering 100 μL using a 20–200 μL tip has a systematic error of $\pm 1.0 \mu\text{L}$, slightly greater than the observed error using the automated device. This demonstrates that a modified 3D printer can be used to prepare 96-well plates from prepared stock solutions with reliable accuracy.

A program to fill microtiter plates with the appropriate solutions from stock solution was written using G-code. The well plate design for the Suzuki base screening experiment is shown in Fig. 2 and the catalyst loading experiment is shown in Fig. S1.† These plate configurations were completed in approximately forty minutes and require no operator intervention. Reagents were stored in 4 mL vials in the pre-cut holes. The syringe drew 200 μL of reagent and deposited 25 μL of reagent per well. The syringe was then washed with methanol solvent before a new reagent was dispensed.

Carryover

A concern when using the same syringe for repeated sample injection is carryover between samples. In order to investigate this effect, a well plate was filled with alternating wells of 1 μM rhodamine B in methanol and pure methanol. For the first 16 wells, the syringe was washed twice with methanol between injection. For the second 16 wells, the syringe was washed only once with methanol. For the final 16 wells, the syringe was not washed between each injection. The resulting heatmap is shown in Fig. S2.† No change in ion intensity at m/z 443 was observed in the blank wells between one wash and two. When no wash step was performed between wells, the ion intensity observed at m/z 443 in the blank wells was increased by six-

Table 1 Accuracy in volume delivery of syringe driven by 3D printer extruder motor

Desired volume	Actual volume delivered	Percent error
50 μL	$51.3 \pm 0.3 \mu\text{L}$	2.70%
100 μL	$99.3 \pm 0.4 \mu\text{L}$	−0.75%
150 μL	$149.7 \pm 0.5 \mu\text{L}$	−0.18%
200 μL	$200.7 \pm 0.7 \mu\text{L}$	0.37%

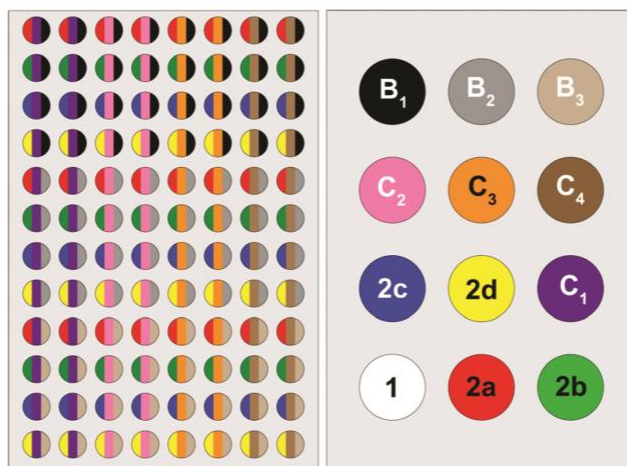
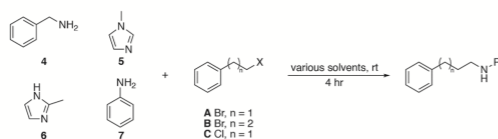


Fig. 2 Microtiter plate for catalyst loading experiments was pipetted using this pattern in which each reagent was pipetted directly into the appropriate well. Reagents were stored in 4 mL vials and each syringe addition could fill 8 wells. Syringe was only washed when the reagent was changed. The full well plate was analyzed in approximately 40 minutes.

Paper



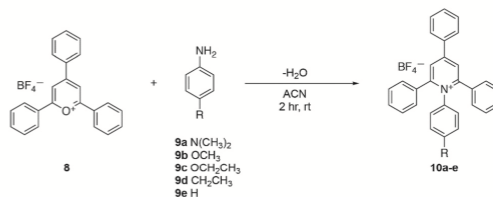
Scheme 2 Alkylation of various amines (4–7) by a halide (A–C) to form a single alkylation product and can potentially form a double alkylation product.

in methanol prior to analysis, solvent effects on ionization efficiency of the products should be negligible.

The data acquisition in these experiments was controlled through Thermo-Fisher XCalibur software, which allowed for the automated acquisition of MS/MS. This can either be done by pre-selecting expected product ion masses or can be done in a data-dependent fashion. In the case of the amine alkylation, MS/MS data was collected for each of the expected alkylation products, as exemplified in Fig. 5. The spectra obtained for these compounds confirm the identity of the products as they agree with reported literature spectra.⁸

Katritzky transamination

The Katritzky transamination reaction involves reaction of a pyrylium heterocycle (8) with a *para*-substituted aniline (9a–e) to form the pyridinium salt (Scheme 3). The reactions were performed in acetonitrile and run in quadruplicate. The resulting MS ion intensity were used to calculate a ratio of product to starting material without correction for ionization efficiencies. A heatmap of the resulting ratios is shown in Fig. 6a.



Scheme 3 Reaction of 2,4,6-triphenylpyrylium tetrafluoroborate (8) with various *para*-substituted anilines (9a–e) to form a pyridinium product (10a–e).

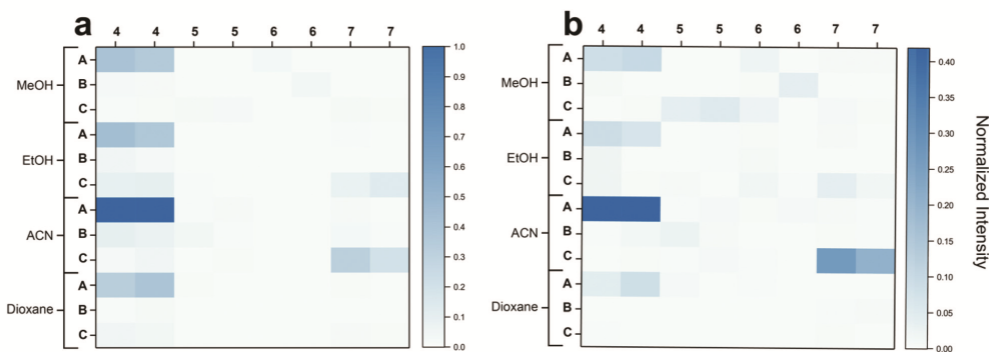


Fig. 4 Reaction of benzylamine (4) and benzyl bromide (A) is observed to be fastest in acetonitrile. (a) The single alkylation product (4 + A) is observed as well as (b) the double alkylation product (4 + 2A).

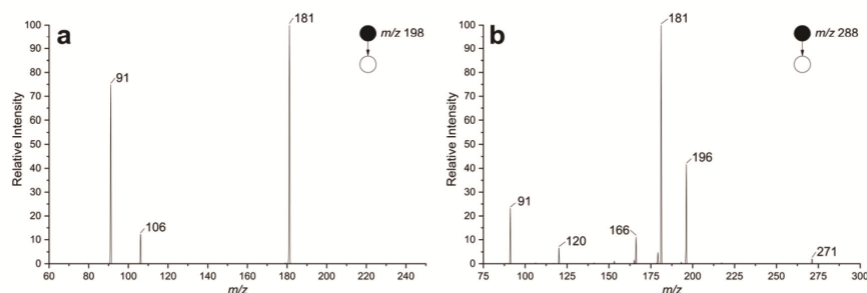


Fig. 5 MS/MS data is acquired automatically for each well to confirm the identity of the desired product. (a) MS/MS fragmentation of the single alkylation product and (b) MS/MS fragmentation of the double alkylation product is shown for the reaction of benzylamine and benzyl bromide.

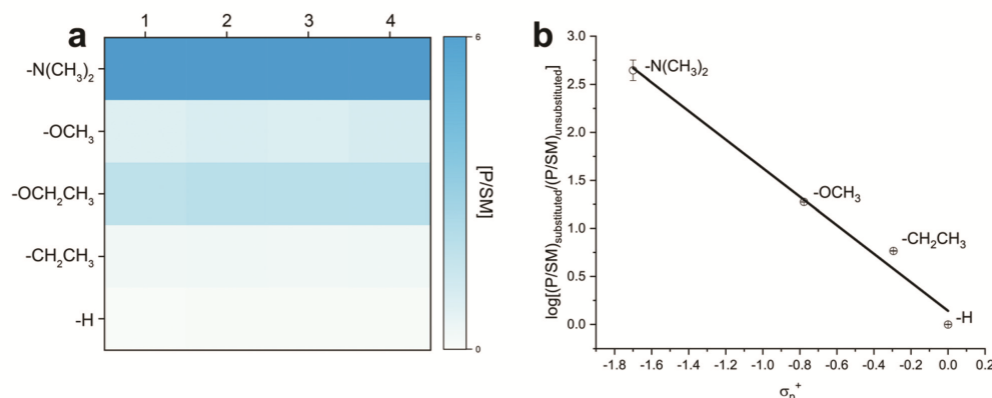


Fig. 6 (a) Heatmap of product to starting material ratios for each *para*-substituted aniline for the Katritzky transamination reaction run in acetonitrile and (b) the resulting Hammett plot which shows a log-linear relationship.

This data can also be displayed as a Hammett plot, showing the reaction yield of the substituted cases *versus* the unsubstituted plotted *versus* the substituent constant σ_p ^{32–34} (Fig. 6b). The slope of the resulting plot shows the effect of the electronic nature of the substituents on the reaction kinetics. When conjugation exists between the substituents and the cationic reaction center, such as with anilines, classic Hammett σ_p values result in poor correlation,³³ which can be seen in Fig. S5†. The correlation can be greatly improved using electrophilic substituent constants σ_p^+ (Fig. 6b).³⁵ This correlation is much more strongly linear when compared to standard Hammett substituent constants. This is evidence that the reaction site is in direct resonance with the *para* substituent, which offers greater stabilization.³⁶

Throughput for the analysis is approximately 65 seconds per reaction mixture, or 105 minutes per 96-well plate. The spray and data acquisition time were 30 seconds per reaction mixture. The remaining time (~35 seconds per reaction mixture) is for getting an aliquot of the sample, movement, and washing of the syringe. This is much slower than other screening systems, such as LC-MS¹⁴ (5–22 s per sample), RapidFireTM¹⁵ (8 s per sample), DESI⁸ (1 s per sample), or the Echo-MS system¹⁶ (1 s per sample), but the cost is far lower. As such, it might be cost effective for an individual investigator to screen reactions this way, performing many more than could be done manually in the same time. A low cost portable mass spectrometer would complement this screening system.³⁷

Although it is not possible to determine *a priori* when this might occur, electrospray ionization can occasionally drive unexpected reaction due to gas-phase pathways.^{38–40} In these experiments, we are simply using mass spectrometry as it has been traditionally used since the 1990s to monitor reaction products.⁴¹ The conditions we use are generally believed not to cause reactions. We have shown that we are indeed observing the bulk phase reaction by performing experiments on reaction mixtures directly after mixing and observing that no reaction products occur (Fig. S7†).

Conclusions

Most reaction screening systems are large-scale and expensive which limits availability to the individual investigator. By modifying a 3D printer to replace the extruder with a glass syringe, low-cost hardware and open-source software can be used for preparation of 96-well microtiter plates and subsequent screening of reaction mixtures. This allows for the easy and cheap investigation of reactions in which the reactivity landscape greatly depends on the reaction conditions and seemingly endless combinations of solvent, catalyst, and base are available. Automated MS/MS capabilities aid in identification of product as well as potential byproducts. Automated preparation of well plates can be done in approximately 40 minutes and the MS analysis time is approximately 105 minutes on a system that is home-built and low-cost.

Conflicts of interest

There are no conflicts to declare.

Acknowledgements

We acknowledge support from the Eli Lilly LRAP (17045108) program.

References

- 1 M. Shevlin, *ACS Med. Chem. Lett.*, 2017, **8**, 601–607.
- 2 T. Peng, G. Nagy, J. C. Trinidad, J. M. Jackson and N. L. B. Pohl, *ChemBioChem*, 2017, **18**, 2306–2311.
- 3 R. Macarron, M. N. Banks, D. Bojanic, D. J. Burns, D. A. Cirovic, T. Garyantes, D. V. S. Green, R. P. Hertzberg, W. P. Janzen, J. W. Paslay, U. Schopfer and

- G. S. Sittampalam, *Nat. Rev. Drug Discovery*, 2011, **10**, 188.
- 4 T. P. Roddy, C. R. Horvath, S. J. Stout, K. L. Kenney, P.-I. Ho, J.-H. Zhang, C. Vickers, V. Kaushik, B. Hubbard and Y. K. Wang, *Anal. Chem.*, 2007, **79**, 8207–8213.
- 5 M. Renom-Carrasco and L. Lefort, *Chem. Soc. Rev.*, 2018, **47**, 5038–5060.
- 6 S. M. Senkan, *Nature*, 1998, **394**, 350.
- 7 Z. Jaman, A. Mufti, S. Sah, L. Avramova and D. H. Thompson, *Chem. – Eur. J.*, 2018, **24**, 9546–9554.
- 8 M. Wleklinski, B. P. Loren, C. R. Ferreira, Z. Jaman, L. Avramova, T. J. P. Sobreira, D. H. Thompson and R. G. Cooks, *Chem. Sci.*, 2018, **9**, 1647–1653.
- 9 Z. Jaman, T. J. P. Sobreira, A. Mufti, C. R. Ferreira, R. G. Cooks and D. H. Thompson, *Org. Process Res. Dev.*, 2019, **23**, 334–341.
- 10 S. D. Dreher, P. G. Dormer, D. L. Sandrock and G. A. Molander, *J. Am. Chem. Soc.*, 2008, **130**, 9257–9259.
- 11 S. Lin, S. Dikler, W. D. Blincoe, R. D. Ferguson, R. P. Sheridan, Z. Peng, D. V. Conway, K. Zawatzky, H. Wang, T. Cernak, I. W. Davies, D. A. DiRocco, H. Sheng, C. J. Welch and S. D. Dreher, *Science*, 2018, **361**, eaar6236.
- 12 D. Perera, J. W. Tucker, S. Brahmabhatt, C. J. Helal, A. Chong, W. Farrell, P. Richardson and N. W. Sach, *Science*, 2018, **359**, 429.
- 13 K. Troshin and J. F. Hartwig, *Science*, 2017, **357**, 175.
- 14 A. Buitrago Santanilla, E. L. Regalado, T. Pereira, M. Shevlin, K. Bateman, L.-C. Campeau, J. Schneeweis, S. Berritt, Z.-C. Shi, P. Nantermet, Y. Liu, R. Helmy, C. J. Welch, P. Vachal, I. W. Davies, T. Cernak and S. D. Dreher, *Science*, 2015, **347**, 49.
- 15 M. Leveridge, R. Buxton, A. Argyrou, P. Francis, B. Leavens, A. West, M. Rees, P. Hardwicke, A. Bridges, S. Ratcliffe and C.-w. Chung, *J. Biomol. Screening*, 2013, **19**, 278–286.
- 16 I. Sinclair, R. Stearns, S. Pringle, J. Wingfield, S. Datwani, E. Hall, L. Ghislain, L. Majlof and M. Bachman, *J. Lab. Autom.*, 2015, **21**, 19–26.
- 17 D. F. Kennedy, B. A. Messerle and S. L. Rumble, *New J. Chem.*, 2009, **33**, 818–824.
- 18 E. A. Dennis, S. J. Ray, C. G. Enke, A. W. Gundlach-Graham, C. J. Barinaga, D. W. Koppenaal and G. M. Hieftje, *J. Am. Soc. Mass Spectrom.*, 2016, **27**, 371–379.
- 19 A. J. Schwartz, J. T. Shelley, C. L. Walton, K. L. Williams and G. M. Hieftje, *Chem. Sci.*, 2016, **7**, 6440–6449.
- 20 C. M. Nichols, J. C. May, S. D. Sherrod and J. A. McLean, *Analyst*, 2018, **143**, 1556–1559.
- 21 M. S. Westphall, K. Jorabchi and L. M. Smith, *Anal. Chem.*, 2008, **80**, 5847–5853.
- 22 E. Gard, J. E. Mayer, B. D. Morrical, T. Dienes, D. P. Ferguson and K. A. Prather, *Anal. Chem.*, 1997, **69**, 4083–4091.
- 23 B. Gross, S. Y. Lockwood and D. M. Spence, *Anal. Chem.*, 2017, **89**, 57–70.
- 24 A. J. Capel, R. P. Rimington, M. P. Lewis and S. D. R. Christie, *Nat. Rev. Chem.*, 2018, **2**, 422–436.
- 25 L. H. Tucker, A. Conde-González, D. Cobice, G. R. Hamm, R. J. A. Goodwin, C. J. Campbell, D. J. Clarke and C. L. Mackay, *Anal. Chem.*, 2018, **90**, 8742–8749.
- 26 M. C. Chambers, B. Maclean, R. Burke, D. Amodei, D. L. Ruderman, S. Neumann, L. Gatto, B. Fischer, B. Pratt, J. Egerton, K. Hoff, D. Kessner, N. Tasman, N. Shulman, B. Frewen, T. A. Baker, M.-Y. Brusniak, C. Paulse, D. Creasy, L. Flashner, K. Kani, C. Moulding, S. L. Seymour, L. M. Nuwaysir, B. Lefebvre, F. Kuhlmann, J. Roark, P. Rainer, S. Detlev, T. Hemenway, A. Huhmer, J. Langridge, B. Connolly, T. Chadick, K. Holly, J. Eckels, E. W. Deutsch, R. L. Moritz, J. E. Katz, D. B. Agus, M. MacCoss, D. L. Tabb and P. Mallick, *Nat. Biotechnol.*, 2012, **30**, 918.
- 27 A. F. Litke, C. Dai and G. C. Fu, *J. Am. Chem. Soc.*, 2000, **122**, 4020–4028.
- 28 N. Miyaura and A. Suzuki, *Chem. Rev.*, 1995, **95**, 2457–2483.
- 29 D. G. Brown and J. Boström, *J. Med. Chem.*, 2016, **59**, 4443–4458.
- 30 B. J. Reizman, Y.-M. Wang, S. L. Buchwald and K. F. Jensen, *React. Chem. Eng.*, 2016, **1**, 658–666.
- 31 S. Elangovan, J. Neumann, J.-B. Sortais, K. Junge, C. Darcel and M. Beller, *Nat. Commun.*, 2016, **7**, 12641.
- 32 L. P. Hammett, *Trans. Faraday Soc.*, 1938, **34**, 156–165.
- 33 C. Hansch, A. Leo and R. W. Taft, *Chem. Rev.*, 1991, **91**, 165–195.
- 34 R. M. Bain, C. J. Pulliam, X. Yan, K. F. Moore, T. Müller and R. G. Cooks, *J. Chem. Educ.*, 2014, **91**, 1985–1989.
- 35 H. C. Brown and Y. Okamoto, *J. Am. Chem. Soc.*, 1958, **80**, 4979–4987.
- 36 X. Yan, R. Augusti, X. Li and R. G. Cooks, *ChemPlusChem*, 2013, **78**, 1142–1148.
- 37 D. T. Snyder, C. J. Pulliam, Z. Ouyang and R. G. Cooks, *Anal. Chem.*, 2016, **88**, 2–29.
- 38 M. I. Jacobs, J. F. Davies, L. Lee, R. D. Davis, F. Houle and K. R. Wilson, *Anal. Chem.*, 2017, **89**, 12511–12519.
- 39 M. I. Jacobs, R. D. Davis, R. J. Rapf and K. R. Wilson, *J. Am. Soc. Mass Spectrom.*, 2019, **30**, 339–343.
- 40 A. Gallo, A. S. F. Farinha, M. Dinis, A.-H. Emwas, A. Santana, R. J. Nielsen, W. A. Goddard and H. Mishra, *Chem. Sci.*, 2019, **10**, 2566–2577.
- 41 M. N. Eberlin, *Eur. J. Mass Spectrom.*, 2007, **13**, 19–28.

Fourier Transform-Ion Mobility Linear Ion Trap Mass Spectrometer Using Frequency Encoding for Recognition of Related Compounds in a Single Acquisition

Robert L. Schrader, Brett M. Marsh, and R. Graham Cooks*



Cite This: *Anal. Chem.* 2020, 92, 5107–5115



Read Online

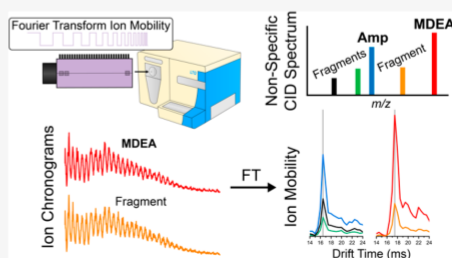
ACCESS |

Metrics & More

Article Recommendations

Supporting Information

ABSTRACT: Fourier transform-ion mobility spectrometry is implemented by coupling a 3D-printed drift tube ion mobility spectrometer, operated at atmospheric pressure, to a linear ion trap mass spectrometer. FT-IMS separations are demonstrated for tetraalkylammonium salts, explosives, fentanyl, and amphetamines. Mobility resolving powers of up to 17 are measured for the tetraalkylammonium cations. When ions are fragmented in the FT-IMS mode, the product ions maintain the frequency and amplitude relationships established during the mobility measurement. Therefore, precursors and product ion relationships can be identified through the mobility information. Using in-source activation for nonspecific fragmentation of all precursors, functional group families of precursors and product ions are identified in a single acquisition. The identity of the precursor ion is not known a priori, but the m/z values for both precursors and product ions are measured.



Ion mobility has been used as a standalone detector and coupled with mass spectrometry for the detection of drugs,^{1–3} explosives,^{4–6} biological materials,^{7,8} among others. Ion mobility separates ions in space or time based on the size-to-charge ratio,⁹ as opposed to mass spectrometry which separates based on the mass-to-charge ratio. Mobility separation can be accomplished with many instrumental configurations, such as drift tubes,^{9,10} high-field asymmetric waveform spectrometers,¹¹ traveling wave devices,¹² trapped ion mobility spectrometers,¹³ and structures for lossless ion manipulation.¹⁴

The simplest of these spectrometers is the drift tube in which ions are pulsed into the drift region where they traverse a uniform electric field and are impeded by collisions to a degree that depends on their collision cross section.^{9,15} Faraday cup detection completes the stand-alone drift tube device.^{16,17} Drift tubes can also be coupled to mass spectrometers. Instruments with a single entrance gate coupled to a fast mass analyzer, such as a time-of-flight instrument, must have a mass spectrometry sampling rate sufficient to extract mobility information in the millisecond regime from a single ion injection event. Quadrupole mass filters have also been used as mass analyzers and detectors for drift tube ion mobility devices.³ The quadrupole mass filter can be used either to analyze all ions in a transmission mode or in a mass-selective mode to detect ions of a single m/z . Triple quadrupoles offer the addition of tandem mass spectrometry capabilities.^{5,18,19} Slow mass analyzers, such as quadrupole ion

traps and Orbitraps, are unable to sample all of the mobility information from a single injection of ions. The mass scan in a quadrupole ion trap occurs over 30–85 ms, which is much slower than in time-of-flight instruments.²⁰ One approach to overcome this is to sample a mobility-selected packet of ions by scanning the delay between the opening of the first ion gate and a second ion gate at the exit of the drift cell. The ion mobility spectrum can be reconstructed from the MS intensity at each sampling point.^{21,22} In this mode of operation, greater than 99% of the ions generated at the ion source are not sampled at the mass spectrometer. The equations relating resolving power and signal-to-noise ratio in drift tube ion mobility have been published previously.²³

Fourier transforms are utilized in mass spectrometry techniques such as Fourier transform-ion cyclotron resonance,²⁴ Orbitraps,^{25,26} in select quadrupole ion trap^{27,28} and time-of-flight experiments.²⁹ Fourier transform-ion mobility (FT-IMS) is a recently reintroduced technique that has been used to increase the duty cycle when coupling drift tube ion mobility with ion traps^{30,31} and Orbitraps.^{32,33} The FT-IMS method increases the duty cycle to 25%, which results in

Received: December 4, 2019

Accepted: February 25, 2020

Published: March 3, 2020



ACS Publications

© 2020 American Chemical Society

<https://dx.doi.org/10.1021/acs.analchem.9b05507>
Anal. Chem. 2020, 92, 5107–5115

breadboard and as such allowed for standard header pins to be used to supply voltages to the device. A schematic of the device is provided in Figure 1a. Note that the first two and the final two drift electrodes were used as ion gates. Unlike some other ion mobility systems,^{23,30} there is no ion desolvation region prior to the entrance ion gate as the plastic construction could not be heated.

Electronics. High-voltage DC potentials were applied to the drift region through a custom voltage divider circuit built with a solderable breadboard (Mouser Electronics, Mansfield, TX) and using 29 resistors, each 1 M Ω . Electrical contact was made by inserting header pins from the breadboard into holes in the electrodes. Entrance and exit ion gates were created with four steel mesh screens (40 mesh, 66% transmission, E-Fab, Santa Clara, CA) placed on the 1st, 2nd, 30th, and 31st drift electrode. The switched potential on the 1st drift electrode and 31st drift electrode was applied using a Behlke GHTS 60A (BillERICA, MA) high-voltage switch and a Directed Energy Inc. (DEI) PVX-4140 pulse generator (Fort Collins, CO). High voltage for the focusing electrode, both potentials for the Behlke switch, and the upper drift potential were supplied from a custom high-voltage power supply. High voltage for the lower drift potential and DEI switch were supplied by a Spectrum Solutions (Russellton, PA) TD-500 power supply. The square wave input signal for both high-voltage switches was supplied by a Keysight 33600A waveform generator (Santa Rosa, CA). High-voltage parameters for each electrode are given in Table 1.

Table 1. Operating Parameters for the Bipolar Ion Mobility Spectrometer

item	parameter
nanospray voltage	± 4500 – 5500 V
focusing electrode	± 3000 V
gate 1 electrode (high/low)	$\pm 2500/2375$ V
drift high	± 2400 V
drift low	± 200 V
gate 2 electrode (high/low)	$\pm 325/75$ V
ion gate frequency sweep	5–2005, 5–3005, 5–7005 Hz

Mass Spectrometry. Borosilicate glass capillaries (i.d. 0.86 cm, o.d. 1.5 cm, 10 cm length) were purchased from Sutter Instruments (Navajo, CA) and pulled to an approximate 5 μ m tip diameter with a P-97 Flaming/Brown tip puller (Sutter Instruments). The pulled capillaries were fitted in a Warner Instruments (Hamden, CT) E series electrode holder fitted with a 0.127 mm diameter silver wire (Alfa Aesar, Ward Hill, MA, USA), and high voltage (4.5–5.5 kV) was applied to the holder. A Thermo Finnigan LTQ (San Jose, CA) was used for all experiments. The nanoelectrospray capillaries were placed approximately 1–2 mm from the first steel mesh. An Arduino Uno microcontroller (Arduino, Turin, Italy) with a mechanical switch was used to trigger the waveform generator and the LTQ sample acquisition simultaneously using the Arduino digital output pins and LTQ contact closure. The 3D-printed ion mobility device was placed approximately 1 mm in front of the mass spectrometer capillary inlet (Figure 1d). A 200 ms ion injection time (without automatic gain control) was used for all experiments, which corresponds to a scan time of approximately 240–280 ms, dependent on mass range. Capillary temperature, capillary voltage, and tube lens voltage were 200 $^{\circ}$ C, ± 15 V, and ± 65 V, respectively. For CID

experiments, a 100 ms injection time with an isolation window of m/z 100 and with the isolation mass being set at a value of mass-to-charge ratio that corresponded to the average of two adjacent TAA cations while a normalized collision energy of 40 was used. When source fragmentation was of interest for MS/MS experiments on drugs of abuse, a voltage of 30–50 V was applied. Ion chronograms for each ion of interest were generated using XCalibur (Thermo Fisher), and Fourier transforms were calculated using MATLAB (The MathWorks, Inc., Natick, MA).

Fourier Transform-Ion Mobility Operation. In the FT-IMS mode of operation, both ion gates were opened and closed simultaneously using a square wave with an initial frequency of 5 Hz and final frequency of 2005–7005 Hz with the adjustment in frequency occurring linearly over a period of 4 min (Figure 1b). The highest gating frequency that can be used is a function of the sampling rate of the mass analyzer as higher gating frequencies result in higher encoded frequencies. Waveforms were calculated in MATLAB and exported as “.csv” files to the waveform generator. Frequency encoding of FT-IMS has been described previously.^{32,46} Briefly, ions are transmitted when their drift time (t_d) corresponds to the gating frequency ($\nu = 1/t_d$). Therefore, by sweeping the gate frequency over a range of frequencies, the signal (S) will be

$$S(\nu)_{\max} = 0.5I_0 \text{ for } \nu = 0, 1/t_d, 2/t_d, 3/t_d, \dots$$

$$S(\nu)_{\min} = 0 \text{ for } \nu = 0, 1/2t_d, 3/2t_d, 5/2t_d, \dots$$

at frequency ν where I_0 is the ion intensity without ion gating. For each ion, the resulting ion chronogram can be Fourier transformed to give the ion arrival frequency. The total signal versus time, the total ion chronogram, represents the raw data obtained over the course of the experiment. The ion mobility spectrum can then be determined by dividing the signal by the sweep rate in Hz/s. The steps connecting the ion chronogram to the ion mobility spectrum are shown in Figure 1c.

RESULTS AND DISCUSSION

Characterization of Plastic IMS in Fourier Transform Mode. Previous experiments using the plastic, dual-gated ion mobility device have shown good resolution but low efficiency using the second ion gate as a mobility selection window.²¹ In order to compare this mode of operation with Fourier transform-ion mobility, a seven tetraalkylammonium salt mixture (C_2 – C_8) was ionized by nanospray with the emitter placed inside the focusing electrode and the drift cell placed directly in front of the mass spectrometry capillary inlet. Three different waveforms were used in turn, each 4 min in length: 5–2005, 5–3005, and 5–7005 Hz. Ion mobility spectra for the TAA mixture are shown in Figure 2a. The signal intensity of the C_2 TAA is small when compared with the other TAAs, and it is overshadowed when plotted on the same scale. A plot showing only the C_2 TAA for each frequency sweep is given in Figure S1. In all cases, for higher sweep rates, higher arrival frequencies were observed, as shown for the C_6 TAA cation (Figure 2b). The arrival frequency for ions of higher mobility (lower drift time) is lower than that of an ion with lower mobility (Figure 2c). Resolving power was calculated by fitting each peak (e.g., in Figure 2a) to a Gaussian function, and the resolving power is $R_p = t_d/\text{fwhm}$, where the fwhm is 2.353σ , where σ is obtained from the Gaussian fitting. This treatment is only valid for Gaussian peaks, which may not be true for the TAA cations given the small number of data points making up

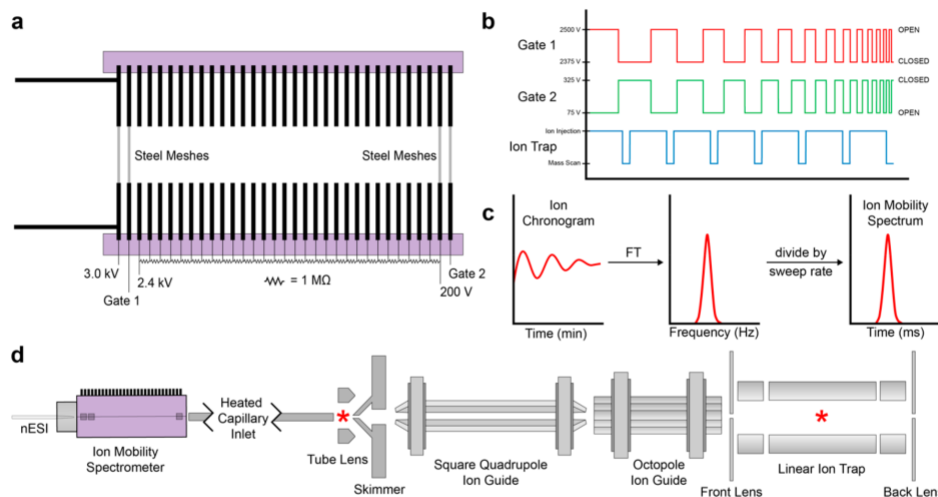


Figure 1. (a) Schematic of the 3D-printed ion mobility device with ion gating performed by applying square waveforms to two sets of steel meshes at each end of the 31-drift lens spectrometer. Cylindrical extrusion can be seen on the first (focusing) electrode. Steel meshes are placed directly onto the 3D-printed electrodes. (b) Sweep voltages used to simultaneously open and close the gates with linearly increasing frequency. (c) Fourier transform of the ion chronogram gives the ion frequency distribution, which is converted into arrival time, i.e., the ion mobility spectrum, by division by the sweep rate. (d) Ion mobility spectrometer is placed directly in front of the mass spectrometer capillary inlet. Fragmentation (denoted by a red asterisk) can be made in either the source region or the ion trap.

improved data acquisition times and increased instrumental sensitivity. Alternatively, an increase in duty cycle can also be accomplished with the Hadamard transformation.^{34–36} The Hadamard transform has also been applied to time-of-flight mass spectrometry.^{37,38}

In IMS-TOF experiments, ions can be fragmented following the drift tube separation and prior to mass analysis and the resulting product ions will maintain the precursor ion arrival time.^{39–41} It has been observed that ions that are fragmented in the ion trap maintain the arrival frequency encoded into the precursor ions in FT-IMS experiments done using a linear ion trap.³¹ In this study we use this knowledge in order to fragment all ions via in-source fragmentation and then identify families of precursors and product ions from the mobility information.

Ion mobility spectrometers have been fabricated using several nontraditional means including resistive glass,⁴² printed circuit boards,^{14,43,44} and metal-coated polymers.⁴⁵ A 3D-printed ion mobility spectrometer has recently been described as both a standalone device¹⁷ as well as coupled to a mass spectrometer.²¹ Resolving powers achieved for the standalone device were about 50, and when coupled to the mass spectrometer they were approximately 45. This ion mobility device was fabricated using polylactic acid/polyhydroxyalkanoate for the housing and conductive polyethylene terephthalate glycol-modified polymer with multiwalled carbon nanotubes for the electrodes. This device was used here to perform FT-IMS experiments and to establish a methodology to obtain MS/MS information from all ions using a single FT-IMS experiment.

EXPERIMENTAL SECTION

Chemicals. Tetraalkylammonium (TAA) bromide salts (C_2 – C_8) were purchased from Sigma-Aldrich (St. Louis, MO). TAAs were prepared in 100 μ M solutions in acetonitrile (Fisher Scientific, Hampton, NH). Amphetamine, 3,4-methylenedioxymethamphetamine (MDEA), acetyl norfentanyl oxalate, acetyl fentanyl, 4-fluoroisobutyrylfentanyl, trinitroglycerin (TNG), and HMX were purchased from Cerilliant (Round Rock, TX). Amphetamine solutions were diluted to 10 ppm from standards in methanol (Fisher Scientific) and 0.1% formic acid (Sigma-Aldrich). Fentanyl solutions were diluted to 25 ppm in methanol/0.1% formic acid. Explosives solutions were diluted to 10 ppm in acetonitrile (Fisher Scientific). TAA bromide salts were observed as the positively charged cations, and the drugs of abuse were observed as the protonated molecules. Explosives were observed as negatively charged adducts with chloride and nitrate.

3D-Printed Ion Mobility Spectrometer. The 3D-printed ion mobility spectrometer has been described in detail previously.^{17,21} Briefly, polyethylene terephthalate glycol (PETG)-modified polymer filament containing multiwalled carbon nanotubes (3DXTech, MI) was used to construct 1 focusing electrode and 31 drift electrodes. The drift electrode apertures were 7 mm in diameter. The first (focusing) electrode incorporated a 30 mm cylindrical extrusion prior to the lens structure used to confine the electrospray plume. The nonconductive housing was printed in two identical pieces from nonconductive polylactic acid/polyhydroxyalkanoate (PLA/PHA) filament (ColorFabb, Belfeld, Netherlands). The housing with overall dimensions of approximately 46 × 66 × 83 mm was fabricated such that the slots for the individual electrodes had a pitch of 2.54 mm. This distance was chosen as it is the standard distance between pins of a

<https://dx.doi.org/10.1021/acs.analchem.9b05507>
Anal. Chem. 2020, 92, 5107–5115

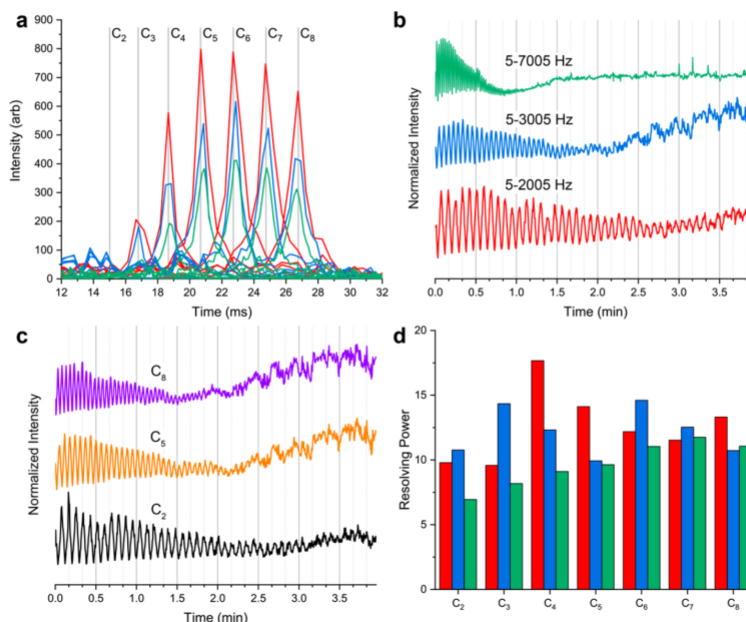


Figure 2. Ion mobility spectra for TAA cation mixture (C_2 – C_8) recorded using gate frequency sweeps: 5–2005 Hz (red), 5–3005 Hz (blue), and 5–7005 Hz (green). (b) Ion chronograms for the C_6 TAA for each frequency sweep show an increase in arrival frequency with sweep rate. (c) Ion chronograms for the C_2 , C_5 , and C_8 TAA cation for the 5–3005 Hz frequency sweep shows an increase in arrival frequency for ions with lower mobility. (d) Calculated resolving power for each TAA cation for each frequency sweep showing a decrease in resolving power at faster sweep rates.

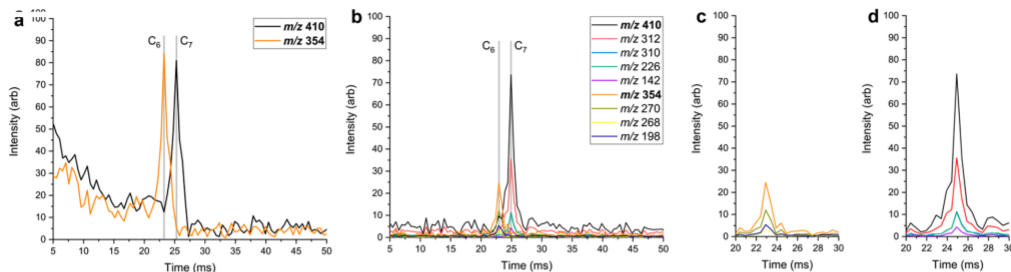


Figure 3. (a) Isolation using a m/z 100 window allows isolation of the C_6 and C_7 TAA cation in the ion trap. (b) Excitation occurs at a secular frequency corresponding to the average mass. Fragment ions (generated in the ion trap) of each TAA cation have the same drift time as the precursor ion, as can be seen in the ion mobility spectrum. (c) Ion mobility spectrum of only the C_6 precursor and product ions showing that all peaks have the same drift time. (d) Ion mobility spectrum of only the C_7 precursor and product ions showing again that both peaks have the same drift time.

the peak. While the peaks in the observed spectrum are nonideal, it is a valuable metric for comparisons. A simulation study based on a PCB ion mobility device has been done to optimize Gaussian peak response.⁴³ For higher gate sweep frequencies, i.e., a higher sweep rate, both the absolute signal intensity as well as the resolving power were decreased.

The maximum resolving power achieved when the plastic IMS device was operated using the second gate as a mobility window selector was approximately 45,²¹ whereas the maximum resolving power observed using the Fourier transform mode was 17. A greater resolving power was

reported using the FT-IMS mode of operation on a commercial Exellims ambient IMS system.³⁰ The plastic IMS makes use of two Tyndall–Powell style gates constructed from two stainless steel meshes, as opposed to the Bradbury–Neilson gate of the commercial system. The ion packets produced by the Tyndall–Powell gate are not as narrow or as well shaped like those of a Bradbury–Neilson gate.^{47,48} This deviation from ideality in ion gating is likely to cause the reduction in resolving power in FT mode with the 3D-printed spectrometer. Variation in dead time is another factor that may impact resolving power.⁴⁹ Although the resolving power is

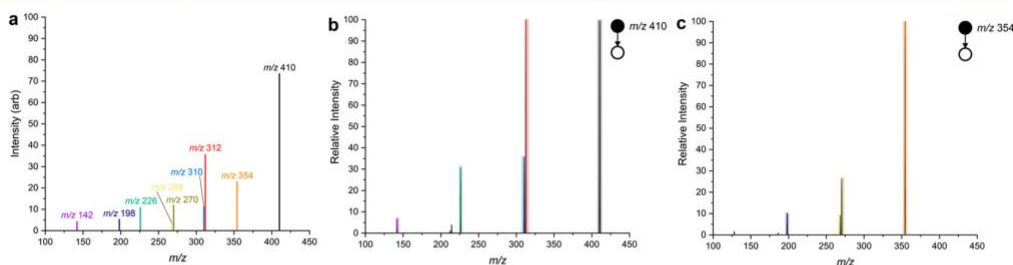


Figure 4. (a) Reconstructed mass spectrum using CID from the Fourier transform-ion mobility spectrum of each ion. (b) Isolation and fragmentation of the C_6 TAA cation in the ion trap without ion mobility. (c) Isolation and fragmentation of the C_7 TAA cation in the ion trap without ion mobility. CID mass spectrum shows product ions belonging to both precursors which can be identified using ion mobility information.

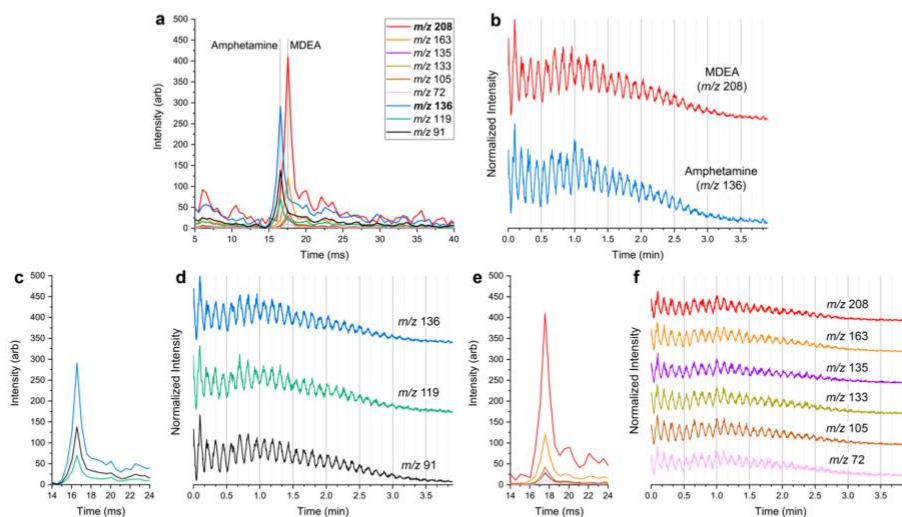


Figure 5. (a) Ion mobility spectra using in-source fragmentation of amphetamine (m/z 136) and its fragments m/z 119 and 91 and MDEA (m/z 208) and its fragments m/z 163, 135, 133, 105, and 72. (b) Ion chronograms for precursor ions amphetamine and MDEA show differences in arrival frequency corresponding to their differences in drift time. (c) Ion mobility spectra from the same data for only amphetamine and its fragment showing that all peaks have the same arrival time. (d) Ion chronograms for amphetamine and its fragment ions showing again the ions of m/z 119 and 91 maintain the frequency of the amphetamine precursor. (e) Ion mobility spectra (from the same data) for only MDEA and its fragment showing that all peaks have the same arrival time. (f) Ion chronograms for MDEA and its fragments again showing that the fragment ions maintain the frequency of the MDEA precursor.

reduced, the signal intensity is increased by over an order of magnitude when compared to the mobility selection mode of operation.²¹

FT-IMS-CID of TAA Cations. Ion mobility data can be used to determine the family of precursors and product ions to which an ion belongs. Because the product ions maintain the precursor ion's frequency pattern,³¹ they are expected to have the same arrival time distribution as the precursor. This allows for simultaneous collection of fragmentation and drift time information. Because all ions are being fragmented simultaneously, a priori knowledge of the precursor ion m/z is lost. However, for small molecules and singly charged ions, the precursor ion is likely to be the observed species with the largest m/z , though this may not be true for larger or more highly charged molecules.

For nonspecific CID fragmentation in the ion trap, a m/z 100 mass selection window was used, which is sufficient to isolate two adjacent TAA cations. Isolation of two TAA cations without fragmentation is given in Figure 3a. In order to fragment the TAA cations, the excitation mass chosen was the average mass of the two TAA precursor cations. The resulting CID spectrum contains both precursor ions and product ions originating from each precursor. Plotting the ion mobility spectrum with both precursors and their product ions shows two distinct arrival times as product ions have the arrival time of their precursor (Figure 3b). Plotting each precursor and their fragments individually, as ion chronograms, highlights the fact that the precursors and product ions have the same drift time (Figure 3c and 3d).

<https://dx.doi.org/10.1021/acs.analchem.9b05507>
Anal. Chem. 2020, 92, 5107–5115

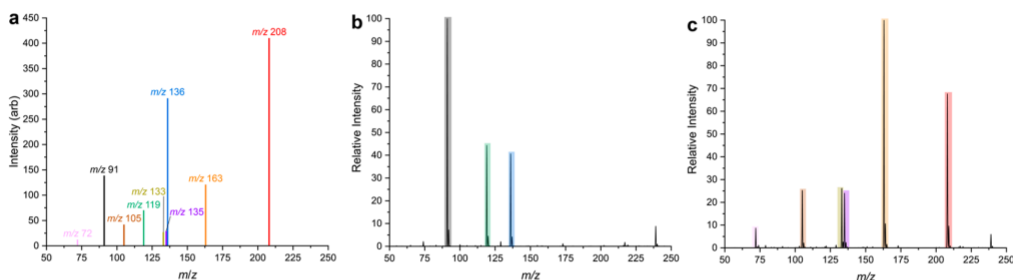


Figure 6. (a) Reconstructed in-source mass spectrum with in-source fragmentation from the Fourier transform for amphetamine, MDEA, and their detected fragments. (b) Full scan mass spectrum of amphetamine with source fragmentation without ion mobility showing amphetamine and its product ions. (c) Full scan mass spectrum of MDEA with source fragmentation without ion mobility showing MDEA and its product ions. Product ions coming from either amphetamine or MDEA can be identified with ion mobility information.

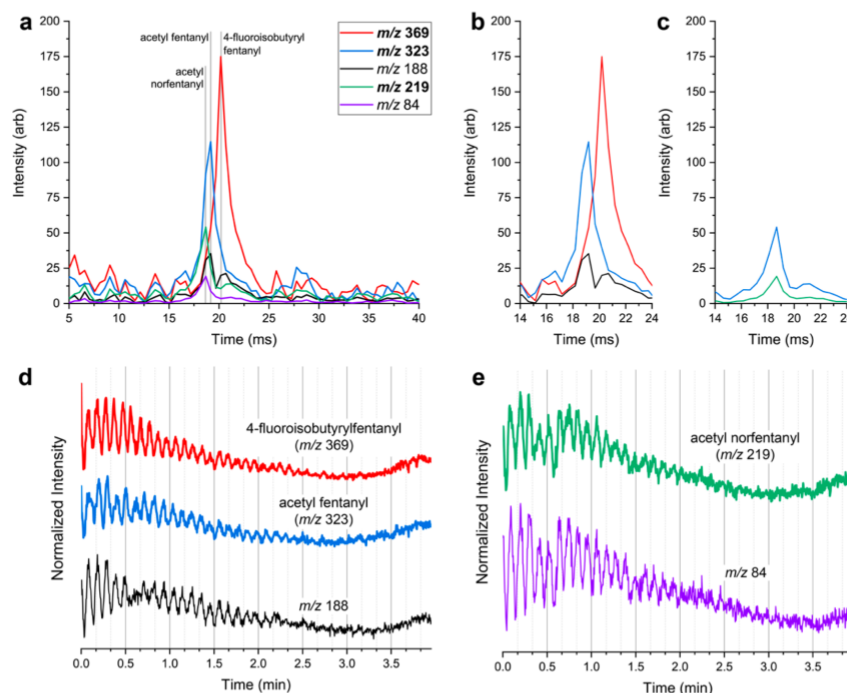


Figure 7. (a) Ion mobility spectra using in-source CID for 4-fluoroisobutyrylfentanyl (m/z 369), acetyl fentanyl (m/z 323), their fragment m/z 188, acetyl norfentanyl (m/z 219), and its fragment m/z 84. (b) Ion mobility spectra (from the same data) of only 4-fluoroisobutyrylfentanyl, acetyl fentanyl, and their fragment m/z 188. The fragment ion shows two peaks corresponding to the drift time of both of its precursors. (c) Ion mobility spectra (from the same data) of acetyl norfentanyl and its fragment m/z 84 showing that both peaks have the same arrival time. (d) Ion chromatograms for 4-fluoroisobutyrylfentanyl, acetyl fentanyl, and their fragment m/z 188 showing that the product ion frequency is a combination of both precursor ion frequencies. (e) Ion chromatograms for acetyl norfentanyl and its product ion m/z 84 showing that the product ion maintains the frequency of the acetyl norfentanyl precursor.

The CID mass spectrum (Figure 4a) of the C_6 and C_7 TAA isolation was reconstructed from the intensity values of the peaks in the FT-IMS spectrum. When compared with the product ion spectra recorded by the ion trap of the C_7 TAA cation (Figure 4b) and C_6 TAA cation (Figure 4c), it is clear that fragments from each precursor can be identified in the

reconstructed mass spectrum. Although the mass spectrum collected contains products from all precursor ions, ion mobility information allows identification of which product ions are from the C_7 TAA cation and which product ions are from the C_6 TAA cation.

It is clear that drift time information can be used to determine families of precursors and product ions as seen for the data in Figure 3b. Furthermore, in this case, the precursor can be assumed to be the ion of the highest m/z at a particular arrival time. When using the LTQ ion trap, this method is limited by the selection window and uneven fragmentation due to excitation at a single resonance frequency. One can envisage the experiment being done without ion isolation and with the use of broad-band excitation to cause fragmentation. This can be accomplished using a stored waveform inverse Fourier transform (SWIFT) for excitation.⁵⁰ This contrasts with the typical ion trap CID experiment in which a single precursor is isolated and activated using a single-resonance frequency and then subjecting the resulting product ions to mass analysis.⁵¹

Separation and Fragmentation of Drugs of Abuse. The plastic IMS combined with mass spectrometry has been used previously to detect drugs of abuse.²¹ Drug compounds were shown to be resolved, though not to baseline. Using the FT-IMS mode, similar performance was achieved for amphetamines (Figure S2) and fentanyl (Figure S3). As is the case of the TAAs, signal intensity was improved by over an order of magnitude when comparing the original²¹ with the FT-IMS mode of operation. On the basis of the data gathered for the TAA cations, a gate waveform of 5–2005 Hz was chosen for further experiments. While lowering the sweep rate should further increase the SNR and resolving power, this necessarily increases the acquisition time. Therefore, the sweep rate used here was chosen to give the best SNR and resolving power.

CID can be performed in the source region prior to mass analysis. This results in a full scan mass spectrum containing product ions generated from all precursors. This method of nontargeted fragmentation was applied for the amphetamines and fentanyls. The ion mobility spectrum for amphetamine, MDEA, and for the product ions of both precursors is given in Figure 5a. The difference in frequency of the two species can be seen in the arrival time frequency which is encoded in each ion chronogram (Figure 5b). Amphetamine has two product ions, m/z 119 and 91, which have the same arrival frequency as the amphetamine precursor (Figure 5c). When plotted alone (from the same data set), the ion mobility spectrum of amphetamine and its product ions shows that all three peaks have the same drift time (Figure 5d). Similarly, the fragments of MDEA, m/z 163, 135, 133, 105, and 72, were observed at the same drift time as the MDEA precursor (Figure 5e). This is also reflected from the ion chronograms of MDEA and its products having the same frequency (Figure 5f).

Using intensities from the ion mobility spectrum of all detected precursors and their fragments, an in-source CID mass spectrum can be reconstructed (Figure 6a) using the knowledge of precursors and product ions from the FT-IMS information. Mass spectra acquired using pure solutions of amphetamine and MDEA with in-source fragmentation are given in Figure 6b and 6c. When comparing the reconstructed spectrum with the standards, the precursor of the fragments can be easily identified. In-source fragmentation has the advantage of producing both MS^2 and MS^3 products. The ion trap fragmentations of amphetamine and MDEA are shown in Figure S4. The resonance excitation of the MDEA precursor yields mostly m/z 163 with a small amount of m/z 72. Subsequent fragmentation of m/z 163 yields m/z 135, 133, and 105. All of these ions are observed with in-source fragmentation because fragments produced in the source region may still fragment before entering the ion trap. If

excitation was to be done in the ion trap, this could also be achieved with a broad-band excitation waveform.

While the two amphetamines have different product ions, it is also possible to recognize samples having two precursors fragmenting to the same product ions. Acetyl fentanyl and 4-fluoroisobutyrylfentanyl both fragment to m/z 188. In the same experiment, acetyl norfentanyl, which fragments to a different product ion, was also examined. The ion mobility spectra of 4-fluoroisobutyryl fentanyl, acetyl fentanyl, and its product ion as well as acetyl norfentanyl and its product ion are given in Figure 7a. The ion mobility spectra (plotted from the same data) for acetyl fentanyl and 4-fluoroisobutyryl fentanyl and their common product ion (plotted alone) show that the product ion has two peaks corresponding to the arrival times of both precursors (Figure 7b). Similarly, the ion mobility spectra for acetyl norfentanyl and its fragment (plotted alone) show that the product ion has the same arrival time as the precursor (Figure 7c). The arrival frequencies for both precursors are different, and the product ion frequency is a combination of both of those frequencies (Figure 7d). The arrival frequencies for acetyl norfentanyl and its product ion, similar to the amphetamines, are the same (Figure 7e).

Performance achieved for the drugs of abuse in the FT-IMS method was comparable to that reported in the literature.²¹ However, signal intensity is greatly increased for the FT-IMS method. Therefore, using FT-IMS, simultaneous ion fragmentation and mobility information can be obtained more quickly (4 min versus approximately 20 min) than the previously described method.

Separation of Explosives. Explosives have been analyzed using both standalone IMS instruments⁴ as well as IMS-MS instruments.^{5,18} These compounds are commonly observed in negative nanoelectrospray as chloride, nitrite, or nitrate adducts. In the present experiments, only the chloride and nitrate adducts of the individual molecules were observed. A chloride adduct of the HMX dimer was observed as well. Negative ion mode experiments were performed analogously to positive mode experiments with opposite polarity of ion mobility voltages. The ion mobility spectra for each observed ion are shown in Figure S5a. Ion chronograms for each ion are shown in Figure S5b. Signal intensity for these experiments was much lower than that for the experiments with the drugs of abuse, an effect seen in both the absolute signal intensity and the signal/noise level. The noise seen in the frequency domain signal has a negative effect on the transformed arrival time distribution, i.e., the ion mobility spectrum.

Tandem mass spectrometry of chloride-adducted HMX is limited to the fragmentation of the dimers back to monomers.^{52,53} Moreover, the fragmentation of the NO_3 adduct is inefficient.⁵⁴ As a result, attempts to perform fragmentation on the explosives were unsuccessful. The source fragmentation potential was either insufficient to induce fragmentation or resulted in a total loss in signal intensity. This highlights the need for broad-band excitation capability to perform the experiment in the ion trap.

CONCLUSIONS

Fourier transform-ion mobility offers the ability to efficiently couple a 3D-printed drift tube for ion mobility to a linear ion trap. When compared to the low duty cycle mobility window selection mode of operation, resolving power was slightly reduced but signal intensity was improved by greater than an order of magnitude. This performance may be improved

further by employing a Bradbury–Neilson style gate as opposed to the Tyndall–Powell gate currently used. The Fourier transform mode of operation offered the additional advantage of the ability to perform simultaneous tandem mass spectrometry without ion isolation in the ion trap. Because product ions generated in the mass spectrometer maintain the arrival frequency of the precursors from which they were formed, correlation of related precursors and product ions was easily recognized when all ions were fragmented without isolation. The use of a 3D-printing technology to construct the ion mobility device allows easy implementation of this method into an analytical workflow. This is especially important in forensic applications where multiple analysis methods are desirable.

■ ASSOCIATED CONTENT

Supporting Information

The Supporting Information is available free of charge at <https://pubs.acs.org/doi/10.1021/acs.analchem.9b05507>.

Ion mobility spectra for C₂ TAA; ion mobility spectra for amphetamine (*m/z* 136) and MDEA (*m/z* 208) when no fragmentation energy is applied, and ion chromatograms for each amphetamine; ion mobility spectra for acetyl norfentanyl (*m/z* 219), acetyl fentanyl (*m/z* 323), and 4-fluoroisobutylfentanyl (*m/z* 369) when no fragmentation energy is applied, and ion chromatograms for each fentanyl; MS² of amphetamine, MS³ of amphetamine and *m/z* 119, MS² of MDEA, and MS³ of MDEA and *m/z* 163; ion mobility spectra of trinitroglycerin chloride adduct (*m/z* 262, 264), trinitroglycerin NO₃ adduct (*m/z* 289), HMX chloride adduct (*m/z* 331, 333), HMX NO₃ adduct (*m/z* 358), and HMX dimer chloride adduct (*m/z* 627, 629), and ion chromatograms for all ions; drift times for all analyzed compounds (PDF)

■ AUTHOR INFORMATION

Corresponding Author

R. Graham Cooks – Department of Chemistry, Purdue University, West Lafayette, Indiana 47907, United States;
orcid.org/0000-0002-9581-9603; Email: cooks@purdue.edu

Authors

Robert L. Schrader – Department of Chemistry, Purdue University, West Lafayette, Indiana 47907, United States
Brett M. Marsh – Department of Chemistry, Purdue University, West Lafayette, Indiana 47907, United States

Complete contact information is available at:

<https://pubs.acs.org/doi/10.1021/acs.analchem.9b05507>

Notes

The authors declare no competing financial interest.

■ ACKNOWLEDGMENTS

The authors acknowledge funding from FLIR Systems, Inc.

■ REFERENCES

- (1) Lawrence, A. H. *Anal. Chem.* **1986**, *58* (6), 1269–1272.
- (2) Lawrence, A. H. *Forensic Sci. Int.* **1987**, *34* (1), 73–83.
- (3) Wu, C.; Siems, W. F.; Hill, H. H. *Anal. Chem.* **2000**, *72* (2), 396–403.
- (4) Ewing, R. G.; Atkinson, D. A.; Eiceman, G. A.; Ewing, G. J. *Talanta* **2001**, *54* (3), 515–529.
- (5) Du, Z.; Sun, T.; Zhao, J.; Wang, D.; Zhang, Z.; Yu, W. *Talanta* **2018**, *184*, 65–72.
- (6) Roscioli, K. M.; Davis, E.; Siems, W. F.; Mariano, A.; Su, W.; Guharay, S. K.; Hill, H. H. *Anal. Chem.* **2011**, *83* (15), 5965–5971.
- (7) May, J. C.; Goodwin, C. R.; McLean, J. A. *Curr. Opin. Biotechnol.* **2015**, *31*, 117–121.
- (8) Bohrer, B. C.; Merenbloom, S. I.; Koeniger, S. L.; Hilderbrand, A. E.; Clemmer, D. E. *Annu. Rev. Anal. Chem.* **2008**, *1* (1), 293–327.
- (9) Cumeras, R.; Figueras, E.; Davis, C. E.; Baumbach, J. I.; Gracia, I. *Analyst* **2015**, *140* (5), 1376–1390.
- (10) Cohen, M. J.; Karasek, F. W. *J. Chromatogr. Sci.* **1970**, *8* (6), 330–337.
- (11) Kolakowski, B. M.; Mester, Z. *Analyst* **2007**, *132* (9), 842–864.
- (12) Shvartsburg, A. A.; Smith, R. D. *Anal. Chem.* **2008**, *80* (24), 9689–9699.
- (13) Ridgeway, M. E.; Lubeck, M.; Jordens, J.; Mann, M.; Park, M. A. *Int. J. Mass Spectrom.* **2018**, *425*, 22–35.
- (14) Ibrahim, Y. M.; Hamid, A. M.; Deng, L.; Garimella, S. V. B.; Webb, I. K.; Baker, E. S.; Smith, R. D. *Analyst* **2017**, *142* (7), 1010–1021.
- (15) Kanu, A. B.; Dwivedi, P.; Tam, M.; Matz, L.; Hill, H. H., Jr. *J. Mass Spectrom.* **2008**, *43* (1), 1–22.
- (16) Adamov, A.; Mauriala, T.; Teplov, V.; Laakia, J.; Pedersen, C. S.; Kotiaho, T.; Syssoev, A. A. *Int. J. Mass Spectrom.* **2010**, *298* (1), 24–29.
- (17) Hollerbach, A.; Baird, Z.; Cooks, R. G. *Anal. Chem.* **2017**, *89* (9), 5058–5065.
- (18) Kozole, J.; Stairs, J. R.; Cho, I.; Harper, J. D.; Lukow, S. R.; Lareau, R. T.; DeBono, R.; Kuja, F. *Anal. Chem.* **2011**, *83* (22), 8596–8603.
- (19) Liuni, P.; Romanov, V.; Binette, M.-J.; Zaknoun, H.; Tam, M.; Pilon, P.; Hendrikse, J.; Wilson, D. J. *Anal. Chem.* **2014**, *86* (21), 10772–10779.
- (20) March, R. E. *J. Mass Spectrom.* **1997**, *32* (4), 351–369.
- (21) Hollerbach, A.; Fedick, P. W.; Cooks, R. G. *Anal. Chem.* **2018**, *90* (22), 13265–13272.
- (22) Keelor, J. D.; Zambrycki, S.; Li, A.; Clowers, B. H.; Fernández, F. M. *Anal. Chem.* **2017**, *89* (21), 11301–11309.
- (23) Kirk, A. T.; Allers, M.; Cochems, P.; Langejuergen, J.; Zimmermann, S. *Analyst* **2013**, *138* (18), 5200–5207.
- (24) Marshall, A. G.; Hendrickson, C. L.; Jackson, G. S. *Mass Spectrom. Rev.* **1998**, *17* (1), 1–35.
- (25) Perry, R. H.; Cooks, R. G.; Noll, R. J. *Mass Spectrom. Rev.* **2008**, *27* (6), 661–699.
- (26) Eliuk, S.; Makarov, A. *Annu. Rev. Anal. Chem.* **2015**, *8* (1), 61–80.
- (27) Syka, J. E. P.; William, J.; Fies, J. Fourier transform quadrupole mass spectrometer and method. U.S. Patent US4,755,670, 1988.
- (28) Soni, M.; Frankevich, V.; Nappi, M.; Santini, R. E.; Amy, J. W.; Cooks, R. G. *Anal. Chem.* **1996**, *68* (19), 3314–3320.
- (29) Knorr, F. J.; Ajami, M.; Chatfield, D. A. *Anal. Chem.* **1986**, *58* (4), 690–694.
- (30) Morrison, K. A.; Siems, W. F.; Clowers, B. H. *Anal. Chem.* **2016**, *88* (6), 3121–3129.
- (31) Morrison, K. A.; Bendiak, B. K.; Clowers, B. H. *J. Am. Soc. Mass Spectrom.* **2017**, *28* (4), 664–677.
- (32) Poltash, M. L.; McCabe, J. W.; Shirzadeh, M.; Laganowsky, A.; Clowers, B. H.; Russell, D. H. *Anal. Chem.* **2018**, *90* (17), 10472–10478.
- (33) Poltash, M. L.; McCabe, J. W.; Shirzadeh, M.; Laganowsky, A.; Russell, D. H. *TrAC, Trends Anal. Chem.* **2020**, *124*, 115533.
- (34) Clowers, B. H.; Siems, W. F.; Hill, H. H.; Massick, S. M. *Anal. Chem.* **2006**, *78* (1), 44–51.
- (35) Szumlas, A. W.; Ray, S. J.; Hieftje, G. M. *Anal. Chem.* **2006**, *78* (13), 4474–4481.
- (36) Tummalacherla, M.; Garimella, S. V. B.; Prost, S. A.; Ibrahim, Y. M. *Analyst* **2017**, *142* (10), 1735–1745.

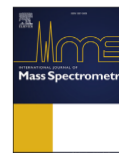
<https://dx.doi.org/10.1021/acs.analchem.9b05507>
Anal. Chem. **2020**, *92*, 5107–5115

- (37) Brock, A.; Rodriguez, N.; Zare, R. N. *Rev. Sci. Instrum.* **2000**, 71 (3), 1306–1318.
- (38) Zare, R. N.; Fernández, F. M.; Kimmel, J. R. *Angew. Chem., Int. Ed.* **2003**, 42 (1), 30–35.
- (39) Hoaglund-Hyzer, C. S.; Li, J.; Clemmer, D. E. *Anal. Chem.* **2000**, 72 (13), 2737–2740.
- (40) Valentine, S. J.; Koeniger, S. L.; Clemmer, D. E. *Anal. Chem.* **2003**, 75 (22), 6202–6208.
- (41) Stone, E.; Gillig, K. J.; Ruotolo, B.; Fuhrer, K.; Gonin, M.; Schultz, A.; Russell, D. H. *Anal. Chem.* **2001**, 73 (10), 2233–2238.
- (42) Kaplan, K.; Graf, S.; Tanner, C.; Gonin, M.; Fuhrer, K.; Knochenmuss, R.; Dwivedi, P.; Hill, H. H. *Anal. Chem.* **2010**, 82 (22), 9336–9343.
- (43) Bohnhorst, A.; Kirk, A. T.; Zimmermann, S. *Int. J. Ion Mobility Spectrom.* **2016**, 19 (2), 167–174.
- (44) Reinecke, T.; Clowers, B. H. *HardwareX* **2018**, 4, e00030.
- (45) Barmounis, K.; Maissner, A.; Schmidt-Ott, A.; Biskos, G. *Aerosol Sci. Technol.* **2016**, 50 (1), 2–5.
- (46) Knorr, F. J.; Eatherton, R. L.; Siems, W. F.; Hill, H. H. *Anal. Chem.* **1985**, 57 (2), 402–406.
- (47) Puton, J.; Knap, A.; Siodlowski, B. *Sens. Actuators, B* **2008**, 135 (1), 116–121.
- (48) Chen, C.; Chen, H.; Li, H. *Anal. Chem.* **2017**, 89 (24), 13398–13404.
- (49) Guntner, A. S.; Thalhamer, B.; Klampfl, C.; Buchberger, W. *Sci. Rep.* **2019**, 9 (1), 19182.
- (50) Julian, R. K.; Cooks, R. G. *Anal. Chem.* **1993**, 65 (14), 1827–1833.
- (51) Louri, J. N.; Cooks, R. G.; Syka, J. E. P.; Kelley, P. E.; Stafford, G. C.; Todd, J. F. *J. Anal. Chem.* **1987**, 59 (13), 1677–1685.
- (52) Cotte-Rodriguez, I.; Takáts, Z.; Talaty, N.; Chen, H.; Cooks, R. G. *Anal. Chem.* **2005**, 77 (21), 6755–6764.
- (53) Fedick, P. W.; Bills, B. J.; Manicke, N. E.; Cooks, R. G. *Anal. Chem.* **2017**, 89 (20), 10973–10979.
- (54) Garcia-Reyes, J. F.; Harper, J. D.; Salazar, G. A.; Charipar, N. A.; Ouyang, Z.; Cooks, R. G. *Anal. Chem.* **2011**, 83 (3), 1084–1092.



Contents lists available at ScienceDirect

International Journal of Mass Spectrometry

journal homepage: www.elsevier.com/locate/ijmsTemporal distribution of ions in ambient pressure drift tubes with turns[☆]Robert L. Schrader, Brett M. Marsh, R. Graham Cooks^{*}

Purdue University, Department of Chemistry, West Lafayette, IN, 47907, USA

ARTICLE INFO

Article history:
Received 3 May 2020
Received in revised form
1 July 2020
Accepted 2 July 2020
Available online 13 July 2020

Keywords:
Ion mobility
3D printing
Ion manipulation
Ion focusing
Ion optics

ABSTRACT

Ambient pressure DC-only drift tubes were constructed with one and two turns along the drift path using 3D printing and experimental data was compared to simulations. Turning was achieved using electrodes with 10°, 45° or 90° angles, arranged in various configurations. The performance of drift tubes comprised of nine (one turn) or eighteen (two turns) 10° electrodes was superior to those that achieved the same total angle but used 45° or 90° electrodes. Deviations in the spatial homogeneity of the electric field between the inside and outside of the turns in 45° and 90° electrode systems resulted in wide ion arrival time distributions. Drift tubes containing two turns in opposite directions improved ion arrival time distributions. Unlike the large reductions seen in performance using other geometries, a drift tube containing two opposite direction turns with 10° turning electrodes resulted in only a 1.4 times reduction in resolving power when compared to a straight drift tube of the same path length. Turned drift paths will allow for longer path lengths in a reduced size profile for drift tube ion mobility spectrometers operated at atmospheric pressure.

© 2020 Elsevier B.V. All rights reserved.

1. Introduction

Drift tube ion mobility spectrometry (DT-IMS) separates ions in the gas phase traveling through a constant electric field based on their size-to-charge ratio [1–3]. Drift tube ion mobility has been used to characterize small molecules such as illicit drugs [4,5], explosives [6], and chemical warfare agents [7], as well as large molecules including proteins [8]. Often very long drift tubes, on the order of meters, are used to achieve high resolution [9,10]. Long drift tubes present a challenge as this necessitates large instrumentation.

Several ion mobility instruments including ion cyclotron mobility spectrometry [11], structures for lossless ion manipulation (SLIM) [12], and cyclic IMS [13] feature curved trajectories to allow for theoretically unlimited ion path lengths. Some [12,13] make use of traveling waves for ion mobility separation. By turning the ion beam, long path lengths can be achieved without a commensurately long drift path. Each of these techniques has been implemented at reduced pressure with use of an RF electric field (or RF

element between drift tubes) for axial ion confinement. “S-bend” shaped drift tubes have been used to couple coaxial laser beams to ion mobility separators [14]. The turning of ions is also important in quadrupole devices, for example to separate the ion path from the path of neutrals prior to detection [15–17]; quadrupole deflectors can be used to turn ions from multiple sources [18]. Though the efficient control of ion beams at reduced pressures using RF is well understood, it necessitates the use of vacuum pumps, adding to power and weight burdens.

3D printed electrodes operated with high voltage DC potentials have been used to turn ion beams at atmospheric pressure [19,20]. These studies examined the spatial distribution of the ion beams, but the temporal distribution was not investigated. A marked racetrack effect is expected because ions on the inside of a turn have a shorter path to travel than ions on the outside. Ions may experience electric field inhomogeneities depending on their starting position. The effect on resolution of racetrack effects in the ion cyclotron mobility spectrometry, SLIM, and cyclic IMS were shown to be minimal [11,13,21,22]. Radial confinement of the ion

[☆] Dedicated to the memory of Bill Hase whose computational studies led, confirmed and amplified experiments in always lively fashion.

^{*} Corresponding author. 560 Oval Drive, Department of Chemistry, Purdue University, West Lafayette, IN, 47907-2084, USA.

E-mail address: cooks@purdue.edu (R.G. Cooks).

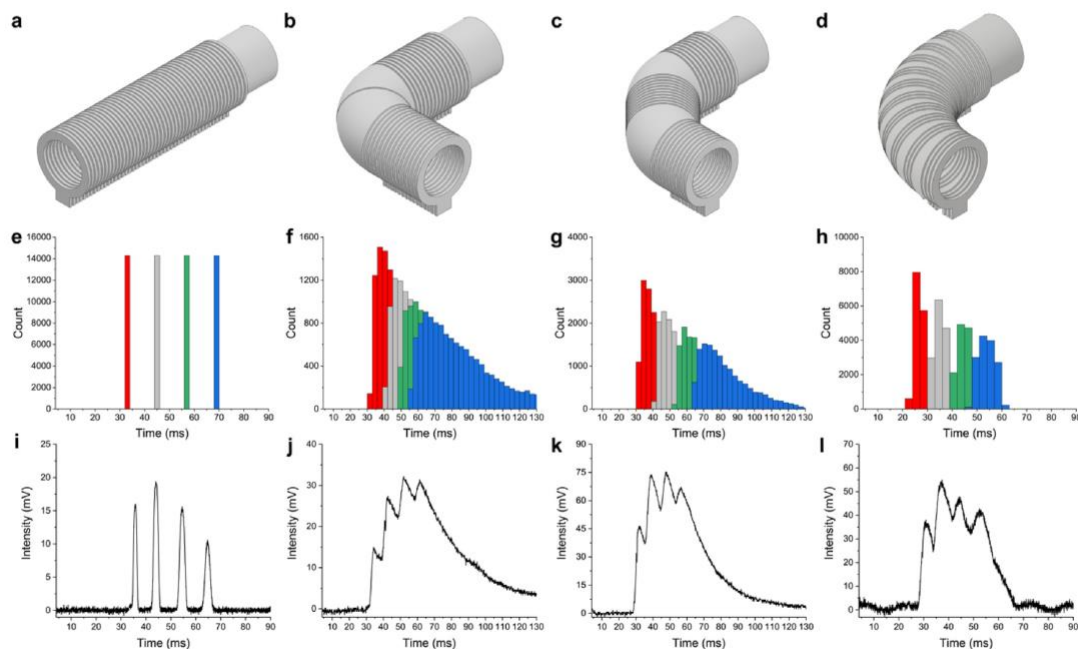


Fig. 1. Renderings of (a) straight drift tube with same path length as single turn drift tubes, turn with (b) two consecutive 45° electrodes, (c) two separated 45° electrodes, and (d) nine separated 10° electrodes. Histogram of drift times from SIMION trajectory simulations for (e) straight drift tube, turn with (f) two consecutive 45° electrodes, (g) two separated 45° electrodes, and (h) nine separated 10° electrodes. Experimental results with C_2 , C_4 , C_6 , and C_8 tetraalkylammonium salts for (i) straight drift tube, turn with (j) two consecutive 45° electrodes, (k) separated 45° electrodes, and (l) turn with nine separated 10° electrodes.

beam likely limits the differences in ion path and electric field inhomogeneity that the ions experience.

Here, drift tube ion mobility devices (Fig. S1) with one turn, two turns in the same direction, and two turns in opposite directions were fabricated using 3D printing, tested at atmospheric pressure, and their performance was compared with simulation. Ion beams are much more radially spread in atmospheric pressure drift tubes and racetrack effects are much more prominent than in ion mobility devices incorporating RF confinement at reduced pressure.

2. Materials and methods

2.1. 3D printing

All housings and electrodes were designed in Autodesk Inventor (San Rafael, CA) and converted to '.stl' files. To prepare for 3D printing, stereolithography files were sliced with Simplify3D (Cincinnati, OH) to break the model into printable layers and generate commands for the 3D printer as '.gcode' files. Housings were printed from ColorFabb (Belfeld, Netherlands) polylactic acid/

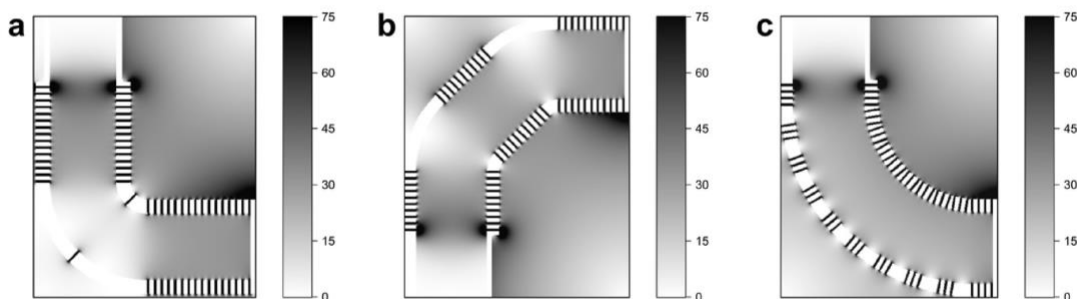


Fig. 2. Electric field strength (V/mm) calculated from SIMION of a single turn using (a) two consecutive 45° turning electrodes, (b) two separated 45° turning electrodes, and (c) nine separated 10° turning electrodes.

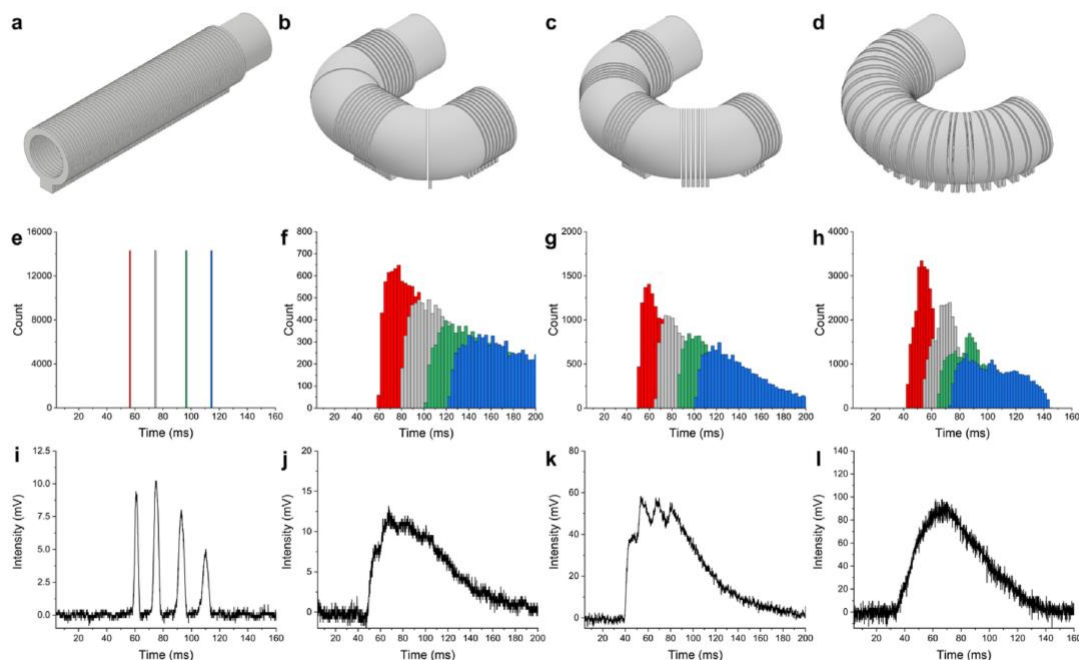


Fig. 3. Renderings of (a) straight drift tube with same path length as hairpin drift tubes, hairpin with (b) two turns with two consecutive 45° electrodes, (c) four turns with separated 45° electrodes, and (d) 18 separated 10° electrodes. Histogram of SIMION trajectory simulations for (e) straight drift tube, hairpin with (f) two turns with two consecutive 45° electrodes (g) four turns with separated 45° electrodes, and (h) 18 separated 10° electrodes. Experimental results with C₂, C₄, C₆, and C₈ tetraalkylammonium salts of (i) straight drift tube, hairpin with (j) two turns with two consecutive 45° electrodes, (k) four turns with separated 45° electrodes, and (l) 18 separated 10° electrodes.

polyhydroxyalkanoate filament. Electrodes were printed from Proto-pasta (Vancouver, WA) conductive polylactic acid filament. All housings and electrodes were printed with a Mendelmax 3 (Maker's Tool Works, Oklahoma City, OK) 3D printer. Straight drift electrodes had dimensions 38 × 28 × 1.5 mm (o.d., i.d., thickness). Turning electrodes were generated as solids of revolution of 10°, 45° and 90° using the same dimensions as the straight drift electrodes.

2.2. SIMION simulations

Ion trajectory simulations for each drift tube were performed using SIMION 8.1 (Scientific Instrument Services, Ringoes, NJ). CAD files (*.stl) of each electrode structure were imported into SIMION using the SL toolkit. To perform atmospheric pressure simulations, the statistical diffusion simulation (SDS) model was used to model collisions with background gas [23]. Reduced mobility values from the literature [24] were used explicitly in the SDS algorithm. Ions were initially distributed randomly within a circle distribution bounded by a diameter of 6 mm and located between the first and second drift electrode. Ion arrival at a grounded plate electrode after the final drift electrode modeled the Faraday cup detector.

2.3. Electronics

A custom voltage divider circuit of 1 MΩ resistors (Stackpole Electronics, Inc., Raleigh, NC, ±1%) was built on a solderable breadboard (Mouser Electronics, Mansfield, TX) and connections

were made by inserting header pins into holes in the electrodes. For the turning, hairpin, and chicane electrodes, the breadboard was cut into multiple pieces, one for each electrode section, with a high voltage wire electrically connecting the sections. The first electrode (the focusing electrode) had a 25 mm cylindrical extension to confine the electrospray plume. This has been described in detail previously [25]. In each drift tube, the focusing electrode was 3000 V, the injection electrode was 2500/2375 V, and the drift voltage was 2400 V. The total number of electrodes for each geometry is given in Fig. S1. There is a voltage drop on each drift electrode, regardless of electrode type. An entrance ion gate was created with two steel mesh screens (40 mesh, 66% transmission, E-Fab, Santa Clara, CA) on the 1st and 2nd drift electrode. A third mesh was used at the exit of the drift tube to shield the Faraday cup detector. High voltage DC potentials (±0.2%) were applied from a custom power supply. Switching was performed using a Behlke GHTS 60 A (Billerica, MA) high voltage switch with input waveforms from a precision square waveform generator operating at a frequency in the range of 2–10 Hz (Model DG535, Stanford Research Systems, Stanford, CA), the chosen value depending on ion arrival times of interest. An injection time of 1 ms was used for all experiments. Detection was performed using a custom PCB Faraday cup with an SMB (Sub-Miniature B) connection to a Keithley 428 current amplifier (Solon, OH). Data for straight drift tubes was collected with an amplification of 10⁸ V/A and data for turning drift tubes was collected with an amplification of 10⁹ V/A. Data was collected using a Tektronix TDS 2024C 4-channel digital oscilloscope (Beaverton, OR).

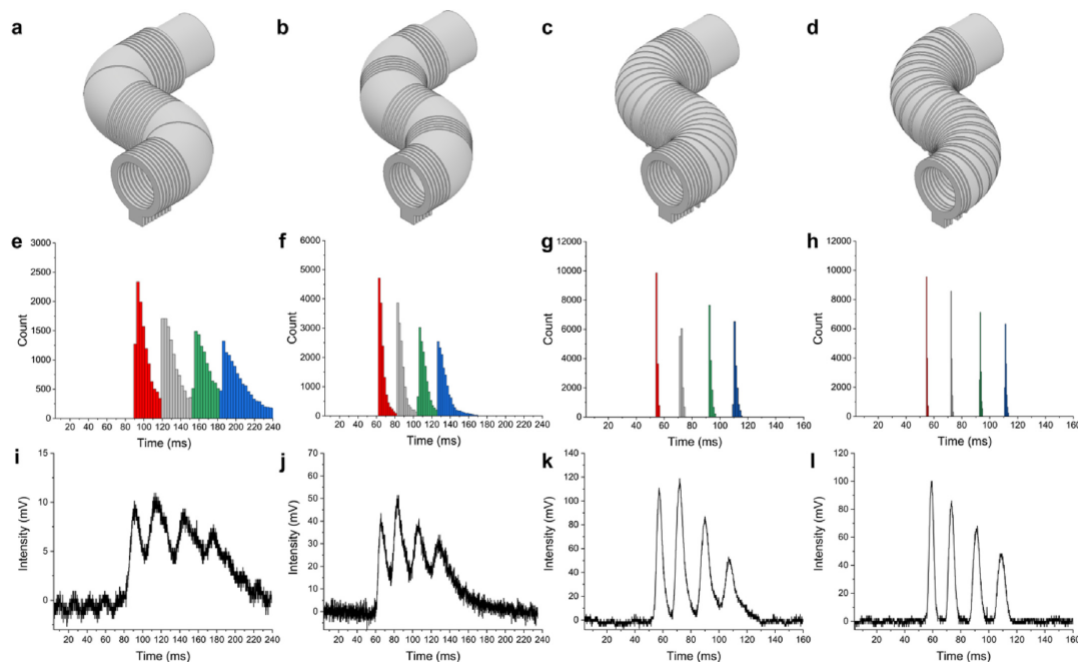


Fig. 4. Renderings of chicane drift tube with (a) two turns with two consecutive 45° electrodes, (b) four turns with separated 45° electrodes, (c) two turns with 18 consecutive 10° electrodes, and (d) 18 separated 10° electrodes. Histogram of drift times from SIMION trajectory simulations for chicane with (e) two turns with two consecutive 45° electrodes, (f) four turns with separated 45° electrodes, (g) two turns with 18 consecutive 10° electrodes, and (h) 18 separated 10° electrodes. Experimental results with C₂, C₄, C₆, and C₈ tetraalkylammonium salts for chicane with (i) two turns with two consecutive 45° electrodes, (j) four turns with separated 45° electrodes, (k) two turns with 18 consecutive 10° electrodes, and (l) 18 separated 10° electrodes.

2.4. Chemicals

Tetraethylammonium bromide, tetrabutylammonium bromide, tetrahexylammonium bromide, and tetraoctylammonium bromide were purchased from Sigma Aldrich (St. Louis, MO). Each tetraalkylammonium (TAA) salt was prepared at 100 μ M concentration in acetonitrile (Fisher Scientific, Hampton, NH).

2.5. Ionization

Borosilicate glass capillaries (i.d. 0.86 cm, o.d. 1.5 cm, 10 cm length) were purchased from Sutter Instruments (Navajo, CA). The capillaries were pulled to an approximate tip diameter of 5 μ m using a P-97 Flaming/Brown tip puller (Sutter Instruments). Pulled capillaries were fitted to a Warner Instruments (Hamden, CT) E series electrode with a 0.127 mm diameter silver wire (Alfa Aesar, Ward Hill, MA). Capillaries were placed approximately 1–2 mm from the entrance mesh. High voltage (5.5 kV) was applied to the electrode holder.

3. Results and discussion

3.1. Drift tubes with one turn

Four different 90° drift tubes were fabricated, each with a different configuration of electrodes. “Consecutive” geometries refer to turning electrodes placed successively without interruption, and “separated” geometries refer to geometries where turning

electrodes are separated by one or more straight drift electrodes. The four 90° drift tubes were: two consecutive 45° electrodes, two separated 45° electrodes, nine separated 10° electrodes, and one 90° electrode. A straight drift tube of the same path length (measured along the center line) was fabricated for comparison. Computer-generated renderings of each drift tube are given in Fig. 1(a–d). Histograms of ion drift times calculated from SIMION trajectory simulations for each drift tube are shown in Fig. 1(e–h). Experimental data for each drift tube is shown in Fig. 1(i–l). Good agreement was seen between the simulated arrival time distributions and the experimental ion mobility spectra. Reduced mobilities (K_0) were used explicitly in the SDS algorithm because estimated values can be incorrect by as much as 40% [26]. Data for the poorest performing system, the single 90° electrode are shown in Fig. S2 and ion trajectory simulations for all others in Fig. S3.

The loss in resolving power as a result of the turn can be attributed to two factors: (1) differences in path length of ions on the inside of the turn versus ion on the outside of the turn and (2) differences in electric field strength on the inside vs the outside of the turn. The magnitude of loss in resolving power is much greater in the drift tubes with 45° electrodes than for the drift tube with 10° electrodes. The electric field gradient in the plane normal to ion motion is greater in the turn for 45° electrode structures than for the 10° electrode structures (Fig. 2). This leads to a large dispersion in the ion arrival time due to variation in drift field strength based on the ion’s position. The drift field is far more homogenous for the 10° electrodes; hence the smaller resolution reduction for these for these electrodes even after considering the greater number of electrodes.

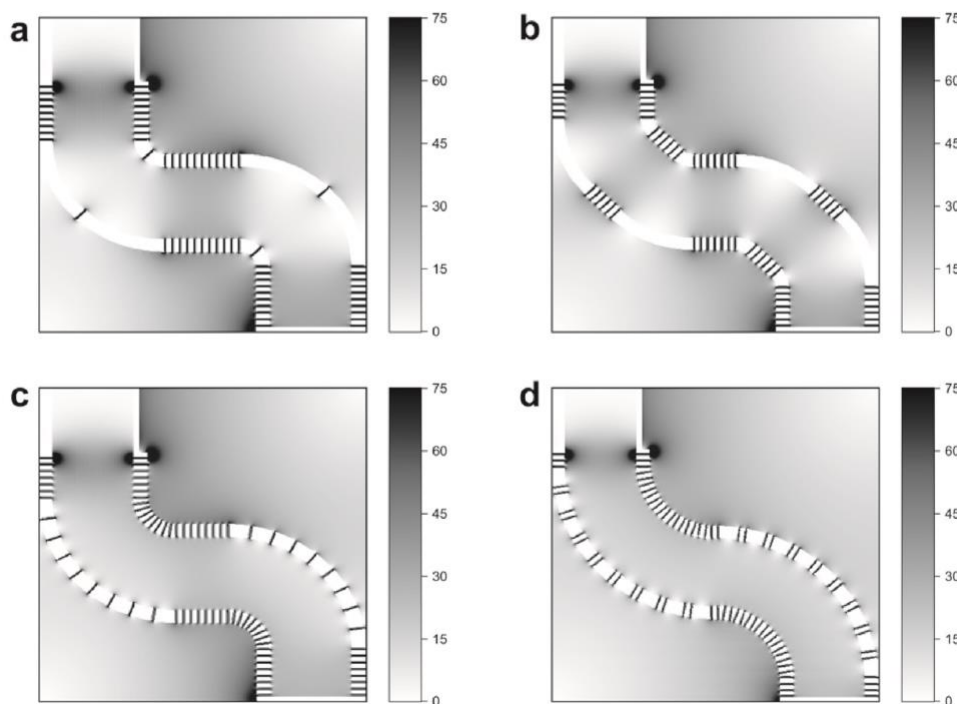


Fig. 5. Electric field strength (V/mm) calculated from SIMION of the chicane with (a) two turns with two consecutive 45° electrodes, (b) four turns with separated 45° electrodes, (c) two turns with nine consecutive 10° electrodes, and (d) 18 separated 10° electrodes.

3.2. Drift tubes with two turns

Two potential geometries exist for drift tubes with two turns: two turns in the same direction (a hairpin) and two turns in the opposite direction (a chicane). For the hairpin, three different drift tube geometries were fabricated: two turns with two consecutive 45° electrodes, four turns with separated 45° electrodes, and 18 separated 10° electrodes. A straight drift tube with the same path length (measured along the center line) as the hairpin drift tubes was fabricated for comparison. SIMION simulations showed that ions do not pass through a hairpin with two 90° turns, so this device was not fabricated. Computer-generated renderings of each drift tube are shown in Fig. 3(a–d). Histograms of ion drift times calculated from SIMION trajectory simulations for each drift tube are shown in Fig. 3(e–h) and experimental data is shown in

Fig. 3(i–l). The corresponding ion trajectory simulations are shown in Fig. S4. As with single turning drift tubes, SIMION simulations show good agreement with the experimental data. Resolution is further degraded in the two turn geometries when compared to the drift tubes with one turn as differences in path length and electric field strength are exaggerated.

For chicane drift tubes, four different drift tube geometries were fabricated: two turns with two consecutive 45° electrodes, four turns with separated 45° electrodes, 18 separated 10° electrodes, and two turns with 18 consecutive 10° electrodes. As with the hairpin, SIMION simulations showed that ions do not pass through a chicane with two 90° electrodes, so this device was not fabricated. Computer-generated renderings of each drift tube are shown in Fig. 4(a–d). Histograms of ion drift times calculated from SIMION trajectory simulations for each drift tube are shown in Fig. 4(e–h) and experimental data is shown in Fig. 4(i–l). The corresponding ion trajectory simulations are shown in Fig. S5. Hairpin and chicane drift tubes have the same path length, so both can be compared with the same length straight drift tube.

Unlike the turn and hairpin drift tubes, because there are two turns in the chicane drift tube an ion originating off-center on either side of the drift tube will travel the same path length. The resulting correction led to lower temporal dispersions for the chicane drift tubes. For both drift tubes containing 45° electrodes, resolving powers were still very low which is attributed to the differences in electric field strength caused by the 45° electrodes, Fig. 5(a and b).

Table 1

Comparison of drift time and resolving power for straight drift tube versus chicane with 18 separated electrodes. (C_m refers to the tetraalkylammonium cation with m -carbon alkanes).

	Straight		Chicane	
	Drift Time (ms)	Resolving Power	Drift Time (ms)	Resolving Power
C_2	60.7	24.3	59.1	16.5
C_4	75.2	20.9	73.4	17.1
C_6	92.9	22.1	91.2	17.3
C_8	110.4	26.2	108.5	16.0

Unlike the previously discussed geometries, the performance degradation in chicane drift tubes with 10° electrodes was greatly reduced compared the straight drift tubes. The average resolving power was reduced by 1.4 times (Table 1) for the chicane with 18 separated 10° electrodes. Additionally, after correcting for the difference in amplifier gain, the ion losses between the straight drift tube and this geometry were minimal. Performance was reduced when the turning electrodes were arranged consecutively. This is attributed to the electric field strength differences between the two geometries, Fig. 5(c and d). A general observation is that the difference in electric field strength in the turns was greater when all of the turning electrodes were placed consecutively versus placing a drift electrode between each turning electrode. The effect of off-axis ion generation points was explored using trajectory simulations for the highly favorable chicane 18 electrode geometry (Figs. S6 and S7). The data accord with expectation in showing a dramatic loss in resolution off-axis.

4. Conclusions

Manipulation of ions at ambient pressure with DC fields offers many advantages over vacuum manipulations using RF fields, although the former situation is much less well understood. The detailed geometry of turning electrodes proved to be paramount to the resulting ion arrival time distributions. The electric field strength within electrodes of 45° and 90° turns was such that temporal distributions were highly distorted due to ions experiencing different drift fields based on initial ion position. Electric field inhomogeneities were greatly reduced for drift tubes with small angle (10°) turning electrodes. Chicane drift tube designs such that ion paths are identical for ions beginning on either side of the drift tube resulted in resolving power decreasing by only 1.4x versus a comparable straight drift tube. Further optimization of the chicane geometry including difference in voltage drops between lens elements will allow for compact atmospheric drift tube designs with long path lengths.

Author statement

All three authors contributed to the concepts underlying this project. RLS performed the experiments and drafted the manuscript.

Declaration of competing interest

Each of the authors declares no conflict of interest.

Acknowledgements

The authors acknowledge funding from FLIR Systems, Inc. Greg Eakins (Jonathan Amy Facility for Chemical Instrumentation at Purdue University) is thanked for design of the PCB Faraday cup.

Appendix A. Supplementary data

Supplementary data to this article can be found online at <https://doi.org/10.1016/j.ijms.2020.116391>.

References

- [1] R. Cumeras, E. Figueras, C.E. Davis, J.I. Baumbach, I. Gràcia, Review on ion mobility spectrometry. Part 1: current instrumentation, *Analyst* 140 (5) (2015) 1376–1390.

- [2] M.J. Cohen, F.W. Karasek, Plasma chromatography™—a new dimension for gas chromatography and mass spectrometry, *J. Chromatogr. Sci.* 8 (6) (1970) 330–337.
- [3] S. Armenta, F.A. Esteve-Turrillas, M. Alcalá, Analysis of hazardous chemicals by “stand alone” drift tube ion mobility spectrometry: a review, *Anal. Meth.* 12 (9) (2020) 1163–1181.
- [4] A. Hollerbach, P.W. Fedick, R.G. Cooks, Ion mobility—mass spectrometry using a dual-gated 3D printed ion mobility spectrometer, *Anal. Chem.* 90 (22) (2018) 13265–13272.
- [5] T. Keller, A. Miki, P. Regenscheit, R. Dirnhofer, A. Schneider, H. Tsuchihashi, Detection of designer drugs in human hair by ion mobility spectrometry (IMS), *Forensic Sci. Int.* 94 (1) (1998) 55–63.
- [6] R.G. Ewing, D.A. Atkinson, G.A. Eiceman, G.J. Ewing, A critical review of ion mobility spectrometry for the detection of explosives and explosive related compounds, *Talanta* 54 (3) (2001) 515–529.
- [7] M.A. Mäkinen, O.A. Anttalainen, M.E.T. Sillanpää, Ion mobility spectrometry and its applications in detection of chemical warfare agents, *Anal. Chem.* 82 (23) (2010) 9594–9600.
- [8] S.J. Allen, K. Giles, T. Gilbert, M.F. Bush, Ion mobility mass spectrometry of peptide, protein, and protein complex ions using a radio-frequency confining drift cell, *Analyst* 141 (3) (2016) 884–891.
- [9] S.L. Koeniger, S.I. Merenbloom, S.J. Valentine, M.F. Jarrold, H.R. Udseth, R.D. Smith, D.E. Clemmer, An IMS–IMS analogue of MS–MS, *Anal. Chem.* 78 (12) (2006) 4161–4174.
- [10] P.R. Kemper, N.F. Dupuis, M.T. Bowers, A new, higher resolution, ion mobility mass spectrometer, *Int. J. Mass Spectrom.* 287 (1) (2009) 46–57.
- [11] S.I. Merenbloom, R.S. Glaskin, Z.B. Henson, D.E. Clemmer, High-resolution ion cyclotron mobility spectrometry, *Anal. Chem.* 81 (4) (2009) 1482–1487.
- [12] L. Deng, Y.M. Ibrahim, A.M. Hamid, S.V.B. Garimella, I.K. Webb, X. Zheng, S.A. Prost, J.A. Sandoval, R.V. Norheim, G.A. Anderson, A.V. Tolmachev, E.S. Baker, R.D. Smith, Ultra-high resolution ion mobility separations utilizing traveling waves in a 13 m serpentine path length structures for lossless ion manipulations module, *Anal. Chem.* 88 (18) (2016) 8957–8964.
- [13] K. Giles, J. Ujma, J. Wildgoose, S. Pringle, K. Richardson, D. Langridge, M. Green, A cyclic ion mobility-mass spectrometry system, *Anal. Chem.* 91 (13) (2019) 8564–8573.
- [14] B.D. Adamson, N.J.A. Coughlan, P.B. Markworth, R.E. Continetti, E.J. Bieske, An ion mobility mass spectrometer for investigating photoisomerization and photodissociation of molecular ions, *Rev. Sci. Instrum.* 85 (12) (2014), 123109.
- [15] J.E.P. Syka, A.E. Schoen, Characteristics of linear and non-linear r.f.-only quadrupole collision cells, *Int. J. Mass Spectrom. Ion Process.* 96 (1) (1990) 97–109.
- [16] A. Michalski, E. Damoc, J.-P. Hauschild, O. Lange, A. Wiegand, A. Makarov, N. Nagaraj, J. Cox, M. Mann, S. Horning, Mass spectrometry-based proteomics using Q exactive, a high-performance benchtop quadrupole orbitrap mass spectrometer, *Mol. Cell. Proteomics* 10 (9) (2011), M111.011015.
- [17] A. Michalski, E. Damoc, O. Lange, E. Denisov, D. Nolting, M. Müller, R. Viner, J. Schwartz, P. Remes, M. Belford, J.-J. Dunyach, J. Cox, S. Horning, M. Mann, A. Makarov, Ultra high resolution linear ion trap orbitrap mass spectrometer (orbitrap elite) facilitates top down LC MS/MS and versatile peptide fragmentation modes, *Mol. Cell. Proteomics* 11 (3) (2012), 0111.013698.
- [18] P.R. Mahaffy, K. Lai, An electrostatic quadrupole deflector for mass spectrometer applications, *J. Vac. Sci. Technol.* 8 (4) (1990) 3244–3246.
- [19] Z. Baird, P. Wei, R.G. Cooks, Ion creation, ion focusing, ion/molecule reactions, ion separation, and ion detection in the open air in a small plastic device, *Analyst* 140 (3) (2015) 696–700.
- [20] K. Iyer, B.M. Marsh, G.O. Capek, R.L. Schrader, S. Tichy, R.G. Cooks, Ion manipulation in open air using 3D-printed electrodes, *J. Am. Soc. Mass Spectrom.* 30 (12) (2019) 2584–2593.
- [21] I.K. Webb, S.V.B. Garimella, A.V. Tolmachev, T.-C. Chen, X. Zhang, R.V. Norheim, S.A. Prost, B. LaMarche, G.A. Anderson, Y.M. Ibrahim, R.D. Smith, Experimental evaluation and optimization of structures for lossless ion manipulations for ion mobility spectrometry with time-of-flight mass spectrometry, *Anal. Chem.* 86 (18) (2014) 9169–9176.
- [22] S.V.B. Garimella, Y.M. Ibrahim, I.K. Webb, A.B. Ipsen, T.-C. Chen, A.V. Tolmachev, E.S. Baker, G.A. Anderson, R.D. Smith, Ion manipulations in structures for lossless ion manipulations (SLIM): computational evaluation of a 90° turn and a switch, *Analyst* 140 (20) (2015) 6845–6852.
- [23] A.D. Appelhans, D.A. Dahl, SIMION ion optics simulations at atmospheric pressure, *Int. J. Mass Spectrom.* 244 (1) (2005) 1–14.
- [24] G. Kaur-Atwal, G. O'Connor, A.A. Aksenov, V. Bocos-Bintintan, C.L. Paul Thomas, C.S. Creaser, Chemical standards for ion mobility spectrometry: a review, *Int. J. Ion Mobil. Spectrom.* 12 (1) (2009) 1–14.
- [25] A. Hollerbach, Z. Baird, R.G. Cooks, Ion separation in air using a three-dimensional printed ion mobility spectrometer, *Anal. Chem.* 89 (9) (2017) 5058–5065.
- [26] H. Lai, T.R. McJunkin, C.J. Miller, J.R. Scott, J.R. Almirall, The predictive power of SIMION/SDS simulation software for modeling ion mobility spectrometry instruments, *Int. J. Mass Spectrom.* 276 (1) (2008) 1–8.